

Characterization of Transverse Instabilities Driven by Electron Cloud

Présentée le 7 juin 2024

Faculté des sciences de base
Laboratoire de physique des accélérateurs de particules
Programme doctoral en physique

pour l'obtention du grade de Docteur ès Sciences

par

Sofia Carolina JOHANNESSON

Acceptée sur proposition du jury

Prof. F. Courbin, président du jury
Prof. M. Seidel, Dr G. Iadarola, directeurs de thèse
Prof. G. Franchetti, rapporteur
Dr K. Shing Bruce LI, rapporteur
Prof. F. Blanc, rapporteur

I am among those who think
that science has great beauty.
— Marie Curie

Till Farfar ...

Acknowledgements

I extend my heartfelt gratitude to my CERN supervisor, Dr. Giovanni Iadarola, whose unwavering support has been the cornerstone of this thesis. It simply would not have been possible without his calm and patient guidance, constant encouragement, and enduring presence during both challenging and triumphant moments.

In addition, I wish to express my sincere appreciation to Prof. Mike Seidel and Dr. Tatiana Pieloni for their invaluable mentorship, which has been instrumental in keeping me on the right path and providing much-needed support throughout this academic journey.

I would also like to extend my thanks to the brilliant minds within the e-cloud team. Dr. Lotta Mether, Dr. Konstantinos Paraschou, Dr. Luca Sabato, and Dr. Lorenzo Giacomel, your engaging discussions have enriched my understanding of the subject matter.

My deepest gratitude goes to my section leader, Dr. Giovanni Rumolo, and the dedicated members of our section. Special thanks to Nicolas, David, Elena, Sebastien, Szymon, Elias, Leonardo, Chiara, and Roxanna.

I am deeply appreciative of the camaraderie and support from many of my CERN colleagues, including Joanna, Eleanor, Tirsi, Ingrid, Hannes, Vera, Mael, Jan, Jacqueline, Jack, and many others — especially Dr. Frank Zimmermann for his encouragement and invitations to conferences.

A special mention is deserved for my office mate, Andrii, for the countless chocolates and interesting discussions, and to Anna, for her unwavering moral support.

My gratitude also extends to the entire CERN OP team, whose enabling of my measurements played a pivotal role in this journey. I am equally thankful to everyone who engaged in enlightening discussions along the way.

Last but not least, I want to convey my heartfelt appreciation to my dearest friends, Jessica, Tay, Kajsa, Louisa, Ylva, Klara, and Sigrid. Their unwavering support and the joy they brought into my life served as a vital reminder that there is a world beyond the academic realm.

Abstract

Electron cloud continues to be one of the main limiting factors of the Large Hadron Collider (LHC), the biggest accelerator at CERN. These clouds form in the beam chamber when positively charged particles are passing through and cause unwanted effects in both hardware and the beam dynamics. This thesis focuses on the modeling of the beam dynamics of transverse instabilities driven by electron clouds.

Conventional simulation methods are too computationally heavy to be able to simulate slow instabilities. Therefore the Vlasov approach was explored, which through an analytical model reduced the simulations to an eigenvalue problem and thus reduced the computational power needed to model these instabilities. This employs a model of electron cloud forces where the dipolar kicks and the detuning along the bunch coming from the electron cloud are included. This formalism is used to express the electron cloud forces arising in both LHC dipole and quadrupole magnets. To benchmark the Vlasov approach, this was compared with macroparticle simulations using the same linear description of electron cloud forces. The results showed good agreement between the Vlasov approach and macroparticle simulations for strong electron clouds, with both approaches showing a stabilizing effect from positive chromaticity. For weaker electron clouds and in the presence of chromaticity, a discrepancy in instability growth rate is observed between the Vlasov approach and macroparticle simulations, which was thoroughly investigated. It was found that the discrepancy is only present when detuning with longitudinal amplitude from electron cloud is present. If this term is removed, the two simulation approaches agree very well. Similar results were obtained when considering dipolar and quadrupolar forces from impedances.

Dedicated measurements at the LHC in conditions with high electron cloud were carried out to study electron cloud driven instabilities. Bunch trains were injected for several values of chromaticity and characteristic electron cloud driven instabilities were observed. The instability growth rate had a strong dependence on chromaticity. Macroparticle simulations using the Vlasov formalism of forces could replicate the order or magnitude of the growth rate and its strong dependence on the chromaticity. Additionally, the amount of amplitude detuning provided by the octupole magnets required for stabilizing the beam was measured for several bunch intensities and chromaticities. The results show that beams with higher intensity need less stabilizing from octupoles. Electron cloud build-up simulations show a lower electron cloud density in the center of the beam pipe of both dipoles and quadrupoles for higher bunch intensities.

Zusammenfassung

Die Elektronenwolke bleibt weiterhin einer der Hauptfaktoren, die den Large Hadron Collider (LHC), den größten Teilchenbeschleuniger am CERN, einschränken. Diese Wolken entstehen in der Strahlkammer, wenn positiv geladene Teilchen hindurchtreten, und verursachen unerwünschte Effekte sowohl in der Hardware als auch in der Strahldynamik. Diese Dissertation konzentriert sich auf die Modellierung der Strahldynamik von transversalen Instabilitäten, die durch die Elektronenwolke verursacht werden.

Konventionelle Simulationsmethoden sind zu rechenintensiv, um langsame Instabilitäten simulieren zu können. Daher wurde der Vlasov-Ansatz erkundet, der mithilfe eines analytischen Modells die Simulationen auf ein Eigenwertproblem reduzierte und somit den benötigten Rechenaufwand zur Modellierung dieser Instabilitäten verringerte. Dieser Ansatz verwendet ein Modell der Elektronenwolkenkräfte, bei dem die dipolaren Stöße und die Abstimmung entlang des Bündels, die von der Elektronenwolke stammen, berücksichtigt werden. Die Kräfte, die von der Elektronenwolke in LHC-Quadrupolen und LHC-Dipolen erzeugt werden, wurden in diesem Kraftformalismus ausgedrückt. Um den Vlasov-Ansatz zu überprüfen, wurde dieser mit Makropartikel-Simulationen unter Verwendung der gleichen linearen Beschreibung der Elektronenwolkenkräfte verglichen. Die Ergebnisse zeigten eine gute Übereinstimmung zwischen dem Vlasov-Ansatz und den Makropartikel-Simulationen für starke Elektronenwolken, wobei beide Ansätze einen stabilisierenden Effekt durch positive Chromatizität zeigten. Für schwächere Elektronenwolken und in Anwesenheit von Chromatizität wurde eine Diskrepanz in der Wachstumsrate der Instabilität zwischen dem Vlasov-Ansatz und Makropartikel-Simulationen festgestellt, die gründlich untersucht wurde. Es wurde festgestellt, dass die Diskrepanz nur vorhanden ist, wenn die Abstimmung mit der longitudinalen Amplitude der e-Cloud vorhanden ist. Wenn dieser Term entfernt wird, stimmen die beiden Simulationsansätze sehr gut überein. Ähnliche Ergebnisse wurden bei Betrachtung dipolarer und quadrupolarer Kräfte aus Impedanzen erzielt.

Dedizierte Messungen am Large Hadron Collider unter Bedingungen mit hoher Elektronenwolke wurden durchgeführt, um e-cloud-getriebene Instabilitäten zu untersuchen. Bündelzüge wurden für mehrere Werte der Chromatizität eingebracht, und charakteristische e-cloud-getriebene Instabilitäten wurden beobachtet. Die Wachstumsrate der Instabilität zeigte eine starke Abhängigkeit von der Chromatizität. Makropartikel-Simulationen unter Verwendung des Vlasov-Formalismus für Kräfte konnten die Größenordnung der Wachstumsrate und ihre starke Abhängigkeit von der Chromatizität replizieren. Zusätzlich wurde die Stabilitätsschwelle, die durch die Amplitudenabstimmung der Oktupolmagneten im LHC bestimmt

Zusammenfassung

wurde, für mehrere Bündelintensitäten und Chromatizitäten gemessen. Die Ergebnisse zeigen, dass Strahlen mit höherer Intensität weniger Stabilisierung durch Oktupole benötigen. Simulationen zum Aufbau der Elektronenwolke zeigen eine geringere Elektronendichte in der Mitte des Strahlrohrs von sowohl Dipolen als auch Quadrupolen, was von der beobachteten Intensitätsabhängigkeit herrührt.

Résumé

Le nuage d'électrons reste l'un des principaux facteurs limitants du Grand collisionneur de hadrons, le plus grand accélérateur du CERN. Ces nuages se forment dans la chambre à vide du faisceau lorsque des particules chargées positivement la traversent et provoquent des effets indésirables à la fois sur les équipements et sur la dynamique du faisceau. Cette thèse se concentre sur la modélisation des instabilités transversales provoquées par les nuages d'électrons.

Les méthodes de simulation conventionnelles demandent trop de puissance de calcul pour pouvoir simuler des instabilités lentes. C'est pourquoi une approche utilisant l'équation de Vlasov a été explorée, qui, par le biais d'un modèle analytique, réduit les simulations à une équation aux valeurs propres, diminuant ainsi la puissance de calcul nécessaire pour modéliser ces instabilités. Cette approche utilise un modèle de forces du nuage d'électrons incluant les effets des déflexions dipolaires et du désaccord en nombre d'onde le long du paquet causés par le nuage d'électrons. Ce formalisme est utilisé pour exprimer les forces du nuage d'électrons qui apparaissent dans les aimants dipolaires et quadripolaires du LHC. L'approche de Vlasov a été comparée à des simulations macroparticules utilisant la même description linéaire des forces du nuage d'électrons. Les résultats ont montré un bon accord entre l'approche Vlasov et les simulations macroparticules pour les nuages d'électrons très dense, les deux méthodes soulignant l'effet stabilisateur d'une chromaticité positive. Pour les nuages d'électrons moins denses, et en présence de chromaticité, une divergence dans le taux de croissance de l'instabilité est observée entre l'approche de Vlasov et les simulations macroparticules, ce qui a fait l'objet d'un examen approfondi. Il a été constaté que l'écart n'est présent qu'en cas de présence d'un désaccord du nombre d'onde selon l'amplitude longitudinale des particules causé par le nuage d'électrons. Si ce terme est supprimé, les deux approches sont en très bon accord. Des résultats similaires ont été obtenus en considérant les forces dipolaires et quadripolaires créées par des impédances de couplage du faisceau.

Des mesures spécifiques sur le Grand collisionneur de hadrons (LHC), dans des conditions où le nuage d'électrons était dense, ont été effectuées pour étudier les instabilités induites par le nuage d'électrons. Des trains de paquets ont été injectés pour plusieurs valeurs de chromaticité et des instabilités caractéristiques induites par le nuage d'électrons ont été observées. Le taux de croissance de l'instabilité dépendait fortement de la chromaticité. Des simulations macroparticules utilisant le formalisme des forces de Vlasov ont pu reproduire l'ordre de grandeur du taux de croissance et sa forte dépendance à la chromaticité. En outre, le degré de désaccord en nombre d'onde généré par les aimants octupolaires et nécessaire

Résumé

pour stabiliser le faisceau a été mesuré pour plusieurs intensités de paquet et plusieurs chromaticités. Les résultats montrent que les faisceaux d'intensité plus élevée necessitent moins d'octupoles pour être stabilisés. Les simulations de nuages d'électrons montrent que pour des intensités du faisceau plus grandes, la densité de nuage d'électrons est plus faible au centre de la chambre à vide des dipôles et des quadripôles.

Contents

Acknowledgements	i
Abstract (English/Français/Deutsch)	iii
Introduction	1
1 Electron cloud instabilities in Large Hadron Collider	5
1.1 The CERN accelerator complex	5
1.2 Introduction to e-cloud	7
1.3 Vlasov method applied to e-cloud instabilities	10
1.3.1 Transverse Equations of Motion	10
1.3.2 Longitudinal Equations of motion	12
1.3.3 Hamiltonian of the accelerator	15
1.3.4 Unperturbed Vlasov Equation	17
1.3.5 First order perturbation	19
1.3.6 Adapting the Vlasov equation to e-cloud	23
1.3.7 Description of the Detuning Sources	26
1.3.8 The Coherent Force	28
1.3.9 Solving the Vlasov Equation	31
1.4 E-cloud modeling for the LHC	34
1.4.1 E-cloud strength	38
1.5 Applying the introduced force modeling in macro-particle simulations	40
2 Vlasov approach for modeling e-cloud instabilities	45
2.1 Beam stability in the absence of chromaticity	45
2.2 Effect of chromaticity	51
2.3 Study the detuning term	58
2.3.1 Splitting the detuning function in two	58
2.3.2 Simulations with individual detuning terms	61
2.4 Checks with impedance in the e-cloud Vlasov formalism	68
2.4.1 Impedance in the e-cloud formalism	68
2.4.2 Comparison with conventional impedance modeling	70
2.4.3 Results with impedance forces in the e-cloud Vlasov formalism	72

Contents

3	Experimental characterization of e-cloud driven instabilities in the LHC	79
3.1	Measurements at high e-cloud conditions	79
3.1.1	Methodology	79
3.1.2	Overview of measured instabilities	80
3.1.3	Instability Growth Rate	83
3.1.4	Spectral analysis of measured data	89
3.1.5	Comparison with Simulations	94
3.2	Measurements of octupole thresholds after conditioning	105
3.2.1	Methodology	105
3.2.2	Measured Thresholds	105
3.2.3	Observed instabilities	115
3.2.4	High bunch intensity	117
3.2.5	Simulations	120
4	Conclusions	123
A	Numerical Checks	125
A.1	Number of longitudinal slices	125
A.2	Detuning from e-cloud in dipoles	127
A.3	Number of macroparticles in instability simulations	129
A.4	Number of terms Vlasov sum	130
	Bibliography	137
	Abbreviations	139
	Curriculum Vitae	141

Introduction

CERN is the largest particle physics laboratory globally, housing several large particle accelerators. The centerpiece of these accelerators is the Large Hadron Collider (LHC), a 27-kilometer synchrotron capable of accelerating two counter-rotating beams of protons up to 6.8 TeV each. The LHC, among the most complex machines ever built, demands a strong effort to achieve the precise beam parameters essential for fundamental particle physics research.

Groups of protons, known as bunches, are accelerated to 450 GeV before they reach the LHC by going through several smaller accelerators known as the injector complex. In the LHC itself, the bunches are accelerated to the final energy. A typical bunch has about 10^{11} protons.

One of the main limiting factors of the LHC performance is the electron cloud, also known as e-cloud. When protons are accelerated in the LHC electrons are emitted from the walls of the beam chamber due to radiation from the bending of the proton beam or beam losses. These electrons are referred to as seed electrons or primary electrons. Secondary electrons are emitted when the primary electrons hit the beam chamber walls with energies of a few 100 eV. The secondary electrons are then accelerated by the beam to reach high enough energies to cause additional secondary emission. This leads to a build-up of electrons in the beam chamber. The build-up process depends on the beam parameters, the geometry, and the surface properties of the beam chamber as well as the magnetic field present. In particular, the e-cloud arranges itself differently in a quadrupole magnet compared to a dipole magnet.

The detrimental effects of e-cloud manifest in various ways, including increased heat load on the beam chambers, vacuum degradation, and beam quality deterioration. The latter includes transverse beam instabilities which are exponentially growing oscillations that occur perpendicular to the beam's direction. Two key characteristics of these instabilities are the change in transverse oscillation frequency, known as tune shift, and the rate at which the transverse amplitude grows, referred to as the growth rate.

Efforts have been made to mitigate the impact of the e-cloud, primarily through surface treatments and electron irradiation of the beam chamber walls. Nevertheless, these strategies have their limitations, and the complete suppression of e-cloud formation is not possible. Altering beam parameters, particularly by reducing the number of bunches in the machine, offers a means to reduce e-cloud, yet such actions come at the cost of decreased luminosity

Introduction

production. Therefore, it is imperative to gain a comprehensive understanding of how e-cloud affects both the accelerator and beam dynamics in order to maximize the performance of the collider.

Modeling instabilities driven by e-cloud presents a substantial computational challenge when utilizing conventional methods. These simulations rely on Particle-in-Cell (PIC) algorithms, which are computationally very demanding, especially when dealing with slow instabilities characterized by low growth rates. These slow instabilities necessitate tracking a significant number of machine turns to accurately capture their dynamics. Since the computation time is directly proportional to the number of turns in the machine, the computational burden quickly becomes prohibitively heavy.

The interaction between a particle beam and the surrounding accelerator structures, referred to as beam-induced impedance, has been successfully modeled using the Vlasov approach. This approach employs the Vlasov equation to describe the collective motion of a particle distribution in a system governed by a Hamiltonian. In this approach the instability growth rate and tune shift can be calculated from the eigenvalues of the Vlasov equation, meaning the computation time is independent of the instability growth rate, which makes it very attractive to model slow instabilities.

Attempts have previously been made to model also e-cloud driven instabilities in this formalism. The e-cloud forces are introduced into the Vlasov equation as perturbations and the Vlasov equation is linearized and truncated to first order. The e-cloud forces are introduced as dipolar kicks, equivalent to generalized impedance, and as a detuning along the bunch, also known as quadrupolar forces. The resulting bunch distortion resulting from interaction with e-cloud is the unknown in the equation. Following a well-constructed ansatz of this distortion, the linearized Vlasov equation becomes an eigenvalue problem, where again the instability growth rate and tune shift can be calculated from the eigenvalues.

In the pursuit of comprehensive understanding, our research includes benchmarking the Vlasov approach against macroparticle simulations that employ the same force formalism. These simulations utilize PyHEADTAIL as a tracker and monitor the trajectory of approximately 10^5 macroparticles turn by turn in the LHC. The force formalism used in the Vlasov simulations is simplified compared to the nonlinear model in conventional PIC simulations. This simplification enables a direct benchmark of the Vlasov approach, as both simulation methods share the same force formalism.

One of the main mitigation strategies for e-cloud driven instabilities, apart from reducing e-cloud in the machine, is positive chromaticity, which is the tune-shift dependence on the momentum of each particle. For this reason, particular attention in our simulation study work was given to the modeling of chromaticity and its impact on the beam stability.

The Vlasov approach emerges as a promising avenue to study these phenomena. Not only does it offer a potential solution to simulate slow instabilities effectively, but it also provides

an opportunity to gain a deeper insight into the fundamental mechanisms underlying these instabilities, potentially enabling more effective mitigation strategies and further optimizing accelerator design.

Complementary to these analytical and simulation work, experimental studies dedicated to exploring and characterizing e-cloud-driven instabilities were conducted at the LHC as part of this research. Measurements were conducted under conditions of high e-cloud to elucidate the characteristics of e-cloud-driven instabilities in the LHC. This investigation involved meticulous observation of the position turn-by-turn for each bunch, allowing for a comprehensive analysis of bunch-by-bunch behavior, instability growth rates, and the tunes of every individual bunch in each measurement.

Furthermore, a second set of measurements was conducted in conditions with nominal e-cloud to study the effects of amplitude detuning stemming from octupoles, which are commonly employed to mitigate instabilities. This analysis involved measuring the onset of instability as the octupole strength was systematically reduced. The identified instabilities were categorized based on the measurement of the transverse position and emittances of each bunch, providing valuable insights into the LHC's operational e-cloud conditions.

This thesis is organized into three distinct sections. The first section introduces the physics of e-cloud driven instabilities and the analytical Vlasov method, providing a comprehensive overview of its underlying principles and describing how e-cloud forces can be modeled within a Vlasov formalism. The second section examines the validity of the Vlasov model for realistic LHC scenarios, providing a thorough analysis of the effects of the detuning forces from the e-cloud in combination with chromaticity. This critical assessment refines our theoretical framework and sheds light on the practical limitations and scope of the Vlasov method. In the third and final section, we present experimental studies focused on e-cloud phenomena observed at the LHC.

1 Electron cloud instabilities in Large Hadron Collider

1.1 The CERN accelerator complex

CERN, which stands for European Laboratory for Particle Physics, is a laboratory located on the border between France and Switzerland that was founded in 1954. Today, CERN is the largest laboratory for particle physics research seeking to answer the fundamental questions about our universe [1]. CERN has 23 member states, Sweden and Switzerland included, but has users from 12 000 institutions from 83 different countries as of 2022 [2]. The most notable recent scientific achievement of CERN is the discovery of the Higgs Boson, the last particle in the standard model, however many questions are still unanswered [3]. For example, what is dark matter?

The discoveries of CERN were made possible by the accelerator complex depicted in Fig. 1.1. The flagship accelerator is the LHC which is a 27-km long synchrotron that can accelerate two counter-rotating proton beams from 450 GeV to 6.8 TeV, which yields a collision energy of 13.6 TeV. The protons have a long journey before reaching the LHC at 450 GeV. The protons are initially obtained from a hydrogen source and are then accelerated as negative hydrogen ions to 160 MeV in the linear accelerator called LINAC 4. Then the ions are stripped to protons and injected into the Proton Synchrotron Booster (PSB), Proton Synchrotron (PS), and finally the Super Proton Synchrotron (SPS) where they reach an energy of 450 GeV. During this journey, the protons are grouped into bunches containing $\sim 10^{11}$ protons each with a length of a few centimeters and a transverse cross-section of a few $(\mu\text{m})^2$. A schematic figure of the bunch can be seen in Fig. 1.2. The bunch slots are separated by 25 ns. [5]

The proton bunches are then finally injected into the LHC which can store about 3000 bunches in each of the counter-rotating beams. The protons collide at interaction points within the LHC, and data from these collisions are recorded by large detectors for analysis. This process allows for the study of fundamental particles and forces in the universe. [6]

The LHC has four interaction points at which the two counter-rotating beams collide and each of them houses an experiment, ATLAS, CMS, LHCb, and ALICE. ATLAS (A Toroidal LHC

Chapter 1. Electron cloud instabilities in Large Hadron Collider

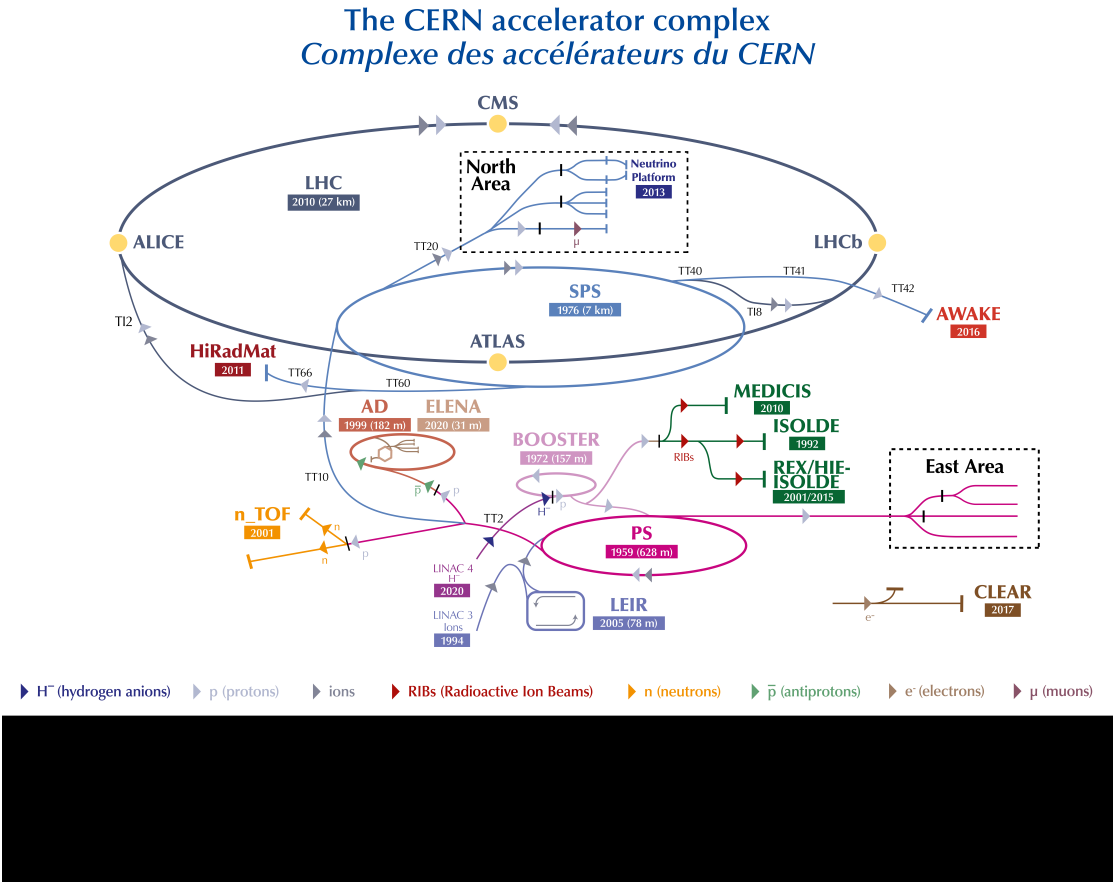


Figure 1.1: The Cern accelerator complex as of 2022, the image is taken from [4]

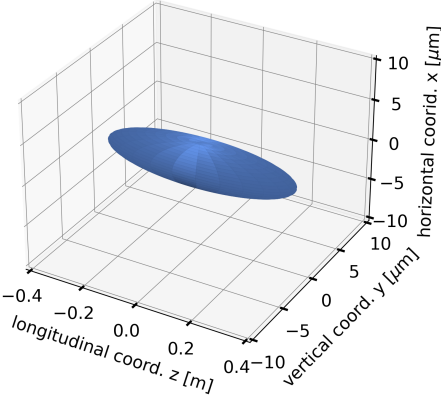


Figure 1.2: A schematic image of a particle bunch in the LHC. The longitudinal lengths are a few centimeters and the transverse lengths are a few μm .

apparatus) is the biggest of the four detectors and was built to detect the Higgs boson and search for new particles. CMS (Compact Muon Solenoid), studies the same phenomena as ATLAS but uses different types of detectors. LHCb, where "b" stands for the beauty quark, was built to investigate nature's preference for matter over antimatter. The last experiment is ALICE (A Large Ion Collider Experiment) is used when ions are accelerated in the LHC instead of protons and studies the strong interaction of particles. [7]

The first run of the LHC was between 2008 and 2013 and operated with a top energy of 4 TeV per beam. After this run, the first long shutdown took place where upgrades were made to reach beam energies of 6.5 TeV during the second run, Run 2, starting in 2015 [8]. Additionally, the bunch spacing was decreased from 50 ns to 25 ns which as anticipated caused e-cloud to be a main limiting factor of the machine [9, 10]. The machine was shut down again in 2018 for two years for further upgrades mainly on the injector chain to reach higher beam intensity and brightness. Notably, the linear accelerator at the beginning of the injector chain was replaced [11]. The LHC was successfully restarted again in 2022 for Run 3 and is expected to run until 2025. Research activities are planned in the LHC until the 2040s [12], including a major upgrade, High-Lumi LHC (HL-LHC), that will allow increasing by a large factor the produced collision rate [13].

This thesis will focus on the beam dynamics of the LHC. Beam dynamics in accelerator physics refers to the study and control of the movement, focusing, and manipulation of charged particle beams as they travel through complex accelerator systems, aiming to optimize their stability and interactions.

In the context of beam dynamics, transverse instabilities refer to undesirable motion or oscillations of charged particle beams in the transverse directions, perpendicular to the beam's forward motion. They can lead to a degradation of beam quality and beam losses. In high-intensity particle accelerators, particles exhibit collective effects due to their interactions with each other and their surroundings. Examples of these effects include the space charge effect, which results from the mutual repulsion between charged particles in a beam, and wakefields. Wakefields are electromagnetic fields generated as charged particle beams or bunches pass through a medium, typically within the beam pipe. E-cloud effects are another class of collective effects and will be further discussed in the next section. [14]

1.2 Introduction to e-cloud

E-cloud and its effect on beam dynamics have been observed in particle accelerators operating with positively charged particles since the 1970s [15]. At CERN, e-cloud effects can be seen in the PS, the SPS, and the LHC and are considered a main limitation [16] to the machine performance. The unwanted effects from e-cloud are vacuum degradation, beam energy loss, heat load on the beam screens, affects the beam diagnostics as well as an impact on the beam dynamics [17].

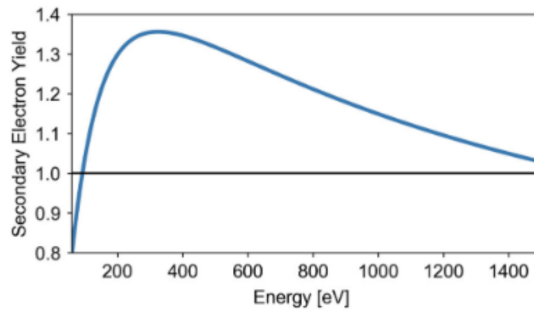


Figure 1.3: The SEY for an LHC beam screen as a function of the incident electron energy. Figure taken from [22].

Electrons are produced by ionization of residual gas and photo-emission due to synchrotron radiation or beam losses. Synchrotron radiation is the radiation emitted as a result of bending/accelerating the charged particles in an accelerator [18]. These electrons are referred to as primary electrons or seed electrons. In lepton accelerators and very high energy proton accelerators, the primary electron production is dominated by synchrotron radiation, whereas gas ionization and beam losses produce the most primary electrons in low and intermediate energy proton machines [19].

Often, the production of primary electrons alone is insufficient to lead to a significant e-cloud build-up. However, electrons impact the wall of the beam chamber with energies of a few 100 eV after being accelerated by the interaction with the beam, and when electrons hit the wall at these energies secondary emission of electrons occurs. Surfaces bombarded with electrons emit secondary electrons with a yield depending on the incident electrons energy, this curve is known as the Secondary Electron Yield or SEY for short [20]. To simplify discussions, it is common to refer to the highest point on this curve as the 'SEY value' or simply SEY. If the SEY is bigger than 1 we can have exponential multipacting of electrons in the beam chamber. A typical SEY curve of an LHC beam screen can be seen in Fig. 1.3. A schematic figure of the e-cloud build-up process can be seen in Fig. 1.4. The emission of primary electrons is proportional to the beam intensity whereas the secondary electron production depends non-linearly on the beam intensity. The secondary electron production mostly depends on the SEY. The net electron motion in the longitudinal direction is not large meaning the essential dynamics of the e-cloud are in the transverse plane. [21]

The SEY curve for LHC beam pipes has been measured and has a peak with a height in the range from 1.0 to 2.0 for incident electrons of 332 eV [23]. A way of reducing the SEY of the LHC is to coat the beam chamber with a thin film of amorphous carbon [24]. These coatings need to be very thin to not impact the impedance of the accelerator and the development of coatings thin enough is ongoing [25].

The SEY of the beam screens an accelerator can be reduced by electron irradiation [27]. The commissioning of the LHC therefore includes a scrubbing run, which aims at conditioning

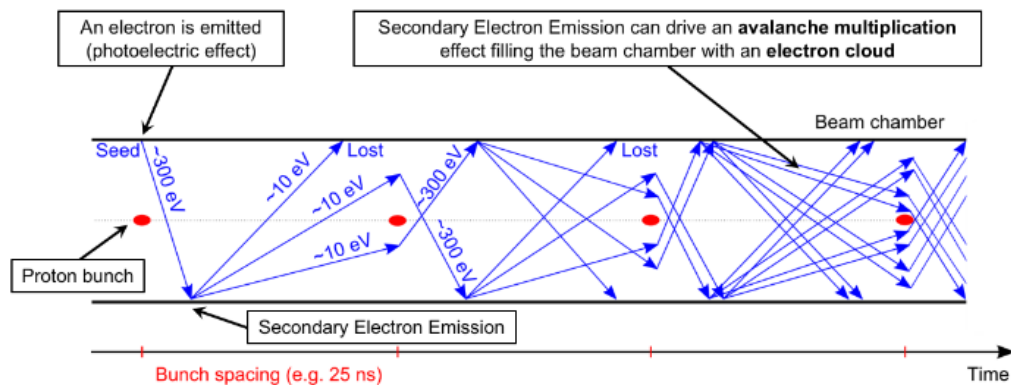


Figure 1.4: The figure is a schematic of how primary electrons are accelerated by the particle beam causing secondary emission of electrons which can drive an avalanche multipacting of electrons in the beam chamber of an accelerator. Figure taken from [26].

the beam screen using the e-cloud generated by the beam itself. The scrubbing run in 2015, beginning of run 2, reduced the SEY from approximately 2.3 to 1.4 [10]. However, due to air exposure of the LHC beam chambers during LS2, the SEY of the beam screens increased again to pre-conditioning values [10].

E-cloud builds up along the train with increasing e-cloud density for bunches towards the tail of trains. The electron population does not increase forever but saturates at a certain value due to the self-repellent field of the e-cloud. [28].

Different filling schemes, i.e. the pattern with which the bunches are arranged in the accelerator, affect the process of secondary emission of electrons and therefore the e-cloud build-up [29]. The more bunches placed consecutively after one another results in a higher average density of e-cloud in the beam chamber. For example in the LHC, the decrease from a bunch spacing of 50 ns and 25 ns leads to the heat loads on the beam screens being dominated by e-cloud effects instead of impedance and synchrotron radiation [30]. The induced heat load of the e-cloud prevents the operation of bunches closer than 25 ns [31]. The main e-cloud mitigation strategy of Run 3 is to use an alternative filling scheme where four bunch slots were left empty every eight bunches in the first bunch train [32].

The electrons arrange themselves in the beam chamber following the magnetic field lines that are present [26], see Fig 1.5. In a dipole magnet, the electrons arrange themselves in two vertical stripes, and in quadrupoles, they arrange themselves in a cross-like pattern.

E-cloud can trigger transverse beam instabilities of two types, coupled bunch instabilities, and single-bunch-instabilities [33]. The single bunch instabilities cannot be mitigated by transverse feedback systems due to the strong intra-bunch motion [34]. Intra-bunch feedback systems have also been investigated to mitigate fast intra-bunch motion in circular accelerators, although at the moment they are not foreseen to be deployed as part of the HL-LHC

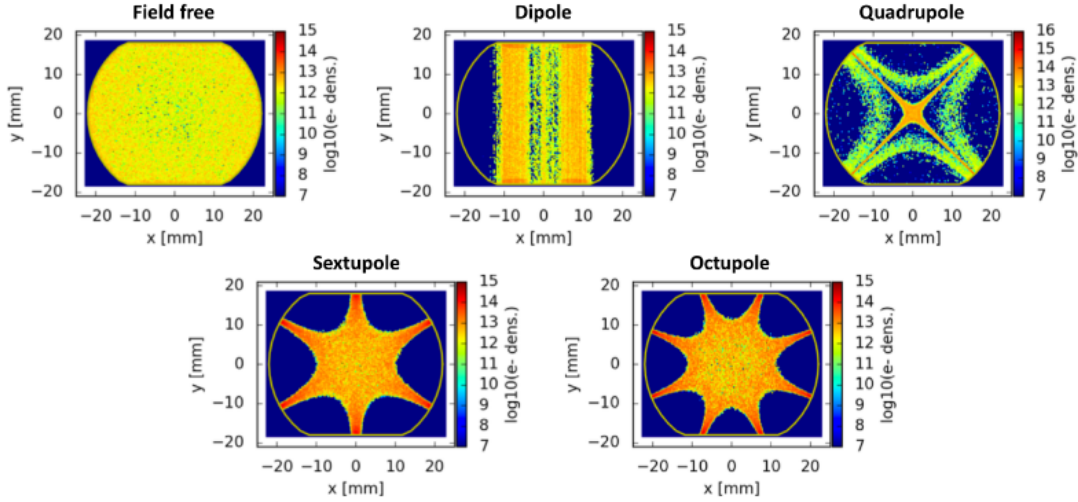


Figure 1.5: The figure shows the e-cloud distribution in a field-free region, dipole, quadrupole sextupole, and an octupole simulated with the coed PyECLLOUD. Figure taken from [26].

project [35].

The e-cloud in the quadrupole magnets is the main source of the e-cloud driven instabilities in the LHC at injection energy[36]. Chromaticity has a stabilizing effect in the single bunch instability driven by e-cloud [37].

1.3 Vlasov method applied to e-cloud instabilities

In this section e-cloud instabilities will be discussed in the using the Vlasov formalism. First, the Hamiltonian that describes the particles' motion in the accelerator will be expressed. Then the Vlasov equation will be derived from Hamiltonian mechanics. Perturbation theory will be used to introduce collective effects into the Vlasov equation. Lastly, the linearized Vlasov equation truncated to first order with forces from e-cloud will be derived.

1.3.1 Transverse Equations of Motion

The transverse equations of motion in an accelerator with a periodic lattice, such as a circular machine, can be described using the Hill's equation:

$$u''(s) + K(s)u(s) = 0, \tag{1.1}$$

where $u(s)$ is the transverse position along the path of the accelerator s . A general solution to the Hill's equation is given by:

1.3 Vlasov method applied to e-cloud instabilities

$$u(s) = \sqrt{2J} \sqrt{\beta(s)} \cos(\phi(s)\psi_0), \quad (1.2)$$

where $\beta(s)$ is an amplitude modulation along the accelerator path known as the betatron function and ψ_0 is an integration constant. J is the action and is also an integration constant. With the ansatz in Eq. 1.2 the Hills equation (Eq. 1.1) gives two constraints for the betatron function $\beta(s)$ and the phase function $\psi(s)$:

$$\frac{1}{2}(\beta\beta'' - \frac{1}{2}\beta'^2) - \beta^2\psi' + \beta^2 K(s) = 0 \quad (1.3)$$

and

$$\beta'\psi' + \beta\psi'' = (\beta\psi')' = 0 \Rightarrow \beta\psi' = \text{const.} \quad (1.4)$$

Choosing a normalization of $\beta\psi' = 1$ results in the following expression of the phase function:

$$\psi(s) = \int_{s_0}^s \frac{d\bar{s}}{\beta(\bar{s})} + \psi_0. \quad (1.5)$$

Using the betatron function $\beta(s)$ to express $\psi(s)$ in Eq. 1.3 results in

$$\frac{1}{2}\beta'\beta'' - \frac{1}{4}\beta'^2 + \beta^2 K(s) = 0. \quad (1.6)$$

The average value of the betatron function along the ring, $\langle\beta(s)\rangle$ can be used to approximate the transverse motion and is known as the *smooth approximation*. The relation between the average of the betatron function, $\langle\beta(s)\rangle$, and the total number of oscillations along the machine (the tune), Q , is:

$$2\pi Q = \oint \frac{d\bar{s}}{\langle\beta(s)\rangle} = \frac{2\pi R}{\langle\beta(s)\rangle} \Rightarrow \langle\beta(s)\rangle = \frac{R}{Q}, \quad (1.7)$$

where R is the total radius of the machine. The smooth approximation of the function $K(s)$ in Hill's equation is calculated by putting Eq. 1.7 into Eq. 1.6:

$$\langle\beta\rangle^2 K(s) = 0 \Rightarrow K(s) = \frac{1}{\langle\beta\rangle^2} = \left(\frac{Q}{R}\right)^2, \quad (1.8)$$

which results in the smooth approximation of the Hill's equation:

$$u''(s) + \left(\frac{Q}{R}\right)^2 u = 0, \quad (1.9)$$

where R is the total radius of the machine and Q is the transverse tune. [38]

1.3.2 Longitudinal Equations of motion

The equations of motion in the longitudinal plane will be derived in the coordinates z , which corresponds to distance along the beamline in relation to the position of the synchronous particle, and $\delta = \frac{\Delta p}{p}$, the momentum deviation from the synchronous particle. The following derivation of the equations of motion in the longitudinal plane is from reference [39].

In a synchrotron, such as the LHC, the nominal particle trajectory is constant meaning the aperture of the accelerator can be small. A change in particle energy therefore requires the magnets and the accelerating structures, the RF cavities, to be synchronous with the revolution frequency. The RF frequency therefore is an integer of the revolution frequency such that the synchronous particle always arrives in the RF cavity with the same phase:

$$f_{\text{RF}} = h f_{\text{rev}}. \quad (1.10)$$

The integer h is called the harmonic number. [40]

The revolution time of the synchronous particle is

$$T_0 = \frac{L_0}{v_0}, \quad (1.11)$$

where $L_0 = 2\pi R$ is the length of orbit of the synchronous particle and v_0 its velocity. Not all particles in a synchrotron will be synchronous particles. The revolution period of a particle not on the synchronous path is:

$$T = \frac{L_0 + \Delta L}{v_0 + \Delta v} = (L_0 + \Delta L) \frac{v_0 - \Delta v}{v_0^2 - (\Delta v)^2} \approx \frac{1}{v_0^2} (L_0 v_0 + v_0 \Delta L - L_0 \Delta v) \quad (1.12)$$

and thus the period difference is:

$$\Delta T = T - T_0 = \frac{v_0 \Delta L - L_0 \Delta v}{v_0^2} \Rightarrow \frac{\Delta T}{T_0} = \frac{\Delta L}{L_0} - \frac{\Delta v}{v_0}. \quad (1.13)$$

This can be approximated as the time derivative of ΔT since T_0 , the design revolution period, is small:

$$\delta \dot{T} \approx \frac{\Delta T}{T_0}. \quad (1.14)$$

The longitudinal position z is defined as the distance from the synchronous particle and is given by

$$z = \beta c \Delta T, \quad (1.15)$$

so in order to express z' , the time derivative of ΔT is to be evaluated and expressed in terms of z and δ . The relative path length difference, $\frac{\Delta L}{L}$, can be expressed in $\frac{\Delta p}{p}$ via the momentum

1.3 Vlasov method applied to e-cloud instabilities

compaction factor. The momentum compaction factor, α_c , is a machine parameter and a measure of the relative change in path length compared to the relative change in momentum [41]:

$$\alpha_c = \frac{\Delta L/L}{\Delta p/p}. \quad (1.16)$$

The relationship between the relative velocity difference, $\frac{\Delta v}{v}$ and the the relative momentum difference $\frac{\Delta p}{p}$ can be calculated from the derivative $\frac{dp}{dv}$:

$$\frac{dp}{dv} = \frac{d}{dv}(\gamma m_0 v) = m_0 \frac{d}{d\beta} \left(\frac{\beta c}{\sqrt{1-\beta^2}} \right) \frac{d\beta}{dv} = \gamma^3 m_0 \Rightarrow \Delta p = \gamma^3 m_0 \Delta v. \quad (1.17)$$

This leads to the following expression:

$$\frac{\Delta p}{p} = \gamma^2 \frac{\delta v}{v}. \quad (1.18)$$

Putting Eq. 1.18 and Eq. 1.16 into Eq. 1.13 leads to

$$(\Delta T) = \left(\alpha_c - \frac{1}{\gamma^2} \right) \frac{\Delta p}{p} = -\eta \delta, \quad (1.19)$$

where $\eta = (\frac{1}{\gamma^2} - \alpha_c)$ is the slippage factor. Finally, the time derivative of z can be found by putting Eq. 1.19 into Eq. 1.15

$$\dot{z} = \beta c \Delta T = -\beta c \eta \delta. \quad (1.20)$$

The derivative of z with respect to s relates to the time derivative \dot{z} via:

$$\frac{dz}{dt} = \frac{dz}{ds} \frac{ds}{dt} = z' \beta c, \quad (1.21)$$

which leads to the first equation of motion in the longitudinal plane:

$$z' = -\eta \delta. \quad (1.22)$$

The second equation of motion in the longitudinal plane is the derivative of δ with respect to s . This is related to the energy change per revolution. The total energy of a particle can be expressed from the momentum:

$$E = \gamma m_0 c^2 = \gamma m_0 \frac{\beta c}{\beta c} c^2 = c^2 \frac{p}{v}. \quad (1.23)$$

Differentiating E with respect to p and using the expression Eq. 1.17 together with $p = \gamma m_0 v$ gives:

$$\frac{dE}{dp} = \frac{d}{dp} \left(c^2 \frac{p}{v} \right) = c^2 \frac{v - p \frac{dv}{dp}}{v^2} = \beta c \Rightarrow \Delta E = \beta c \Delta p, \quad (1.24)$$

which together with Eq. 1.23 leads to

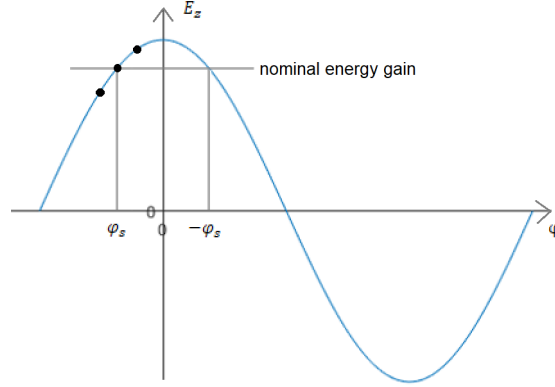


Figure 1.6: The RF voltage as a function of the phase. An example of a synchronous phase is displayed as φ_s , as well as the Voltage a particle of that phase would see. The figure is taken from [42].

$$\frac{\Delta E}{E} = \beta^2 \frac{\Delta p}{p} = \beta^2 \delta. \quad (1.25)$$

To express the derivative of δ with respect to s , the energy difference ΔE needs to be evaluated. The energy gain per turn for the synchronous particle is given by

$$E_0 = eU_0 \sin \varphi_0 - W_0, \quad (1.26)$$

where e is the elementary charge, U_0 is the peak voltage at the beam location in the RF cavity, φ_0 is the phase at which the particle enters the cavity and W_0 is how much energy the particle loses every turn due to synchrotron radiation. In a proton synchrotron, such as the LHC, W_0 is negligible. An illustrative figure of the Voltage in the cavity as a function of the phase can be seen in Fig. 1.6.

The difference in energy gain of a particle not on the synchronous phase compared to the energy gain of a particle with the synchronous phase is given by:

$$\Delta E = E - E_0 = eU_0 (\sin(\varphi_0 + \Delta\varphi) - \sin \varphi_0) \approx eU_0 (\cos \varphi_0) \Delta\varphi, \quad (1.27)$$

where $\Delta\varphi$ is the phase difference from the synchronous phase, $\varphi - \varphi_0$, and is small meaning $\sin(\varphi_0 + \Delta\varphi) - \sin \varphi_0 \approx \Delta\varphi \cos \varphi_0$. The time derivative of ΔE can be approximated by dividing with the revolution period T_0 :

$$\dot{\Delta E} = \frac{eU_0}{T_0} (\cos \varphi_0) \Delta\varphi. \quad (1.28)$$

The phase difference, $\Delta\varphi$, between an arbitrary particle and the synchronous particle is related to the time difference ΔT by:

$$\Delta\varphi = 2\pi \frac{\Delta T}{T_{\text{RF}}} = \omega_{\text{RF}} \Delta T = h\omega_{\text{rev}} \Delta T, \quad (1.29)$$

1.3 Vlasov method applied to e-cloud instabilities

which in turn is related to the longitudinal position z through:

$$z = \beta c \Delta T = \beta c \frac{\Delta \varphi}{h \omega_{\text{rev}}}, \quad (1.30)$$

where h is the harmonic number and $\omega_{\text{rev}} = \frac{2\pi}{T_0}$ is the angular revolution frequency. Using Eq. 1.25, Eq. 1.28 and Eq. 1.30 the time derivative of δ can be expressed as:

$$\frac{d\delta}{dt} = \frac{1}{\beta^2 E} \Delta \dot{E} = \beta c \frac{h e U_0 \cos \varphi_0}{2\pi E \beta^2 R^2} z = \frac{\beta c}{\eta} \left(\frac{Q_s}{R} \right)^2 z, \quad Q_s = \sqrt{\eta \frac{e U_0 h \cos \varphi_0}{2\pi \beta^2 E}}. \quad (1.31)$$

The derivative of δ with respect to s is therefore:

$$\delta' = \frac{1}{\eta} \left(\frac{Q_s}{R} \right)^2 z. \quad (1.32)$$

The full equations of motion in the longitudinal plane for small oscillation amplitude are given by Eq. 1.22 and 1.32:

$$\begin{cases} z' = -\eta \delta \\ \delta' = \frac{1}{\eta} \left(\frac{Q_s}{R} \right)^2 z \end{cases}. \quad (1.33)$$

1.3.3 Hamiltonian of the accelerator

The time derivative of the coordinate vector \mathbf{q} and the momentum vector \mathbf{p} are given by the functions f and g respectively:

$$\begin{cases} \dot{\mathbf{q}} = f(\mathbf{q}, \mathbf{p}, t) \\ \dot{\mathbf{p}} = g(\mathbf{q}, \mathbf{p}, t) \end{cases}. \quad (1.34)$$

In a system with only conservative forces, such as EM-forces without damping or diffusion, the energy of the system is referred to as the Hamiltonian \mathbf{H} . The equations of motion can be written with the Hamiltonian [43]:

$$\begin{cases} f = \frac{\partial \mathcal{H}}{\partial \mathbf{p}} \\ g = -\frac{\partial \mathcal{H}}{\partial \mathbf{q}} \end{cases} \Rightarrow \frac{\partial f}{\partial \mathbf{q}} + \frac{\partial g}{\partial \mathbf{p}} = 0. \quad (1.35)$$

From Hill's equation under the smooth approximation, Eq. 1.9, the Hamiltonian can be derived by writing the expressions for \dot{u} and \dot{u}' :

$$\begin{cases} \dot{u} = \frac{du}{dt} = \frac{du}{ds} \frac{ds}{dt} = u \cdot v = \frac{\partial \mathcal{H}}{\partial u'} \\ \dot{u}' = u'' \cdot v = -v \left(\frac{Q_{0u}}{R} \right)^2 u = -\frac{\partial \mathcal{H}}{\partial u} \end{cases}. \quad (1.36)$$

Chapter 1. Electron cloud instabilities in Large Hadron Collider

From integrating the two expressions the Hamiltonian for transverse motion is reached:

$$\mathcal{H}_{\text{trans.}} = \frac{\nu}{2} \left(u'^2 + \left(\frac{Q_{u0}}{R} \right)^2 u^2 \right), \quad (1.37)$$

where u can be either x to describe horizontal motion or y to describe vertical motion. The terms specific to each plan are u , u' , and Q_{u0} .

Similarly, the longitudinal Hamiltonian can be put together from the longitudinal equations of motion, Eq. 1.33:

$$\begin{cases} \frac{\partial \mathcal{H}_0}{\partial \delta} = \frac{dz}{dt} = \nu z' = -\nu \eta \delta \\ \frac{\partial \mathcal{H}_0}{\partial z} = \frac{d\delta}{dt} = -\nu \delta' = -\frac{\nu}{\eta} \left(\frac{Q_s}{R} \right)^2 z \end{cases}, \quad (1.38)$$

where $\nu = \frac{ds}{dt}$. This leads to the longitudinal Hamiltonian:

$$\mathcal{H}_{\text{long}} = -\frac{\nu}{2} \left(\frac{1}{\eta} \left(\frac{Q_s}{R} \right)^2 z^2 + \eta \delta^2 \right). \quad (1.39)$$

The full Hamiltonian is the sum of the three Hamiltonian's \mathcal{H}_x and \mathcal{H}_y from Eq. 1.37 and \mathcal{H}_z from Eq. 1.38:

$$\mathcal{H}_0 = \frac{\nu}{2} \left[\left(\frac{Q_{x,0}}{R} \right)^2 x^2 + x'^2 + \left(\frac{Q_{y,0}}{R} \right)^2 y^2 + y'^2 \right] - \frac{\nu}{2} \left[\frac{1}{\eta} \left(\frac{Q_s}{R} \right)^2 z^2 + \eta \delta^2 \right], \quad (1.40)$$

where $Q_{x,0}$ is the unperturbed tune in the horizontal plane, $Q_{y,0}$ is unperturbed tune in the vertical plane, Q_s is the synchrotron tune, ν is the velocity of the particles, R is the total radius of the synchrotron and η is the slippage factor.

A good choice of coordinates is the *action-angle* coordinates which simplifies the Hamiltonian [44]. In the transverse plane the action-angle coordinates are (J_u, θ_u) where u is either x or y and are related to cartesian coordinates (u, u') via:

$$\begin{cases} u = \sqrt{\frac{2J_u R}{Q_{u0}}} \cos \theta_u \\ u' = \sqrt{\frac{2J_u Q_{u0}}{R}} \sin \theta_u \end{cases}, \quad (1.41)$$

where R is the radius of the machine and Q_{u0} is the betatron tune for each plane. In the longitudinal plane the action-angle coordinates (J_z, ϕ) are defined by:

$$\begin{cases} z = \sqrt{\frac{2J_z \nu \eta}{\omega_s}} \cos \phi \\ \delta = \sqrt{\frac{2J_z \omega_s}{\nu \eta}} \sin \phi \end{cases}. \quad (1.42)$$

1.3 Vlasov method applied to e-cloud instabilities

The Hamiltonian can be simplified by a strategic choice of coordinates. A transform, for example a coordinate transform, that preserved the Hamiltonian formalism is called a canonical transformation. Canonical transformations preserve the Poisson brackets which in turn means that the Jacobian of the transformation, defined in Eq. 1.43, is symplectic. To check if a coordinate transformation is canonical one can verify that the Jacobian of the coordinate switch is symplectic. [45, 46]

$$\mathcal{J}_x = \begin{pmatrix} \frac{\partial J_x}{\partial x} & \frac{\partial J_x}{\partial x'} \\ \frac{\partial \theta_x}{\partial x} & \frac{\partial \theta_x}{\partial x'} \end{pmatrix}, \mathcal{J}_y = \begin{pmatrix} \frac{\partial J_y}{\partial y} & \frac{\partial J_y}{\partial y'} \\ \frac{\partial \theta_y}{\partial y} & \frac{\partial \theta_y}{\partial y'} \end{pmatrix}, \mathcal{J}_z = \begin{pmatrix} \frac{\partial J_z}{\partial z} & \frac{\partial J_z}{\partial \delta} \\ \frac{\partial \phi}{\partial z} & \frac{\partial \phi}{\partial \delta} \end{pmatrix}. \quad (1.43)$$

A 2x2 matrix, \mathbf{A} , is symplectic if it fulfills the criteria: [47]

$$\mathbf{A}^T \begin{bmatrix} 0 & 1 \\ -1 & 0 \end{bmatrix} \mathbf{A} = \begin{bmatrix} 0 & 1 \\ -1 & 0 \end{bmatrix}. \quad (1.44)$$

It can be shown that the coordinate switch from $(x, x', y, y', z, \delta)$ to $(J_x, \theta_x, J_y, \theta_y, r, \phi)$ is canonical. With this choice of coordinates, the Hamiltonian becomes:

$$H_0 = \omega_0 Q_{x,0} J_x + \omega_0 Q_{y,0} J_y - \omega_s J_z. \quad (1.45)$$

1.3.4 Unperturbed Vlasov Equation

The Hamiltonian of a dynamic system, such as an accelerator, can be used to calculate how a state (q_i, p_i) evolves in time to a new state (q_f, p_f) . This can also be denoted as a mapping

$$\mathcal{M} : (q, p)_i \rightarrow (q, p)_f. \quad (1.46)$$

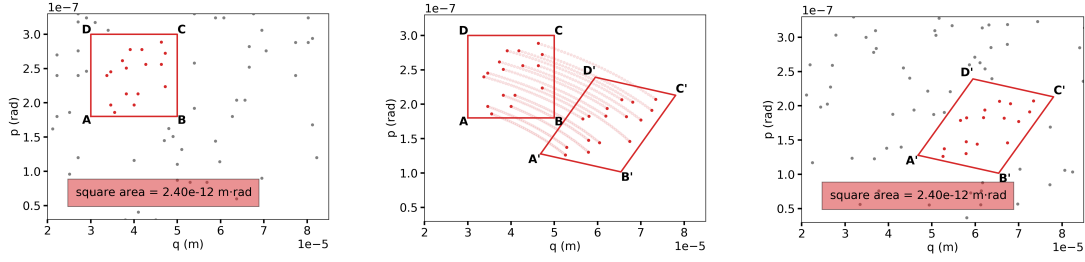
This mapping \mathcal{M} is obtained from following the Hamiltonian trajectory specified by \mathcal{H} and is symplectic. Symplectic maps preserve the volume in phase space. This conservation law is called the Liouville's theorem. [48]

To illustrate this a random distribution was generated in phase space (q, p) , and an area ABCD was selected, see Fig. 1.7a. Some of the particles are inside the area and are colored red, and some are outside and are colored grey. The time evolution is defined by a Hamiltonian, which for this illustration is:

$$\mathcal{H} = \frac{v}{2} \left[\left(\frac{Q_{y0}}{R} \right)^2 q^2 + p^2 \right], \quad (1.47)$$

which is the Hamiltonian in transverse phase space under the smooth approximation in a synchrotron. In the demonstration, a 54 km long circular synchrotron with a tune of 30.295, where the particles travel at the speed of light, is used. The choice of these parameters is arbitrary and was made to produce visible deformation in the phase space.

Chapter 1. Electron cloud instabilities in Large Hadron Collider



(a) A random distribution of particles in phase space with no duplicates at time t_i . An area ABCD of area $2.4 \cdot 10^{-12}$ m·rad is selected and all particles inside the area are colored red.

(b) The stepwise evolution of all particles in the area ABCD from time t_i to time t_f is plotted. The area ABCD is transformed to area A'B'C'D' at time t_f .

(c) The distribution in phase space in (a) transformed from t_i to t_f . The chosen red area is again $2.4 \cdot 10^{-12}$ m·rad.

Figure 1.7: A demonstration on how a distribution of particles in phase space (x, x') evolves in time in a dynamic system which can be described by a Hamiltonian.

The distribution in Fig. 1.7a were then transformed from time t_i to t_f step-wise using the Hamiltonian in Eq. 1.47 to formulate the time derivatives \dot{q} and \dot{p} using Eq. 1.34 and then approximating the time evolution with:

$$\begin{cases} q(t + \Delta t) = q(t) + \Delta t \cdot \dot{q} \\ p(t + \Delta t) = p(t) + \Delta t \cdot \dot{p} \end{cases} \quad (1.48)$$

which works for small time steps Δt . The trajectory of the particles inside the red box is plotted in Fig. 1.7b for 4% of a revolution in the machine, meaning that the total time passed is $t_f - t_i = 0.04 * T_{\text{rev}}$. The trajectory of all particles follows the same flow, eliminating any instances of crossings. In addition, the particles are all still inside the red shape, which was also transformed to the shape A'B'C'D' using the Hamiltonian map from t_i to t_f . Finally, Fig. 1.7c, shows the total particle distribution at time t_f , note that no grey particle is inside the red box. The area of the red box is the same, just as predicted by the Liouville's theorem.

The area preservation can be proven through the Hamiltonian equations, Eq. 1.35. The coordinates of the corners (A, B, C, D) and the corners of the transformed shape (A', B', C', D') are given by:

$$\begin{cases} A = (q, p) \\ B = (q + \Delta q, p) \\ C = (q + \Delta q, p + \Delta p) \\ D = (q, p + \Delta p) \end{cases} \quad \begin{cases} A' = (q + f(q, p, t)dt, p + g(q, p, t)dt) \\ B' = (q + \Delta q + f(q + \Delta q, p, t)dt, p + g(q + \Delta q, p, t)dt) \\ C' = (q + \Delta q + f(q + \Delta q, p + \Delta p, t)dt, p + \Delta p + g(q + \Delta q, p + \Delta p, t)dt) \\ D' = (q + f(q, p + \Delta p, t)dt, p + \Delta p + g(q, p + \Delta p, t)dt) \end{cases} \quad (1.49)$$

1.3 Vlasov method applied to e-cloud instabilities

The area of the box (A', B', C', D') is given by:

$$\text{area}(A'B'C'D') = |A'\vec{B}' \times A'\vec{D}'| = \Delta q \Delta p \left[1 + \frac{\partial f}{\partial q} + \frac{\partial g}{\partial p} dt \right] = \Delta q \Delta p = \text{area}(ABCD), \quad (1.50)$$

and is equal to the area of the box (A, B, C, D). Let us consider a particle density distribution, $\psi(q, p, t)$. The number of particles enclosed by the box ABCD at time t is therefore:

$$N = \psi(q, p, t) \text{area}(ABCD). \quad (1.51)$$

As time passes from t_i to t_f , the square deforms to the shape A'B'C'D' as seen in Fig. 1.7c, however, there is still the same amount of particles enclosed in the shape due to the Hamiltonian map being symplectic:

$$N = \psi(q + f dt, p + g dt, t + dt) \text{area}(A'B'C'D') = \psi(q + f dt, p + g dt, t + dt) \text{area}(ABCD) \quad (1.52)$$

The particle distribution function is therefore constant in time:

$$\psi(q, p, t) = \psi(q + f dt, p + g dt, t + dt) = \psi(q, p, t) + \frac{\partial \psi}{\partial t} dt + f \frac{\partial \psi}{\partial q} dt + g \frac{\partial \psi}{\partial p} dt \quad (1.53)$$

$$\Rightarrow \frac{\partial \psi}{\partial t} + f \frac{\partial \psi}{\partial q} + g \frac{\partial \psi}{\partial p} = 0. \quad (1.54)$$

This leads to the Vlasov equation [49]:

$$\frac{d\psi}{dt} = \frac{\partial \psi}{\partial t} + [\psi, \mathcal{H}] = 0, \quad (1.55)$$

where the Poisson Bracket has been used. The Poisson bracket is defined as:

$$\sum_{i=1}^n \frac{\partial \psi}{\partial q_i} \frac{\partial q_i}{\partial t} + \frac{\partial \psi}{\partial p_i} \frac{\partial p_i}{\partial t} = \sum_{i=1}^n \frac{\partial \psi}{\partial q_i} \frac{\partial \mathcal{H}}{\partial q_i} - \frac{\partial \psi}{\partial p_i} \frac{\partial \mathcal{H}}{\partial p_i} = [\psi, \mathcal{H}] \quad (1.56)$$

A fundamental property of Poisson brackets is that they are invariant under Canonical transformations [45].

1.3.5 First order perturbation

A perturbation of the Hamiltonian can be introduced in the Vlasov equation, Eq. 1.55. The total Hamiltonian is now:

$$\mathcal{H} = \mathcal{H}_0 + \Delta \mathcal{H}. \quad (1.57)$$

In addition, a perturbation of the particle distribution function ψ can also be introduced such that the total distribution is:

$$\psi = \psi_0 + \Delta \psi. \quad (1.58)$$

Chapter 1. Electron cloud instabilities in Large Hadron Collider

Both ΔH and $\Delta\psi$ are first-order perturbations. The Vlasov equation is now:

$$\left(\frac{\partial\psi_0}{\partial t} + [\psi_0, \mathcal{H}_0]\right) + \left(\frac{\partial\Delta\psi}{\partial t} + [\Delta\psi, \mathcal{H}_0] + [\psi_0, \Delta\mathcal{H}]\right) + [\Delta\psi, \Delta\mathcal{H}] = 0. \quad (1.59)$$

The first parenthesis is equal to zero since the unperturbed distributing ψ_0 and the unperturbed Hamiltonian \mathcal{H}_0 fulfills the Vlasov equation, Eq. 1.55. Truncating Eq. 1.59 to first order, meaning approximating $[\Delta\psi, \Delta\mathcal{H}] \approx 0$, leads to the linearized Vlasov equation truncated to first order [50]:

$$\frac{\partial\Delta\psi}{\partial t} + [\Delta\psi, \mathcal{H}_0] = -[\psi_0, \Delta\mathcal{H}]. \quad (1.60)$$

The unperturbed Hamiltonian, \mathcal{H}_0 , comes from equations of motion of the accelerator, Eq. 1.1 and Eq. 1.33 and is expressed in polar coordinates in Eq. 1.45. This describes the particle motion on the accelerator under idealized and simplified conditions. Collective effects can be introduced via the perturbation $\Delta\mathcal{H}$. From Hamiltons equations, Eq. 1.35, the derivative of $\Delta\mathcal{H}$ can be expressed as a coherent force $F_u^{\text{coh}}(z; t)$ [51]:

$$\frac{\partial\mathcal{H}}{\partial u} = -\left(\frac{du'}{dt}\right)^{\text{coh}} = -\frac{1}{m_0\gamma\beta c} \left(\frac{dp_u}{dt}\right)^{\text{coh}} = -\frac{F_u^{\text{coh}}(z; t)}{m_0\gamma\beta c}, \quad (1.61)$$

where u refers to either the horizontal coordinate x or the vertical coordinate y . The force is treated separately in x and y because the motion is uncoupled. Assuming that the force only depends on time t and the longitudinal coordinate z results in the following expression after integration with respect to u :

$$\Delta\mathcal{H} = -\frac{uF_u^{\text{coh}}(z; t)}{m_0\gamma\beta c}, \quad (1.62)$$

which in action-angle coordinates, defined in Eq. 1.41, is:

$$\Delta\mathcal{H} = -\sqrt{\frac{2J_u R}{Q_{u,0}}} \cos\theta_u \frac{F_u^{\text{coh}}(z; t)}{m_0\gamma\beta c}. \quad (1.63)$$

Additionally, the chromaticity can be introduced in the Hamiltonian by introducing a dependence of δ in the tune [49]:

$$Q_u = Q_{u,0} + Q'_u \delta, \quad (1.64)$$

where Q'_u is the linear chromaticity in either x or y plane. This is introduced after the definitions of the coordinates (J_u, θ_u) , and therefore the expressions in Eq. 1.41 do not change. It adds a dependence on δ in $\mathcal{H}_{\text{trans}}$ and derivative of the total Hamiltonian with respect to δ is now

$$\frac{\partial\mathcal{H}_0}{\partial\delta} = \frac{\partial}{\partial\delta}(\omega_0 Q'_u \delta J_u) - \frac{\partial}{\partial\delta}(\omega_s J_z) = \frac{\partial H_0^{\text{chroma}}}{\partial\delta} - \nu\eta\delta. \quad (1.65)$$

1.3 Vlasov method applied to e-cloud instabilities

Table 1.1: LHC parameters needed to estimate the derivative $\frac{\partial H_0}{\partial \delta}$.

Variable	Value
Norm. Trans. Emittance	$\sim 2 \mu\text{ m}$ [53]
Q_u	~ 60 ($Q_x = 62.27$ and $Q_y = 60.295$) [53, 54]
R	$\frac{C}{2\pi}$
C	26658.883 m [5]
η	$\sim 3.2\text{e-}4$ [5]
$\delta = \frac{\Delta p}{p} = \frac{1}{\beta^2} \frac{\Delta E}{E}$	$\sim 1\text{e-}3$ [5]

The contribution from $\mathcal{H}_{\text{chroma}}$ is

$$\frac{\partial H_0^{\text{chroma}}}{\partial \delta} = \nu \omega_0 Q'_u J_u. \quad (1.66)$$

The average transverse action is equal to the transverse emittance [52]

$$\langle J_u \rangle = \epsilon_u. \quad (1.67)$$

which together with

$$\omega_0 = \frac{\nu}{R} \quad (1.68)$$

and using the normalized emittance $\epsilon_N = \beta\gamma\epsilon$ ([39]), the smooth approximation (Eq. 1.7) and the extreme case $Q'_u = Q_{u0}$ gives :

$$\frac{\partial H_0^{\text{chroma}}}{\partial \delta} \approx \nu \frac{Q_{u0}\epsilon_N}{\beta\gamma R} \quad (1.69)$$

Let us now compare $\frac{\partial H_0^{\text{chroma}}}{\partial \delta}$ with $-\nu\eta\delta$ for the LHC using the parameters defined in 1.1:

$$\frac{\partial H_0^{\text{chroma}}}{\partial \delta} \approx \nu 10^{-10} \quad (1.70)$$

$$\frac{\partial H_{0,\text{Long.}}}{\partial \delta} \approx \nu 10^{-7} \quad (1.71)$$

$$\Rightarrow \frac{\partial H_0^{\text{chroma}}}{\partial \delta} \ll \frac{\partial H_{0,\text{Long.}}}{\partial \delta} \quad (1.72)$$

The approximation means that the chromaticity is assumed to not affect the longitudinal motion, ergo:

$$\frac{\partial H_0^{\text{chroma}}}{\partial \delta} \approx 0. \quad (1.73)$$

Chapter 1. Electron cloud instabilities in Large Hadron Collider

Another assumption that is made to solve the Vlasov equation is that the two transverse planes are uncoupled. This means that the Vlasov equation is solved for a 4D phase space (u, u', z, δ) where u is either the horizontal coordinate x or the vertical coordinate y depending on in what plane instabilities are to be evaluated. Henceforth, u will simply refer to the transverse coordinate.

The stationary distribution ψ_0 can be approximated to be uncoupled in transverse and longitudinal planes.

$$\psi_0 = f_0(J_u)g_0(J_z), \quad (1.74)$$

where the two functions are normalized with respect to the total number of particles N :

$$\begin{aligned} \int_0^\infty dJ_u f_0(J_u) &= \frac{N}{2\pi} \\ \int_0^\infty dJ_z g_0(J_z) &= \frac{1}{2\pi}. \end{aligned} \quad (1.75)$$

To express the Vlasov equation using the factorization of ψ_0 two derivatives of the unperturbed Hamiltonian are evaluated:

$$\frac{dJ_u}{dt} = [J_u, \mathcal{H}_0] = \frac{\partial \mathcal{H}_0}{\partial \theta_u} = 0 \quad (1.76)$$

and

$$\frac{dJ_z}{dt} = [J_z, \mathcal{H}_0] = \frac{\partial \mathcal{H}_0}{\partial \phi} = \frac{\partial \mathcal{H}_0}{\partial \delta} \frac{\partial \delta}{\partial \phi} + \frac{\partial \mathcal{H}_0}{\partial z} \frac{\partial z}{\partial \phi} \approx -\omega_s z \delta + \omega_s z \delta = 0, \quad (1.77)$$

where the approximation in Eq. 1.73 is used. With this approximation as well as the factorization of the unperturbed distribution ψ_0 , the Poisson brackets in the linearized Vlasov equation, Ep. 1.60, can be expressed as:

$$[\Delta\psi, \mathcal{H}_0] \approx -\frac{\partial \Delta\psi}{\partial \theta_u} \frac{\partial \mathcal{H}_l}{\partial J_u} - \frac{\partial \Delta\psi}{\partial \phi} \frac{\partial \mathcal{H}_0}{\partial J_z} \approx -\omega_0 Q_u \frac{\partial \Delta\psi}{\partial \theta_u} + \omega_s \frac{\partial \Delta\psi}{\partial \phi}. \quad (1.78)$$

Similarly, the second Poisson bracket in the linearized Vlasov equation truncated to first order is:

$$\begin{aligned} [\psi_0, \Delta\mathcal{H}] &= \frac{df_0}{dJ_u} g_0(J_z) \frac{\Delta\mathcal{H}_0}{\partial \theta_u} + f_0(J_u) \frac{dg_0}{dJ_z} \frac{\partial \Delta\mathcal{H}}{\partial \phi} = \\ &= \frac{df_0}{dJ_u} g_0(J_z) \sqrt{\frac{2J_y R}{Q_{u0}}} \sin \theta_u \frac{F_u^{\text{coh}}(z; t)}{m_0 \gamma v} + f_0(J_y) \frac{dg_0}{dJ_z} \frac{\partial \Delta\mathcal{H}}{\partial z} \frac{\partial z}{\partial \phi} \\ &\approx \frac{df_0}{dJ_u} g_0(J_z) \sqrt{\frac{2J_y R}{Q_{u0}}} \sin \theta_u \frac{F_u^{\text{coh}}(z; t)}{m_0 \gamma v}, \end{aligned} \quad (1.79)$$

where the approximation $\frac{\partial \Delta\mathcal{H}}{\partial z} \approx 0$ have been made. This approximation is valid when the

1.3 Vlasov method applied to e-cloud instabilities

transverse coherent force has little effect on the longitudinal motion [49]. The linearized Vlasov equation truncated to first order is now:

$$\frac{\partial \Delta \psi}{\partial t} - \omega_0 (Q_{u0} + \Delta Q_{\text{chrom}}) \frac{\partial \Delta \psi}{\partial \theta_u} + \omega_s \frac{\partial \Delta \psi}{\partial \phi} = - \frac{df_0}{dJ_u} g_0(J_z) \sqrt{\frac{2J_u R}{Q_{u0}}} \sin \theta_u \frac{F_u^{\text{coh}}(z; t)}{m_0 \gamma v}, \quad (1.80)$$

where $\Delta Q = Q'_u \delta$ is the detuning from chromaticity.

1.3.6 Adapting the Vlasov equation to e-cloud

The Vlasov equation can describe beam coupling impedance-driven instabilities [55], and attempts have been made to apply this approach to simulate e-cloud-driven instabilities by representing the e-cloud forces as impedances [56]. However, both dipolar forces and the betatron tune modulation along the longitudinal coordinate are required to describe the e-cloud forces in the Vlasov approach [57, 58]. A Vlasov approach including these two aspects has been introduced in [59]. The following derivation is based on the references [58, 59]. Firstly, the Vlasov equation is modified to include a detuning term from e-cloud as well as from chromaticity, $\Delta Q(r, \phi) = \Delta Q_\Phi(r, \phi) + \Delta Q_R(r)$,

$$\begin{aligned} \frac{\partial \Delta \psi}{\partial t} - \omega_0 (Q_{u0} + \Delta Q_\Phi(r, \phi) + \Delta Q_R(r)) \frac{\partial \Delta \psi}{\partial \theta_u} + \omega_s \frac{\partial \Delta \psi}{\partial \phi} = \\ - \frac{df_0}{dJ_u} G_0(r) \sqrt{\frac{2J_u R}{Q_{u0}}} \sin \theta_u \frac{F_u^{\text{coh}}(z, t)}{m_0 \gamma v}, \end{aligned} \quad (1.81)$$

where the longitudinal coordinates are now polar. The polar longitudinal coordinates are defined as follows:

$$z = r \cos \phi, \quad (1.82)$$

$$\delta = \frac{\omega_s}{v\eta} r \sin \phi. \quad (1.83)$$

It is important to note that this coordinate transformation is not canonical. However, in our subsequent equations, we will no longer use Poisson brackets, and Hamilton's equations will also be excluded from any future steps. This means that this coordinate transformation is acceptable, as discussed in [51]. In these new coordinates, the unperturbed distribution ψ_0 is

$$\psi_0(J_u, r) = f_0(J_u) G_0(r), \quad (1.84)$$

where $G_0(r)$ is normalized as:

$$\int_0^\infty dr G_0(r) = \frac{v\eta}{\omega_s} \frac{1}{2\pi} \Rightarrow \int_0^\infty dJ_z G_0(J_z) = \frac{1}{2\pi}. \quad (1.85)$$

Chapter 1. Electron cloud instabilities in Large Hadron Collider

An ansatz is made on the form of bunch distortion $\Delta\psi$ where all of the time dependence is contained in a complex exponential:

$$\Delta\psi(J_u, \theta_u, J_z, \phi, t) = e^{j\Omega t} \Delta\psi(J_u, \theta_u, J_z, \phi), \quad (1.86)$$

where j is the imaginary unit, Ω is the complex mode frequency of the bunch distortion and t is time. It is assumed that there is no coupling of the transverse plane and the longitudinal plane, such that the transverse plane can be factorized from the longitudinal plane. A Fourier expansion of the transverse angle, θ_u , is done on the time-independent part:

$$\Delta\psi(J_u, \theta_u, J_z, \phi; t) = e^{j\Omega t} \sum_{p=-\infty}^{\infty} f^p(J_u) e^{jp\theta_u} g^p(r, \phi). \quad (1.87)$$

In the longitudinal plane, the Fourier expansion of the longitudinal angle ϕ is done on the function $g^p(r, \phi) e^{jp\Delta\Phi(r, \phi)}$ where $\Delta\Phi(r, \phi)$ is an arbitrary term. This means that the term $e^{-jp\Delta\Phi(r, \phi)}$ is included in the expression of the ansatz:

$$\Delta\psi(J_u, \theta_u, J_z, \phi, t) = e^{j\Omega t} \sum_{p=-\infty}^{\infty} f^p(J_u) e^{jp\theta_u - jp\Delta\Phi(r, \phi)} \sum_{l=-\infty}^{\infty} R_l^p(r) e^{-jl\phi}. \quad (1.88)$$

The unknowns are now the functions $f^p(J_u)$ and $R_l^p(r)$. The derivatives of $\Delta\psi$ in Eq. 1.81 are now given by the following three equations:

$$\frac{\partial\Delta\psi}{\partial t} = j\Omega e^{j\Omega t} \sum_{p=-\infty}^{\infty} f^p(J_u) e^{jp\theta_u} \cdot e^{-jp\Delta\Phi(r, \phi)} \cdot \sum_{l=-\infty}^{\infty} R_l^p(r) e^{-jl\phi}, \quad (1.89)$$

$$\begin{aligned} \omega_0 (Q_{x0} + \Delta Q_\Phi + \Delta Q_R) \frac{\partial\Delta\psi}{\partial\theta_u} = \\ e^{j\Omega t} \sum_{p=-\infty}^{\infty} (jp\omega_0 (Q_{u0} + \Delta Q_\Phi + \Delta Q_R)) f^p(J_u) e^{jp\theta_u} \cdot e^{-jp\Delta\Phi(z, \delta)} \cdot \sum_{l=-\infty}^{\infty} R_l^p(r) e^{-jl\phi}, \end{aligned} \quad (1.90)$$

$$\begin{aligned} \omega_s \frac{\partial\Delta\psi}{\partial\phi} &= e^{j\Omega t} \sum_{p=-\infty}^{\infty} f^p(J_u) e^{jp\theta_u} \cdot \sum_{l=-\infty}^{\infty} R_l^p(r) \frac{\partial}{\partial\phi} e^{-j(p\Delta\Phi(r, \phi) + l\phi)} \\ &= \omega_s e^{j\Omega t} \sum_{p=-\infty}^{\infty} f^p(J_u) e^{jp\theta_u} \cdot \sum_{l=-\infty}^{\infty} R_l^p(r) \frac{\partial}{\partial\phi} e^{-j(p\Delta\Phi(r, \phi) + l\phi)} \\ &= e^{j\Omega t} \sum_{p=-\infty}^{\infty} f^p(J_u) e^{jp\theta_u} \cdot \sum_{l=-\infty}^{\infty} R_l^p(r) e^{-j(p\Delta\Phi(z, \delta) + l\phi)} \left(-jp\omega_s \frac{\partial\Delta\Phi}{\partial\phi} - jl\omega_s \right). \end{aligned} \quad (1.91)$$

1.3 Vlasov method applied to e-cloud instabilities

which means that the Vlasov equation can now be expressed as:

$$\begin{aligned}
 e^{j\Omega t} \sum_{p=-\infty}^{+\infty} f^p(J_u) e^{jp\theta_u} \cdot \sum_{l=-\infty}^{+\infty} R_l^p(r) e^{-j(p\Delta\Phi(z,\delta)+l\phi)} \\
 \times \left(j\Omega - jp\omega_s \frac{\partial\Delta\Phi}{\partial\phi} - jl\omega_s - jp\omega_0(Q_{u0} + \Delta Q_\Phi + \Delta Q_R) \right) \\
 = -\frac{df_0}{dJ_u} G_0(J_z) \sqrt{\frac{2J_u R}{Q_{u0}}} \sin\theta_u \frac{F_u^{coh}(z, t)}{m_0\gamma v}. \quad (1.92)
 \end{aligned}$$

The arbitrary term $\Delta\Phi$ can be chosen such that ΔQ_Φ is canceled in Eq. 1.92. This choice means that:

$$\frac{\partial\Delta\Phi}{\partial\phi} = -\frac{\omega_0}{\omega_s} \Delta Q_\Phi(r, \phi). \quad (1.93)$$

Now, the Vlasov equation can be written as:

$$\begin{aligned}
 e^{j\Omega t} \sum_{p=-\infty}^{+\infty} f^p(J_u) e^{jp\theta_u} e^{-jp\Delta\Phi(r,\phi)} \sum_{l=-\infty}^{+\infty} R_l^p(r) e^{-jl\phi} (j\Omega - jp\omega_0(Q_{u0} + \Delta Q_R) - jl\omega_s) \\
 = -\frac{df_0}{dJ_u} G_0(r) \sqrt{\frac{2J_u R}{Q_{u0}}} \left(\frac{e^{j\theta_u} - e^{-j\theta_u}}{2j} \right) \frac{F_u^{coh}(z, t)}{m_0\gamma v}, \quad (1.94)
 \end{aligned}$$

where the term $\sin\theta_u$ has been expressed as complex exponential. Because the right-hand side of the Vlasov equation now contains the terms $e^{j\theta_u}$ and $e^{j(-1)\theta_u}$, the left-hand side will not contain any other orders of the exponential of θ_u . To be more precise:

$$f^p(J_u) = 0 \text{ for any } p \neq \pm 1. \quad (1.95)$$

The left-hand side of Eq. 1.94 is therefore

$$\begin{aligned}
 e^{j\Omega t} (f^1(J_u) e^{j\theta_u} e^{-j\Delta\Phi(r,\phi)} \sum_{l=-\infty}^{+\infty} R_l^1(r) e^{-jl\phi} (j\Omega - j\omega_0(Q_{u0} + \Delta Q_R) - jl\omega_s) + \\
 f^{-1}(J_u) e^{j(-1)\theta_u} e^{-j(-1)\Delta\Phi(r,\phi)} \sum_{l=-\infty}^{+\infty} R_l^{-1}(r) e^{-jl\phi} (j\Omega - j(-1)\omega_0(Q_{u0} + \Delta Q_R) - jl\omega_s)). \quad (1.96)
 \end{aligned}$$

Since the complex mode frequency Ω is assumed to be close to the unperturbed frequency $\omega_0\Omega$, the following is true:

$$|j\Omega - j\omega_0(Q_{u0} + \Delta Q_R) - jl\omega_s| \ll |j\Omega + (-1)j\omega_0(Q_{u0} + \Delta Q_R) - jl\omega_s|. \quad (1.97)$$

This implies that

$$f^{-1}(J_u) \ll f^1(J_u), \quad (1.98)$$

Chapter 1. Electron cloud instabilities in Large Hadron Collider

because the coefficients of $e^{\pm j\theta_u}$ are equal in the right-hand side of Eq. 1.94, the coefficients of $e^{\pm j\theta_u}$ on the left-hand side must also equal. Therefore the assumption

$$f^{-1}(J_u) \approx 0 \quad (1.99)$$

is valid. As only one term of $f^p(J_u)$ is non-zero, the superscript is redundant and we write $f^1(J_u) = f(J_u)$. Cancelling out the exponential $e^{j\theta_u}/j$, the Vlasov equation is now given by

$$e^{j\Omega t} f(J_u) e^{-j\Delta\Phi(r,\phi)} \sum_{l=-\infty}^{+\infty} R_l(r) e^{-jl\phi} (\Omega - \omega_0(Q_{u0} + \Delta Q_R) - l\omega_s) = -\frac{df_0}{dJ_u} G_0(r) \sqrt{\frac{2J_u R}{Q_{u0}}} \frac{F_u^{coh}(z, t)}{2m_0\gamma v}, \quad (1.100)$$

which is equivalent to

$$\sum_{l=-\infty}^{+\infty} R_l(r) e^{-jl\phi} \frac{f(J_u) (j\Omega - j\omega_0(Q_{u0} + \Delta Q_R) - jl\omega_s)}{\frac{df_0}{dJ_u} \sqrt{\frac{2J_u R}{Q_{u0}}}} = -e^{-j\Omega t} e^{j\Delta\Phi(r,\phi)} G_0(r) \frac{F_u^{coh}(z, t)}{2m_0\gamma v}. \quad (1.101)$$

Seeing that the right-hand side of Eq. 1.101 does not depend in J_u , it follows that:

$$f(J_u) \propto \frac{df_0}{dJ_u} \sqrt{\frac{2J_u R}{Q_{u0}}}. \quad (1.102)$$

The proportionality constant can be absorbed into $R_l(r)$ which means that the ansatz of the bunch distortion can be expressed as:

$$\Delta\psi(J_u, \theta_u, r, \phi, t) = e^{j\Omega t} e^{j\theta_u} \frac{df_0}{dJ_u} \sqrt{\frac{2J_u R}{Q_{u0}}} \cdot e^{-j\Delta\Phi(r,\phi)} \cdot \sum_{l=-\infty}^{+\infty} R_l(r) e^{-jl\phi} \quad (1.103)$$

and the Vlasov equation can be written as:

$$\sum_{l=-\infty}^{+\infty} R_l(r) e^{-jl\phi} (\Omega - Q_{u0}\omega_0 - \omega_0\Delta Q_R - l\omega_s) = e^{-j\Omega t} e^{j\Delta\Phi(r,\phi)} G_0(r) \frac{F_u^{coh}(z, t)}{2m_0\gamma v}. \quad (1.104)$$

1.3.7 Description of the Detuning Sources

The detuning, expressed in the longitudinal coordinates (z, δ) , is modelled using two polynomial of finite degree N :

$$\Delta Q(z, \delta) = \sum_{n=0}^N A_n z^n + B_n \delta^n, \quad (1.105)$$

1.3 Vlasov method applied to e-cloud instabilities

which expressed in polar coordinates is:

$$\Delta Q(r, \phi) = \sum_{n=0}^N A_n r^n \cos^n \phi + \left(\frac{\omega_s}{v\eta} \right)^n B_n r^n \sin^n \phi. \quad (1.106)$$

This expression includes chromaticity, which is the tune dependence in the momentum δ [60]. The detuning term coming from e-cloud, briefly mentioned at the beginning of the previous section, can be decomposed into two terms:

$$\Delta Q(r, \phi) = \Delta Q_R(r) + \Delta Q_\Phi(r, \phi). \quad (1.107)$$

In other words, the detuning term is divided into a phase shift term $\Delta Q_\Phi(r, \phi)$ and a detuning with longitudinal amplitude $\Delta Q_R(r)$. The latter is defined as:

$$\Delta Q_R(r) = \frac{1}{2\pi} \int_0^{2\pi} \Delta Q(r, \phi) d\phi. \quad (1.108)$$

Expanding this equation leads to:

$$\begin{aligned} \Delta Q_R(r) &= \frac{1}{2\pi} \int_0^{2\pi} \Delta Q(r, \phi) d\phi = \frac{1}{2\pi} \int_0^{2\pi} (\Delta Q_R(r) + \Delta Q_\Phi(r, \phi)) d\phi \\ &= \frac{1}{2\pi} \int_0^{2\pi} \Delta Q_R(r) d\phi + \frac{1}{2\pi} \int_0^{2\pi} \Delta Q_\Phi(r, \phi) d\phi = \Delta Q_R(r) + \frac{1}{2\pi} \int_0^{2\pi} \Delta Q_\Phi(r, \phi) d\phi \\ &\Rightarrow \frac{1}{2\pi} \int_0^{2\pi} \Delta Q_\Phi(r, \phi) d\phi = 0. \end{aligned} \quad (1.109)$$

The remaining term, $\Delta Q_\Phi(r, \phi)$, therefore introduces no average detuning over a synchrotron period

$$\frac{1}{2\pi} \int_0^{2\pi} \Delta Q_\Phi(r, \phi) d\phi = 0, \quad (1.110)$$

but is only responsible for a phase shift as a function of longitudinal coordinates.

Integrating the expression in Eq. 1.106 gives the following expression for the detuning with longitudinal amplitude:

$$\Delta Q_R(r) = \sum_n A_n r^n \left(\frac{\bar{C}_n}{2\pi} \right) + \left(\frac{\omega_s}{v\eta} \right)^n B_n r^n \left(\frac{\bar{S}_n}{2\pi} \right), \quad (1.111)$$

where:

$$\bar{C}_n = \int_0^{2\pi} \cos^n \phi d\phi, \quad (1.112)$$

$$\bar{S}_n = \int_0^{2\pi} \sin^n \phi d\phi. \quad (1.113)$$

Chapter 1. Electron cloud instabilities in Large Hadron Collider

The phase shift term can therefore be expressed as:

$$\Delta Q_{\Phi}(r, \phi) = \sum_n A_n r^n \left(\cos^n \phi - \frac{\bar{C}_n}{2\pi} \right) + \left(\frac{\omega_s}{v\eta} \right)^n B_n r^n \left(\sin^n \phi - \frac{\bar{S}_n}{2\pi} \right). \quad (1.114)$$

Lastly, the expression for $\Delta\Phi(r, \phi)$, i.e. the phase shift term with the chosen constraint in Eq. 1.93, is expressed by integrating Eq. 1.114:

$$\Delta\Phi(r, \phi) = -\frac{\omega_0}{\omega_s} \sum_{n=1}^N r^n \left[A_n \left(C_n(\phi) - \bar{C}_n \frac{\phi}{2\pi} \right) + \left(\frac{\omega_s}{v\eta} \right)^n B_n \left(S_n(\phi) - \bar{S}_n \frac{\phi}{2\pi} \right) \right]. \quad (1.115)$$

where the function $C_n(\phi)$ and $S_n(\phi)$ are defined as:

$$C_n(\phi) = \int \cos^n \phi' d\phi', \quad (1.116)$$

$$S_n(\phi) = \int \sin^n \phi' d\phi'. \quad (1.117)$$

Using recursion, we can compute these integrals as follows:

$$C_n(\phi) = \frac{\cos^{n-1} \phi \sin \phi}{n} + \frac{n-1}{n} C_{n-2}(\phi), C_0(\phi) = \phi \text{ and } C_1(\phi) = \sin \phi \quad (1.118)$$

$$S_n(\phi) = -\frac{\sin^{n-1} \phi \cos \phi}{n} + \frac{n-1}{n} S_{n-2}(\phi), S_0(\phi) = \phi \text{ and } S_1(\phi) = -\cos \phi. \quad (1.119)$$

It is worth noting that:

$$\bar{C}_n = C_n(2\pi) - C_n(0), \quad (1.120)$$

$$\bar{S}_n = S_n(2\pi) - S_n(0). \quad (1.121)$$

1.3.8 The Coherent Force

The coherent force, used to describe the perturbation of the Hamiltonian $\Delta\mathcal{H}$ in Eq. 1.62, can be expressed using a set of real functions $h_n(z)$ which satisfy the orthogonality condition:

$$\int h_n(z) h_{n'}(z) dz = H_n^2 \delta_{n,n'}. \quad (1.122)$$

The norm of the function $h_n(z)$ is given by H_n . In this thesis, the choice of h_n functions is:

$$h_n(z) = \begin{cases} \mathcal{A}_n \cos\left(2\pi \frac{n}{2} \frac{z}{L_{\text{bkt}}}\right), & \text{if } n \text{ is even} \\ \mathcal{A}_n \sin\left(2\pi \frac{n-1}{2} \frac{z}{L_{\text{bkt}}}\right), & \text{if } n \text{ is odd.} \end{cases}, \quad (1.123)$$

where \mathcal{A}_n is the amplitude of the sinusoids and can be chosen arbitrarily. Additionally, L_{bkt} is the length of the RF bucket and the longest bunch length possible. This means that the

1.3 Vlasov method applied to e-cloud instabilities

number of oscillations along the bunch is given by $\frac{n}{2}$ and $\frac{n-1}{2}$ respectively. The function $k_n(z)$ is defined as the response, $\Delta u'$, of each bunch distortion $h_n(z)$ passing through an e-cloud.

The transverse centroid, $\bar{u}(z)$, is defined as the average transverse position of all particles in a bunch as a function of the longitudinal coordinate and can be expressed as a sum of the sinusoidal bunch distortions h_n :

$$\bar{u}(z) = \sum_{n=0}^N a_n h_n(z). \quad (1.124)$$

Note that u can be either x or y depending on whether the calculations to be done are for the horizontal or vertical plane. The coefficients are given by

$$a_n = \frac{1}{H_n^2} \int \bar{u}(z) h_n(z) dz, \quad (1.125)$$

due to the orthogonality condition in Eq. 1.122. With this expression for the coefficients a_n , the transverse centroid can be expressed as:

$$\bar{u}(z) = \sum_{n=0}^N \frac{h_n(z)}{H_n^2} \int d\tilde{z} \bar{u}(\tilde{z}) h_n(\tilde{z}). \quad (1.126)$$

From simulations, it is possible to verify that there is linear behavior, such that the kick $\Delta u'$ of an arbitrary distribution $\bar{u}(z)$ is given by [58]:

$$\Delta u'(z) = \sum_{n=0}^N a_n k_n(z) = \sum_{n=0}^N k_n(z) \int \bar{u}(\tilde{z}) \frac{h_n(\tilde{z})}{H_n^2} d\tilde{z}. \quad (1.127)$$

Using Eq. 1.61, the coherent force F_u^{coh} can be written as an expression of the kick $\Delta u'$:

$$F_u^{coh} = m_0 \gamma \beta c \frac{u'}{dt} \approx m_0 \gamma \beta c \frac{\Delta u'}{\Delta T} = \frac{m_0 \gamma (\beta c)^2}{2\pi R} \Delta u', \quad (1.128)$$

where we have set $\Delta T = T_{rev}$, which was first introduced in Eq. 1.14. Putting Eq. 1.127 into Eq. 1.128 results in:

$$F_u^{coh}(z, t) = \frac{m_0 \gamma (\beta c)^2}{2\pi R} \Delta u' = \frac{m_0 \gamma (\beta c)^2}{2\pi R} \sum_{n=0}^N k_n(z) \int \bar{u}(\tilde{z}, t) \frac{h_n(\tilde{z})}{H_n^2} d\tilde{z}, \quad (1.129)$$

The average transverse position of all particles at each longitudinal position z can be expressed with the bunch distortion $\Delta\psi$:

$$\bar{u}(z, t) = \frac{1}{\lambda_0(z)} \iint d\tilde{u} d\tilde{u}' \int d\tilde{\delta} \tilde{u} \Delta\psi(\tilde{u}, \tilde{u}' z, \tilde{\delta}, t), \quad (1.130)$$

where $\lambda_0(z)$ is the longitudinal bunch profile. The coherent force F_u^{coh} can now be expressed by putting Eq. 1.130 into 1.129:

$$F_u^{coh}(z, t) = \frac{1}{\lambda_0(z)} \frac{m_0 \gamma (\beta c)^2}{2\pi R} \iint d\tilde{u} d\tilde{u}' \iint d\tilde{z} d\tilde{\delta}' \tilde{u} \Delta\psi(\tilde{u}, \tilde{u}', \tilde{z}, \tilde{\delta}, t) \sum_{n=0}^N k_n(z) \frac{h_n(\tilde{z})}{H_n^2}. \quad (1.131)$$

To put the expression of the coherent force F_u^{coh} into the Vlasov equation, Eq. 1.104. A switch to polar coordinates is needed. Using

$$\iint d\tilde{u} d\tilde{u}' = \iint d\tilde{J}_u d\tilde{\theta}_u, \quad (1.132)$$

$$\iint d\tilde{z} d\tilde{\delta} = \frac{\omega_s}{v\eta} \iint \tilde{r} d\tilde{r} d\tilde{\phi}, \quad (1.133)$$

the expression of the coherent force F_u^{coh} in Eq. 1.131 becomes:

$$F_u^{coh}(r, \phi, t) = \frac{m_0 \gamma \beta c \omega_s}{2\pi \eta R} \iint d\tilde{J}_u d\tilde{\theta}_u \iint \tilde{r} d\tilde{r} d\tilde{\phi} \times \sqrt{\frac{2\tilde{J}_u R}{Q_{x0}}} \cos \tilde{\theta}_u \Delta\psi(\tilde{J}_u, \tilde{\theta}_u, \tilde{r}, \tilde{\phi}) \sum_{n=0}^N k_n(r \cos \phi) \frac{h_n(\tilde{r} \cos \tilde{\phi})}{\lambda_0(\tilde{r} \cos \tilde{\phi}) H_n^2}. \quad (1.134)$$

Putting the expression for the anstanz of $\Delta\psi$ in Eq. 1.103 into Eq. 1.134 gives:

$$F_u^{coh}(r, \phi, t) = \frac{m_0 \gamma \beta c \omega_s}{\pi \eta R Q_{u0}} e^{j\Omega t} \int d\tilde{J}_u \tilde{J}_u \frac{df_0}{d\tilde{J}_u} \int d\tilde{\theta}_u e^{j\tilde{\theta}_u} \cos \tilde{\theta}_u \iint \tilde{r} d\tilde{r} d\tilde{\phi} \cdot e^{-j\Delta\Phi(\tilde{r}, \tilde{\phi})} \sum_{l'=-\infty}^{+\infty} R_{l'}(\tilde{r}) e^{-jl'\tilde{\phi}} \sum_{n=0}^N k_n(r \cos \phi) \frac{h_n(\tilde{r} \cos \tilde{\phi})}{\lambda_0(\tilde{r} \cos \tilde{\phi}) H_n^2}. \quad (1.135)$$

The integral of $d\tilde{\theta}_u$ can be calculated:

$$\int_0^{2\pi} d\tilde{\theta}_u e^{j\tilde{\theta}_u} \cos \tilde{\theta}_u = \pi. \quad (1.136)$$

And the integral of $d\tilde{J}_u$ can be calculated using the norm of $f_0(u)$ in Eq. 1.75.

$$\int_0^{+\infty} d\tilde{J}_u \tilde{J}_u \frac{df_0}{d\tilde{J}_u} = [\tilde{J}_u f_0(\tilde{J}_u)]_0^{+\infty} - \int_0^{+\infty} d\tilde{J}_u f_0(\tilde{J}_u) = -\frac{N_b}{2\pi}, \quad (1.137)$$

where N_b is the number of particles in the bunch. Hence, the expression of the coherent force

is:

$$F_u^{coh}(r, \phi, t) = -\frac{N_b m_0 \gamma \beta c \omega_s}{2\pi \eta Q_{u0}} e^{j\Omega t} \iint \tilde{r} d\tilde{r} d\tilde{\phi} e^{-j\Delta\Phi(\tilde{r}, \tilde{\phi})} \times \sum_{l'=-\infty}^{+\infty} R_{l'}(\tilde{r}) e^{-j l' \tilde{\phi}} \sum_{n=0}^N k_n(r \cos \phi) \frac{h_n(\tilde{r} \cos \tilde{\phi})}{\lambda_0(\tilde{r} \cos \tilde{\phi}) H_n^2}. \quad (1.138)$$

1.3.9 Solving the Vlasov Equation

The Vlasov equation, Eq. 1.104, with the expression of the coherent force in Eq. 1.138 becomes:

$$\sum_{l=-\infty}^{+\infty} R_l(r) e^{-j l \phi} (\Omega - Q_{u0} \omega_0 - \omega_0 \Delta Q_R - l \omega_s) = -\frac{N_b \omega_s}{4\pi \eta Q_{u0}} e^{j\Delta\Phi(r, \phi)} G_0(r) \times \iint \tilde{r} d\tilde{r} d\tilde{\phi} \cdot e^{-j\Delta\Phi(\tilde{r}, \tilde{\phi})} \sum_{l'=-\infty}^{+\infty} R_{l'}(\tilde{r}) e^{-j l' \tilde{\phi}} \sum_{n=0}^N k_n(r \cos \phi) \frac{h_n(\tilde{r} \cos \tilde{\phi})}{\lambda_0(\tilde{r} \cos \tilde{\phi}) H_n^2}. \quad (1.139)$$

Multiplying both sides with $e^{j l \phi}$ and integrating over ϕ leads to:

$$R_l(r) (\Omega - Q_{u0} \omega_0 - \omega_0 \Delta Q_R - l \omega_s) = -\frac{N_b \omega_s}{8\pi^2 \eta Q_{u0}} G_0(r) \int d\phi e^{j l \phi} e^{j\Delta\Phi(r, \phi)} \times \iint \tilde{r} d\tilde{r} d\tilde{\phi} e^{-j\Delta\Phi(\tilde{r}, \tilde{\phi})} \sum_{l'=-\infty}^{+\infty} R_{l'}(\tilde{r}) e^{-j l' \tilde{\phi}} \sum_{n=0}^N k_n(r \cos \phi) \frac{h_n(\tilde{r} \cos \tilde{\phi})}{\lambda_0(\tilde{r} \cos \tilde{\phi}) H_n^2}. \quad (1.140)$$

where we have used the fact that the integral on the right-hand side of Eq. 1.139

$$\int_0^{2\pi} d\phi e^{j l \phi} e^{-j l' \phi} = 2\pi \delta_{l, l'}, \quad (1.141)$$

is equal to 0 unless $l = l'$ which is why the equation can be done for each term, $R_l(r)$, of the sum on the left-hand side separately.

We introduce the function $g_0(r)$, defined as

$$g_0(r) = \frac{\omega_s}{\beta c \eta} G_0(r). \quad (1.142)$$

The normalization of g_0 can be calculated from the normalization of $G_0(r)$:

$$\int r dr g_0(r) = \frac{\omega_s}{\beta c \eta} \int r dr G_0(r) = \frac{1}{2\pi}, \quad (1.143)$$

Thus is the same normalization used in the code DELPHI [55]. The Vlasov equation can now

Chapter 1. Electron cloud instabilities in Large Hadron Collider

be expressed as the integral equation:

$$R_l(r) (\Omega - Q_{u0}\omega_0 - \omega_0\Delta Q_R - l\omega_s) = -\frac{N_b\beta c}{8\pi^2 Q_{u0}} g_0(r) \int d\phi e^{jl\phi} e^{j\Delta\Phi(r,\phi)} \\ \times \iint \tilde{r} d\tilde{r} d\tilde{\phi} e^{-j\Delta\Phi(\tilde{r},\tilde{\phi})} \sum_{l'=-\infty}^{+\infty} R_{l'}(\tilde{r}) e^{-jl'\tilde{\phi}} \sum_{n=0}^N k_n(r \cos\phi) \frac{h_n(\tilde{r} \cos\tilde{\phi})}{\lambda_0(\tilde{r} \cos\tilde{\phi}) H_n^2}. \quad (1.144)$$

The radial functions are then expanded, as done in [57], using orthogonal functions

$$R_l(r) = W_l(r) \sum_{m=0}^{+\infty} b_{lm} f_{lm}(r), \quad (1.145)$$

where the functions f_{lm} satisfy the orthogonality condition:

$$\int f_{lm}(r) f_{lm'}(r) w_l(r) dr = F_{lm} \delta_{m,m'} \quad (1.146)$$

and $W_l(r)$ is an arbitrary function and $w_l(r)$ is an arbitrary weight function. The choice of these two functions can be made to simplify the equation. With this expansion, Eq. 1.145, we can integrate both sides of the Vlasov equation, Eq. 1.144, with

$$\int dr w_l(r) f_{lm}(r) \frac{(*)}{W_l(r)}, \quad (1.147)$$

obtaining:

$$b_{lm} (\Omega - Q_{u0}\omega_0 - l\omega_s) - \frac{\omega_0}{F_{lm}} \sum_{m'=0}^{+\infty} b_{lm'} \int dr w_l(r) \Delta Q_R(r) f_{lm}(r) f_{lm'}(r) = \\ -\frac{N_b\beta c}{8\pi^2 Q_{u0} F_{lm}} \sum_{l'm'} b_{l'm'} \sum_{n=0}^N \iint dr d\phi e^{jl\phi} e^{j\Delta\Phi(r,\phi)} w_l(r) f_{lm}(r) \frac{g_0(r)}{W_l(r)} k_n(r \cos\phi) \\ \times \iint \tilde{r} d\tilde{r} d\tilde{\phi} e^{-jl'\tilde{\phi}} e^{-j\Delta\Phi(\tilde{r},\tilde{\phi})} f_{l'm'}(\tilde{r}) \frac{W_{l'}(\tilde{r}) h_n(\tilde{r} \cos\tilde{\phi})}{\lambda_0(\tilde{r} \cos\tilde{\phi}) H_n^2}. \quad (1.148)$$

This equation can be rewritten as an eigenvalue problem. First, the matrices defined by the matrix elements $M_{lm,l'm'}$ and $\tilde{M}_{lm,l'm'}$ are defined as:

$$M_{lm,l'm'} = -\frac{N_b\beta c}{8\pi^2 Q_{u0} F_{lm}} \sum_{n=0}^N \iint dr d\phi e^{jl\phi} e^{j\Delta\Phi(r,\phi)} w_l(r) f_{lm}(r) \frac{g_0(r)}{W_l(r)} k_n(r \cos\phi) \\ \times \iint \tilde{r} d\tilde{r} d\tilde{\phi} e^{-jl'\tilde{\phi}} e^{-j\Delta\Phi(\tilde{r},\tilde{\phi})} f_{l'm'}(\tilde{r}) \frac{W_{l'}(\tilde{r}) h_n(\tilde{r} \cos\tilde{\phi})}{\lambda_0(\tilde{r} \cos\tilde{\phi}) H_n^2} \quad (1.149)$$

and

1.3 Vlasov method applied to e-cloud instabilities

$$\tilde{M}_{lm,l'm'} = \delta_{l,l'} \frac{\omega_0}{F_{lm}} \int dr w_l(r) \Delta Q_R(r) f_{lm}(r) f_{l'm'}(r). \quad (1.150)$$

The full matrices will have the following shape:

$$(N_l N_m) \times (N_l N_m), \quad (1.151)$$

where N_l is the number of l values used and N_m is the number of m values used. With the new matrix expression, the Vlasov equation reduces to an eigenvalue problem:

$$b_{lm} = (\Omega - Q_{u0}\omega_0 - l\omega_s) = \sum_{l'm'} (M_{lm,l'm'} + \tilde{M}_{lm,l'm'}) b_{l'm'}. \quad (1.152)$$

In order to solve the eigenvalue problem, the functions $f_{lm}(r)$, $w_l(r)$ and $W_l(r)$ need to be chosen and $g_0(r)$ and $\lambda_0(z)$ needs to be known. The latter two can be expressed as follows if a Gaussian longitudinal bunch distribution is assumed:

$$\lambda_0(z) = \frac{N}{\sqrt{2\pi}\sigma_b} e^{-\frac{z^2}{2\sigma_b^2}}, \quad (1.153)$$

$$g_0(r) = \frac{1}{2\pi\sigma_b^2} e^{-\frac{r^2}{2\sigma_b^2}}, \quad (1.154)$$

where σ_b is the r.m.s bunch length. The orthogonal functions $f_{lm}(r)$ are chosen to be Laguerre Polynomials [61]:

$$f_{lm}(r) = L_m^{|l|}(ar^2), \quad (1.155)$$

where the choice $a = 0.5\sigma_b^{-0.5}$ is made [58]. Choosing the right function:

$$w_l(r) = 2ar e^{-ar^2} (ar^2)^{|l|}, \quad (1.156)$$

results in the following norm coefficients of $f_{lm}(r)$:

$$F_{lm} = \frac{(|l| + m)!}{m!}. \quad (1.157)$$

Lastly, the shape function $W_l(r)$ is chosen in agreement with the DELPHI code [55]:

$$W_l(r) = \left(\frac{r}{r_b}\right)^{|l|} e^{-ar^2}. \quad (1.158)$$

All functions in the matrices $M_{lm,l'm'}$, Eq. 1.149, and $\tilde{M}_{lm,l'm'}$, Eq. 1.150, are now known which means that the eigenvalue problem in Eq. 1.152 can be solved with standard linear algebra packages, e.g. python NumPy [62].

Table 1.2: Simulation parameters for build-up simulations in LHC magnets during injection.

Parameter	Value
Beam energy	450 GeV
Bunch intensity	1.2e11 protons/bunch
Bunch length	1.2 ns
Bunch spacing	25 ns
Bunches in train	300
SEY	1.4
E_{max}	332 eV
# macro-particles	250000
magnet	LHC quadrupole

1.4 E-cloud modeling for the LHC

The e-cloud buildup in the LHC beam pipe can be modeled using the simulation code PyE-CLOUD. PyE-CLOUD is a software package designed for simulating e-clouds in particle accelerators [63]. The code has been benchmarked against measurements in the CERN accelerators [64]. PyE-CLOUD employs a Particle-In-Cell (PIC) algorithm to simulate the forces acting on electrons within particle beam chambers. It models the interactions of electrons with the particle beam and among themselves, considering various conditions such as different surface properties and the presence of magnetic fields within the beam chambers [65].

The parameters used in the build-up simulations in this thesis are listed in Tab. 1.2. The total number of electrons in the beam chamber as a function of time for an LHC quadrupole can be seen in Fig. 1.8. The total time plotted is $1.4e-6$ s, which corresponds to the passage of 56 bunches. The number of electrons in the beam chamber increases with each bunch passage until saturation is reached, as discussed in Sec. 1.2. Each bunch passage is visible in the electron population as a local maximum. The value at which the e-cloud population saturates depends primarily on the SEY of the beam chamber [66].

The electrons do not spread evenly in the beam chamber but arrange themselves after the magnetic field present in the beam chamber [67]. Figure 1.9 displays the number of electrons at each horizontal position x as a function of time in an LHC dipole, Fig. 1.9a, and in an LHC quadrupole, Fig. 1.9b, for the same beam parameters. The center of the beam pipe corresponds to $x = 0$ and both simulations use an SEY of 1.4. On the left plot, the electrons have arranged themselves away from the beam center whereas in the quadrupole, right plot, there are many electrons present in the center of the chamber. This is due to the magnetic trapping of electrons [68]. Because of this, the e-cloud in the LHC quadrupoles affects the beam dynamics more than the e-cloud in the LHC dipoles when the SEY is as low as 1.4, which is a typical value after conditioning [69].

The transverse cross-section of the e-cloud distribution after build-up saturation in an LHC quadrupole under the conditions defined in Tab. 1.2 can be seen in Fig. 1.10.

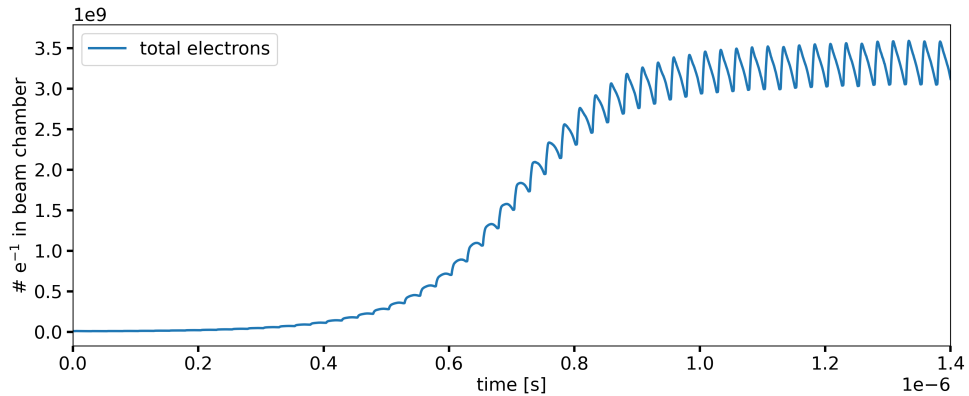


Figure 1.8: The total number of electrons in the beam chamber of an LHC quadrupole with SEY 1.4 during the passage of bunches of 1.2×10^{11} protons/bunch spaced by 25 ns.

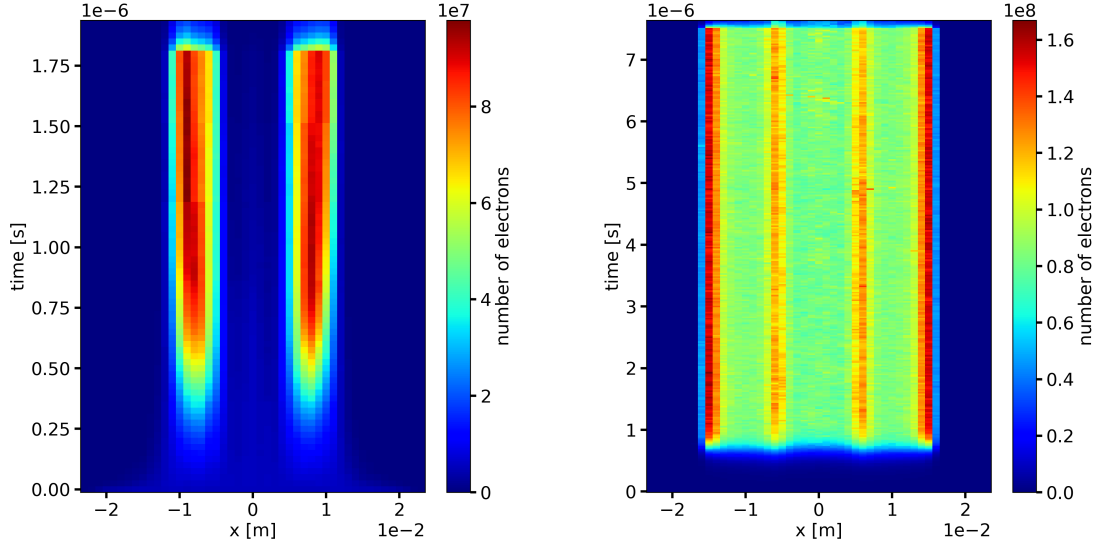
The electrons building up the LHC quadrupoles will spin around the field lines. The distribution of electrons in the beam chamber during a bunch passage in an LHC quadrupole can be seen in Fig. 1.11. The leftmost picture, Fig. 1.11a, shows the distribution before the bunch passage, Fig. 1.11b shows the distribution after a third of the bunch has passed, Fig. 1.11c after two-thirds have passed and finally Fig. 1.11d shows the distribution of electrons just after a bunch has passed through.

The electron density at the center of the beam chamber, at coordinates (0,0) is much higher after a third of the bunch has passed through compared to the right before the bunch passage, meaning this part of the bunch will experience stronger forces from the electrons compared to the head of the bunch. The e-cloud distribution in the beam chamber continues to vary as the bunch passes through meaning that the e-cloud forces acting on the bunch are dependent on the longitudinal position within the bunch.

The PyHEADTAIL code is used for simulating collective beam dynamics with macro-particle tracking [70]. The e-cloud distributions simulated with PyECLOUD can be interfaced with PyHEADTAIL to simulate the e-cloud effects on the beam dynamics [71]. In other words, the electrons act on the bunch as the bunch is passing through, which can also be modeled by PIC simulations. For a given distortion impressed to the bunch $h_n(z)$ the resulting kick from the interaction with the e-cloud, also known as a response can be simulated using PyHEADTAIL from the e-cloud distribution calculated by PyECLOUD. Simulations parameters used for this purpose can be seen in Tab. 1.3.

The set of responses $k_n(z)$ to sinusoid bunch distortions, $h_n(z)$, introduced in Eq. 1.123 were simulated using the procedure described above.

Three of the bunch distortions are plotted in black in the top plots of Fig. 1.12. In the same plots, the e-cloud density is plotted in the xz -plane. The e-cloud density at the head of the bunch, $z = 30$, the electron density is lower than at the center of the bunch $z = 0$. As expected,



(a) E-cloud buildup in LHC dipole for parameters listed in Tab. 1.2. (b) E-cloud buildup in LHC quadrupole for parameters listed in Tab. 1.2.

Figure 1.9: Number of electrons at each x-position as a function of time during a 300 bunch train passage.

a modulation of e-cloud density along the bunch is seen in all three plots.

Figure 1.12a displays the sinusoid bunch distortion, $h_1(z)$, with one oscillation along the bunch and the corresponding kick, $k_1(z)$. The kick is of a similar shape as the bunch distortion. Similarly, a sinusoid bunch distortion of five oscillations along the bunch and its response is plotted in Fig. 1.12b. The response has a higher number of oscillations along the bunch compared to the response in Fig. 1.12a and a higher amplitude. Lastly, the response to a bunch disputation with 10 oscillations along the bunch is plotted with its response in Fig. 1.12c. This response again has a higher number of oscillations along the bunch compared to Fig. 1.12b but the amplitude is lower than both previously plotted responses.

The responses to bunch distortions $h_n(z)$ for $n = 1, 2, \dots, 200$ were calculated and are used to calculate the coherent force, see Eq. 1.138 where the sum is truncated to $N = 200$. A measure of the amplitude of the responses, $k_n(z)$ is the integral:

$$\int_0^{L_{bkt}} k_n^2(z) dz, \quad (1.159)$$

and is plotted as a function of number of oscillations along the bunch, $f_n^z L_{bucket}$ in Fig. 1.13. The amplitude of the responses to the sinusoid bunch distortions and the cosine bunch distortions are plotted in orange and blue respectively. The response to bunch distortions with seven oscillations along the bunch has the highest amplitude and responses to bunch

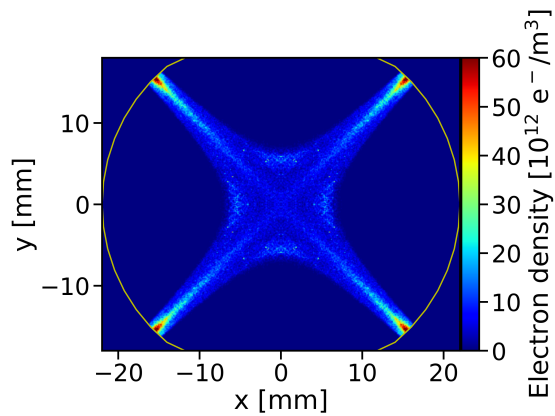
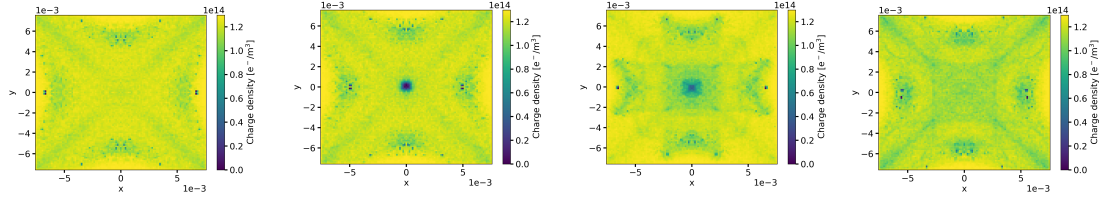


Figure 1.10: The electron distribution in the transverse cross-section of an LHC quadrupole right before a bunch passage but after saturation of the number of electrons in the chamber.

Table 1.3: Simulations parameters for generating responses from e-cloud build-up in LHC quadrupoles with a SEY of 1.4.

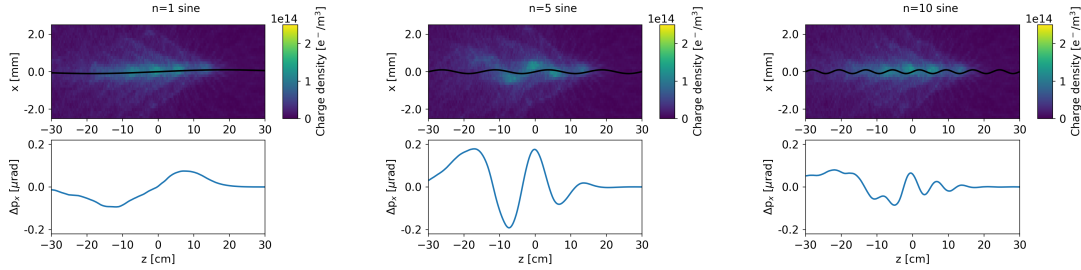
magnet with e-cloud	LHC Quadrupole
interaction points around the ring	8
octupole current	0 A
chromaticity	0
V_{RF}	6e6 V
Transverse Damper	off
# slices in along the bunch	200
Macro-particles per slice	2500
Fraction of device with magnets	7%
Magnetic field	12.1 T/m
cos and sin amplitude	1e-4
# oscillations along the bunch	0-100
Detuning fit order	10
SEY	1.4

Chapter 1. Electron cloud instabilities in Large Hadron Collider



(a) Cross section before bunch passage. (b) Cross section after a third of a bunch has passed through. (c) Cross section after two-thirds of a bunch has passed through. (d) Cross section after a bunch has passed through.

Figure 1.11: The e-cloud distribution in a transverse cross-section of an LHC quadrupole during a bunch passage.



(a) The response to a sinusoid with one oscillation along the bunch. (b) The response to a sinusoid with 5 oscillations along the bunch. (c) The response to a sinusoid with 10 oscillations along the bunch.

Figure 1.12: Calculated responses to bunch distortions $h_n(z)$.

distortions with more than 40 oscillations along the bunch have negligible amplitudes.

The found responses, $k_n(z)$, model the dipolar forces from the e-cloud as they cause the beam to be kicked. Focusing forces from the e-cloud, also known as quadrupolar forces, also act on the beam. The detuning along the bunch from the e-cloud quadrupolar forces can be simulated by displacing all particles along the bunch equally and simulating one turn using the PyHEADTAIL-PyECLOUD code. The resulting tune deviation, or detuning, along the bunch is plotted in Fig. 1.14 in blue. A polynomial of degree 10 is then fitted to the simulated ΔQ and is plotted in orange. The coefficients of this polynomial fit correspond to the coefficients A_n in 1.105.

1.4.1 E-cloud strength

The responses, k_n , and the detuning coefficients A_n are calculated for one configuration of machine and beam parameters. A quick way to vary the amount of e-cloud present in the chamber is to multiply the responses and the detuning with a factor, known as the “e-cloud strength“. An e-cloud strength of 1 corresponds to the e-cloud density calculated by the build-up simulations for the parameters specified.

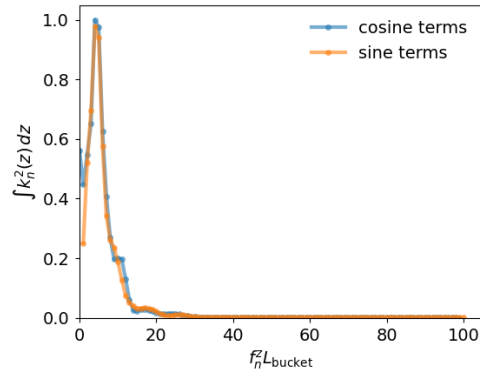


Figure 1.13: The squared amplitude of the responses, $k_n(z)$, as a function of the number of oscillations along the bunch of the corresponding bunch distortion $h_n(z)$.

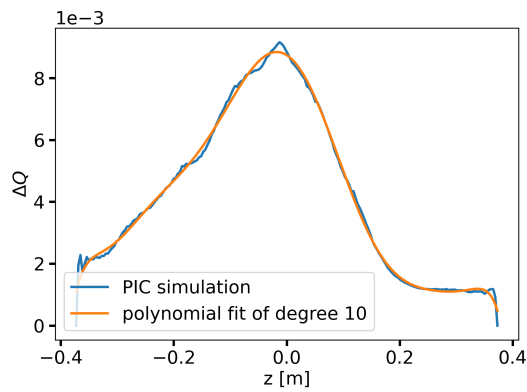


Figure 1.14: The simulated detuning along the bunch as a result of the e-cloud in LHC quadrupoles at injection.

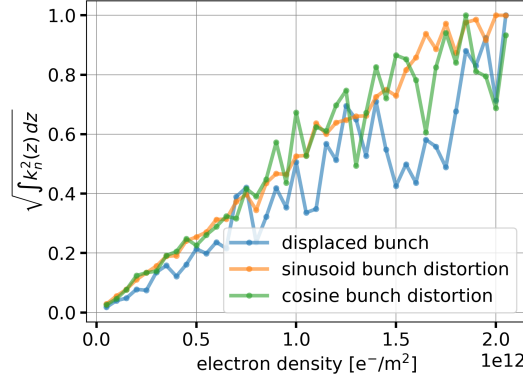


Figure 1.15: The amplitude for the response k_n as a function of electron density for three different bunch distortions.

To demonstrate what the e-cloud strength corresponds to, the amplitude of the response from a displaced bunch, a bunch with a sinusoid bunch distortion, and a bunch with cosine bunch distortion is plotted as a function of electron density in Fig. 1.15. All three curves appear to have a linear dependence on the e-cloud density. Hence, the e-cloud forces are with good approximation proportional to the e-cloud density present in the machine. This means that, to model a change in the e-cloud density, we can simply scale the response functions (and the detuning forces) with a factor that in the following we will call “e-cloud strength”.

1.5 Applying the introduced force modeling in macro-particle simulations

The force model of the e-cloud used in the Vlasov simulations can also be put into PyHEADTAIL. The dipolar forces from the e-cloud are introduced as a response matrix installed at the defined number of interaction points along the ring. The response matrix can be calculated from the responses $k_n(r)$ defined below Eq. 1.123 and plotted in Fig. 1.12 for the e-cloud formed in an LHC quadrupole of SEY 1.4 at injection.

A discretization of $h_n(z)$, defined in Eq. 1.123, along a finite amount of longitudinal slices of z defines the vectors h_n . The number of slices is chosen to be the same as the number of functions $h_n(z)$ used, N . These vectors define basis functions, not necessarily orthogonal, that can be used to describe a discretized beam distribution $x(z)$. The vector $\underline{X} = [x_1, x_2, \dots, x_N]^T$ is a discretization of $x(z)$ for N points along the z -axis. The matrix \underline{F} contains all the basis functions as column vectors and the vector $\underline{A} = [a_1, a_2, \dots, a_N]^T$ contains all coefficients for describing \underline{X} in the basis h_n . Each element in the \underline{X} vector can be calculated using the sum:

$$x_n = \sum_k^N a_k h_{kn}, \quad (1.160)$$

Chapter 1. Electron cloud instabilities in Large Hadron Collider

The response can be limited to k_0 terms by using the matrix $\underline{\underline{C}}$:

$$\underline{\underline{C}} = \begin{bmatrix} 1 & & & & & & \\ & 1 & & & & & \\ & & \ddots & & & & \\ & & & 1 & & & \\ & & & & 0 & & \\ & & & & & 0 & \\ & & & & & & 0 \end{bmatrix}. \quad (1.169)$$

Where the k_0 's row is the last row with a non-zero element, obtaining:

$$\underline{\underline{X}}' = \underline{\underline{M}} \underline{\underline{C}} \underline{\underline{A}}. \quad (1.170)$$

Replacing $\underline{\underline{A}}$ using Eq. 1.168 gives:

$$\underline{\underline{X}}' = \underline{\underline{M}} \underline{\underline{C}} \underline{\underline{F}}^{-1} \underline{\underline{C}}_{tail} \underline{\underline{X}} = \underline{\underline{W}} \underline{\underline{X}} \quad (1.171)$$

The inversion of $\underline{\underline{F}}$ can be made easier using the following manipulation:

$$\begin{aligned} \underline{\underline{X}}_{cond} &= \underline{\underline{C}}_{tails} \underline{\underline{X}} & (a) \\ \underline{\underline{X}}_{cond} &= \underline{\underline{F}} \underline{\underline{A}} & (b). \\ \underline{\underline{C}}_{tails} \underline{\underline{X}} &= \underline{\underline{F}} \underline{\underline{A}} & (c) \end{aligned} \quad (1.172)$$

Multiply both sides of (c) with $\underline{\underline{F}}^T$:

$$\underline{\underline{F}}^T \underline{\underline{C}}_{tails} \underline{\underline{X}} = \underline{\underline{F}}^T \underline{\underline{F}} \underline{\underline{A}}, \quad (1.173)$$

where we write $\underline{\underline{R}} = \underline{\underline{F}}^T \underline{\underline{F}}$. Note that if h_n are orthogonal then the matrix $\underline{\underline{R}}$ is a diagonal matrix. Solving for $\underline{\underline{A}}$ in Eq. 1.173 gives:

$$\underline{\underline{A}} = \underline{\underline{R}}^{-1} \underline{\underline{F}}^T \underline{\underline{C}}_{tail} \underline{\underline{X}}. \quad (1.174)$$

Using the cut version or $\underline{\underline{X}}'$:

$$\underline{\underline{X}}' = \underline{\underline{M}} \underline{\underline{C}} \underline{\underline{A}}, \quad (1.175)$$

gives the final relation between $\underline{\underline{X}}'$ and $\underline{\underline{X}}$: 5

$$\underline{\underline{X}}' = \underline{\underline{M}} \underline{\underline{C}} \underline{\underline{R}}^{-1} \underline{\underline{F}}^T \underline{\underline{C}}_{tail} \underline{\underline{X}}. \quad (1.176)$$

The quadrupolar forces from the e-cloud are implemented using modulated quadrupoles at each interaction point along the ring. The collective strength of each of these quadrupoles has a quadrupole strength of Δk . The change in tune from a change in quadrupole strength Δk is [60]:

$$\Delta Q = \frac{1}{4\pi} \oint \Delta k \beta(s) ds, \quad (1.177)$$

1.5 Applying the introduced force modeling in macro-particle simulations

where Δk is the strength of the modulated quadrupoles and β is the transverse beta function along the ring. Using the smooth approximation, introduced in Sec. 1.3.1, the quadrupolar strength needed to simulate a tune shift of ΔQ is

$$\Delta k = \left(\frac{4\pi}{\beta_u} \Delta Q \right) / n_{segments}, \quad (1.178)$$

where $n_{segments}$ is the number of interaction points along the ring. The expression for ΔQ from e-cloud is

$$\Delta Q = \sum_{n=1}^{N_p} A_n z^n, \quad (1.179)$$

where the coefficients A_n depend on the e-cloud distribution in the chamber, as discussed in Sec. 1.4.

2 Vlasov approach for modeling e-cloud instabilities

2.1 Beam stability in the absence of chromaticity

In this section, we first study the simplest case with only dipolar forces from e-cloud, and then we include detuning forces from the e-cloud.

The solution to the linearized Vlasov equation reduced to an eigenvalue problem is a set of Vlasov modes, each with a complex frequency Ω . The parameters used in these simulations can be seen in Tab. 2.1. An example of a solution set for the Vlasov equation for one e-cloud strength is plotted as a vertical line in Fig. 2.1a. E-cloud strength is defined in Sec. 1.4.1. In this example, only dipolar forces from e-cloud are included, meaning $\Delta Q(z, \delta) = 0$ in Eq. 1.105, and no chromaticity is included. The tune shift of the mode can be calculated from the real part of the complex frequency Ω :

$$\text{Tune Shift} = (Q - Q_0) / Q_s = \left(\frac{\Re(\Omega)}{\omega_0} - Q_0 \right) / Q_s \quad (2.1)$$

where Q_0 is the nominal tune without e-cloud, Q_s is the synchrotron tune and ω_0 is the angular revolution frequency. In Fig. 2.1a, the tune shift is plotted on the y-axis. The other defining characteristic of an instability is the instability growth rate, which is a measure of how fast the amplitude of the centroid motion grows with time. The instability growth rate can be obtained

Table 2.1: Simulation parameters of Vlasov simulations

Parameter	Value	Description
l_{\min}	-7	Minimum radial mode number
l_{\max}	7	Maximum radial mode number
m_{\max}	39	Number of azimuthal modes
n_ϕ	3-360	the number of discretized terms in calculating the integral $\int d\phi$.
n_r	3-200	the number of discretized terms in calculating the integral $\int dr$.
N_{\max}	49	the number of terms used to describe the coherent force
σ_b	0.097057	r.m.s. bunch length

Chapter 2. Vlasov approach for modeling e-cloud instabilities

Table 2.2: Simulation parameters of macroparticle simulations

Parameter	Value
number of interaction points along the ring	8
$\langle \beta_x \rangle$	92.7
$\langle \beta_y \rangle$	93.2
Q_x	62.77
Q_y	60.295
V_{RF}	6e6 V
Transverse Damper	off
Octupole Current	0 A
Bunch Intensity	1.2e11 protons/bunch
ϵ_x, ϵ_y	2.5e-6 m rad
σ_z	0.097
# slices along the bunch	200
macroparticles per slice	2500
# turns	8000
Stop condition losses	0.9
Stop condition emittance growth	0.5

as minus the imaginary part of Ω , The more negative $\Im m \Omega$, the more unstable the mode is. The color of the dots plotted in Fig. 2.1a corresponds to the instability growth rate of the Vlasov mode it represents. Looking at the vertical line at e-cloud strength = 1.0, most dots are dark blue, meaning they have zero or very low instability growth rate. They are grouped around the integer lines $(Q - Q_0)/Q_s = n, n \in \mathbb{Z}$, with some modes slightly shifted down from the integer lines. A strongly unstable mode is visible for e-cloud strength = 1 at $(Q - Q_0)/Q_s = -3$. This Vlasov mode is plotted in green, indicating an instability growth rate of about 40 s^{-1} .

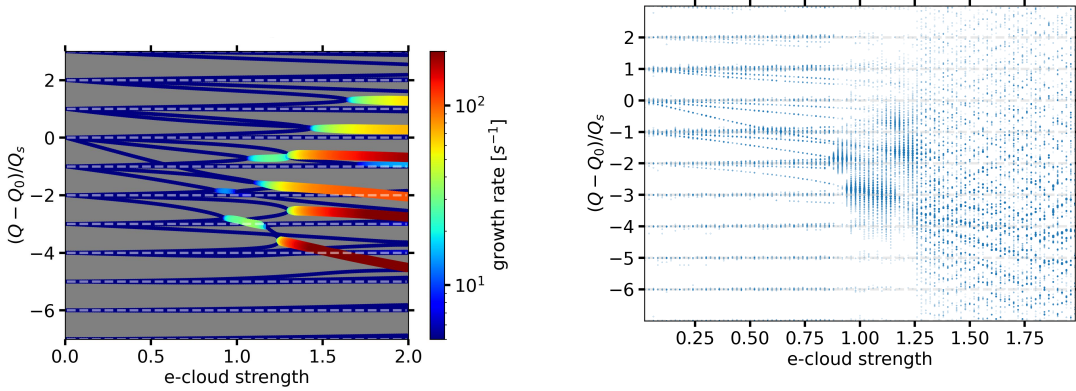
For weak e-cloud strengths in Fig. 2.1a, e-cloud strength < 0.9 all plotted Vlasov modes are deep blue representing weak instabilities with growth rates less than 1 s^{-1} . The Vlasov mode starts on the integer lines at e-cloud strength = 0, and then some of the modes start to shift down as the e-cloud strength increases. In contrast, for e-cloud strength > 1.0 , many Vlasov modes have instability growth rates $> 30 \text{ s}^{-1}$ with the most unstable one being plotted in dark red and has a tune shift starting at a bit about -4 at e-cloud strength 1.25 to a tune shift of -4.5 at e-cloud strength 2.0. All unstable modes appear to happen when two azimuthal modes meet.

The tune shift can also be obtained from macroparticle tracking simulations. The parameters of these simulations can be seen in Tab. 2.2 The spectral information from the transverse motion of the centroid bunch position is evaluated using the SUSSIX algorithm [72]. The SUSSIX spectrum of one simulation, at a fixed e-cloud strength, is plotted as a vertical line in Fig. 2.1b for the case with no detuning from e-cloud and no chromaticity. The size of the dot corresponds to the amplitude at that frequency, and the frequency is in this case measured in units of normalized tune shift $(Q - Q_0)/Q_s$. Macroparticle simulations are run for a set of

2.1 Beam stability in the absence of chromaticity

e-cloud strengths from 0 to 2 and for each strength a spectral analysis is conducted and the result is plotted as a vertical set of dots in Fig. 2.1b. The growth rate of each frequency cannot be easily calculated from the spectral data which is why no information about the instability growth rate is visible in Fig. 2.1b.

At low e-cloud strengths, i.e. e-cloud strength < 0.75 , the spectral lines are grouped around the integer lines $(Q - Q_0)/Q_s = n, n \in \mathbb{Z}$, and similarly to the modes visible in 2.1a, the visible spectral peaks shift down as the e-cloud strength is increased. At e-cloud strength 1, as predicted by the Vlasov method, a stronger mode becomes visible. Increasing e-cloud strength, one first observes a strong mode around $(Q - Q_0)/Q_s = -2$, then at $(Q - Q_0)/Q_s = -3$, then back to -2 , then finally around -3 at e-cloud strength 1.25. For higher e-cloud strengths, the instability becomes very violent, particles are lost after a small number of turns and it becomes impossible to perform an accurate spectral analysis on the tracking data.



(a) The tune-shift of all Vlasov modes at each e-cloud strength are plotted as dots. The color of the dot corresponds to the instability growth rate of that mode.

(b) The tune-shift calculated from macroparticle tracking simulations. Each dot corresponds to a frequency peak found using the SUSSIX algorithm and the size of the dot corresponds to the amplitude of that peak.

Figure 2.1: The resulting spectrograms from Vlasov simulations and macroparticle simulations where no detuning from e-cloud is included, $\Delta Q(z, \delta) = 0$

The Vlasov modes obtained from simulations including the detuning from e-cloud can be seen in Fig. 2.2. There are “fans of modes“ originating from the integer lines of $(Q - Q_0)/Q_s$, with slopes greater or equal to zero, meaning that a positive tune shift is introduced as the e-cloud strength increases. The color of each mode corresponds to the instability growth rate and the first unstable mode can be seen around e-cloud strength 0.6 for frequencies in the order of $(Q - Q_0)/Q_s = -0.5$. As the e-cloud strength increases, several unstable Vlasov modes are visible, all parallel to the top line of each mode-fan up to e-cloud strength 1.5. At this strength, two Vlasov modes with high growth rates (higher than 100 s^{-1}) can be seen at $(Q - Q_0)/Q_s = -1$ and 0. The tune shifts of these modes increase at a lower rate with e-cloud strength compared to the weaker unstable modes, which still follow the parallel lines.

In order to compare the tune shifts predicted by the Vlasov modes with the spectrum calculated

Chapter 2. Vlasov approach for modeling e-cloud instabilities

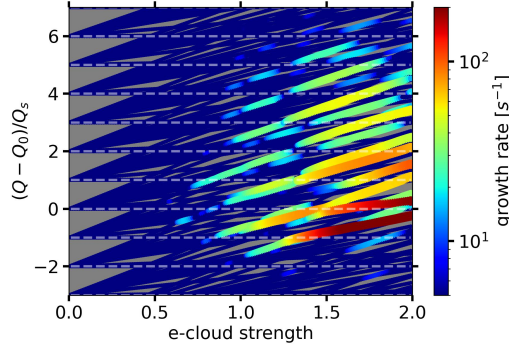


Figure 2.2: The tune-shift of all Vlasov modes at each e-cloud strength are plotted as dots for simulations with detuning from e-cloud, $\Delta Q(z, \delta) \neq 0$. The color of the dot corresponds to the instability growth rate of that mode.

from the macroparticle tracking simulations, the Vlasov modes can be plotted in the same plot as the SUSSIX spectra of the macroparticle simulations. In Fig. 2.3a, we present the same Vlasov modes as depicted in Fig. 2.1a, shown as yellow-orange dots. The color intensity of each dot corresponds to the instability growth rate, with darker shades indicating higher growth rates for the respective Vlasov mode. The same spectral information plotted in Fig. 2.1b is plotted on top of the Vlasov modes in Fig. 2.3a where the frequency with the highest amplitude is marked with a big dot for each e-cloud strength. In the region with e-cloud strengths < 1.0 , the spectral peaks from the macroparticle simulations are on top of the predicted Vlasov modes, the same grouping around $(Q - Q_0)/Q_s = n, n \in \mathbb{Z}$ is visible as well as the shift down of some modes as the e-cloud strength increases. For strong e-cloud, the only visible peak in the macroparticle spectrum follows the behavior of the strongest Vlasov mode. This is expected and it means that the Vlasov modes accurately predict the frequency of the strongest unstable mode, which dominates the bunch motion in the tracking simulation.

Figure 2.3b shows the result of simulations for e-cloud strengths in the range 0-2 with detuning forces from e-cloud, $\Delta Q(z, \delta) \neq 0$, in the absence of chromaticity. The resulting Vlasov modes are plotted in yellow-orange, where the strong modes are plotted in orange and the weak modes are plotted in yellow. These are the same modes plotted in Fig. 2.2. The spectral analysis of the macroparticle tracking simulations is again overlaid as black dots where each dot is a frequency peak calculated using the SUSSIX algorithm and the size of the plotted dot corresponds to the amplitude of that spectral component. For e-cloud strength < 0.5 , there are groups visible around the integer lines. In addition, fans of modes with positive slopes are visible in the Vlasov spectra as well as in the macroparticle spectra. In the region between e-cloud strength 0.5 and 1.5, several orange lines are visible in the Vlasov spectrum which represent several unstable modes. The spectral components visible in the macroparticle simulations follow these orange lines well. For e-cloud strengths above 1.5, several strong modes, orange dots, are visible in the Vlasov spectrum. In the spectra from the macroparticle simulations in the region of strong e-cloud only one peak is visible, marked by the black dot.

2.1 Beam stability in the absence of chromaticity

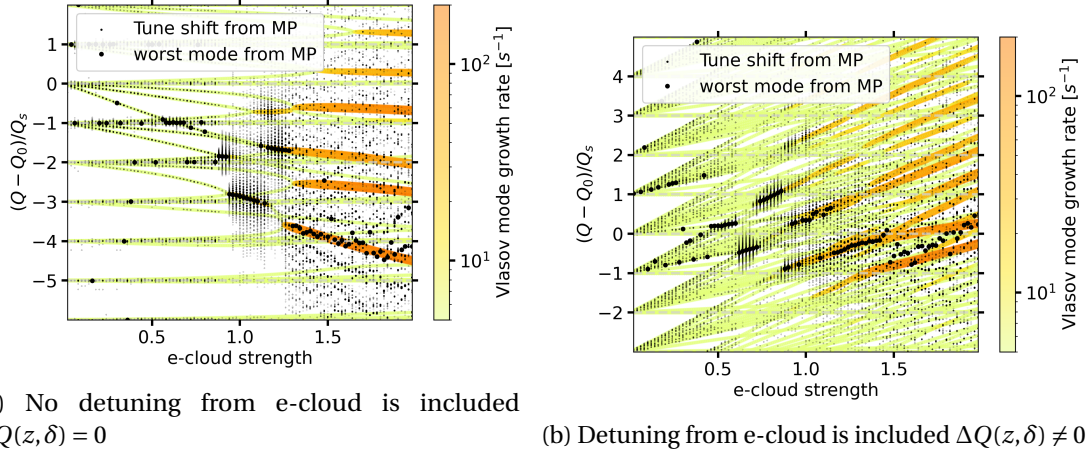


Figure 2.3: The tune shift calculated from the Vlasov approach, the dots in a yellow-orange color-map, and the spectral analysis of the macroparticle tracking simulations, black dots. The highest peak of the macroparticle spectra is marked with a big dot at each e-cloud strength.

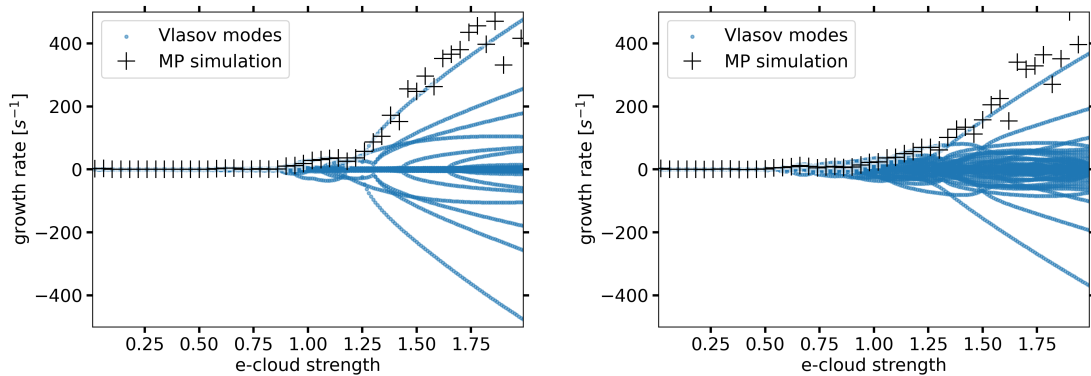
Also in this case, for higher e-cloud strengths, the instability becomes very violent, in the tracking particles are lost after a small number of turns and it becomes impossible to perform an accurate spectral analysis on the tracking data.

The instability growth rate for each Vlasov mode is minus the imaginary part of the complex frequency Ω . The growth rates, $-\tilde{\mathcal{I}}m(\Omega)$, of each Vlasov mode for the case of only dipolar forces from e-cloud and no chromaticity are plotted in Fig. 2.4a. The Vlasov modes are symmetric around $-\tilde{\mathcal{I}}m(\Omega) = 0$, meaning for every unstable Vlasov mode with a growth rate of a , where a is a positive number, there exists a Vlasov mode with a growth rate of $-a$, which is naturally damped. For low e-cloud strengths (< 1) there are no unstable Vlasov modes visible. For higher e-cloud strength (> 1) several Vlasov modes with non-zero growth rates are visible. The growth rate of the most unstable Vlasov mode, the mode with the highest growth rate at each e-cloud strength, increases with increased e-cloud strength.

The instability growth rate of the macroparticle simulations can be calculated by fitting an exponential to the tracking data of the centroid bunch position. The resulting exponent corresponds to the instability growth rate. The obtained growth rates for the simulations at each e-cloud strength are plotted as black crosses on top of the Vlasov modes. The black crosses follow the growth rate of the worst Vlasov mode for all considered e-cloud strengths.

When detuning from e-cloud is included in the model, the Vlasov modes plotted in Fig. 2.4b are obtained. Again, the Vlasov modes are symmetric around $-\tilde{\mathcal{I}}m(\Omega) = 0$, and modes with a low growth rate are visible from e-cloud strength 0.5. The growth rate of the worst Vlasov mode increases with e-cloud strengths. Compared to Fig. 2.4a, weaker modes are visible for e-cloud strengths > 1 . The instability growth rate obtained from doing an exponential fit on the centroid bunch from the macroparticle tracking simulations is plotted as black crosses and is found to follow the growth rate of the worst Vlasov mode.

Chapter 2. Vlasov approach for modeling e-cloud instabilities



(a) No detuning from e-cloud is included $\Delta Q(z, \delta) = 0$. (b) With detuning from e-cloud is included $\Delta Q(z, \delta) \neq 0$.

Figure 2.4: The negative imaginary part of the complex mode frequency of the Vlasov modes at each e-cloud strength are plotted as blue dots. The instability growth rate from macroparticle tracking simulations is plotted as a black cross at each e-cloud strength.

The worst Vlasov mode in Fig. 2.4a has a higher growth rate compared to the worst Vlasov modes in Fig. 2.4b. For e-cloud strength 2.0, the growth rate of the worst Vlasov mode is 500 s^{-1} in the left plot and 400 in the right plot of 2.4. This indicates that the detuning forces from e-cloud have a slightly stabilizing effect on the worst Vlasov mode. However, as previously mentioned, weaker modes appear in the presence of detuning from e-cloud, which are not present when only dipolar forces are included in the model.

To illustrate the accuracy of the performed fit, Fig.2.5 shows the bunch centroid motion for different macroparticle simulations, the corresponding rise time fit and the growth rate for the strongest mode as obtained from the Vlasov method.

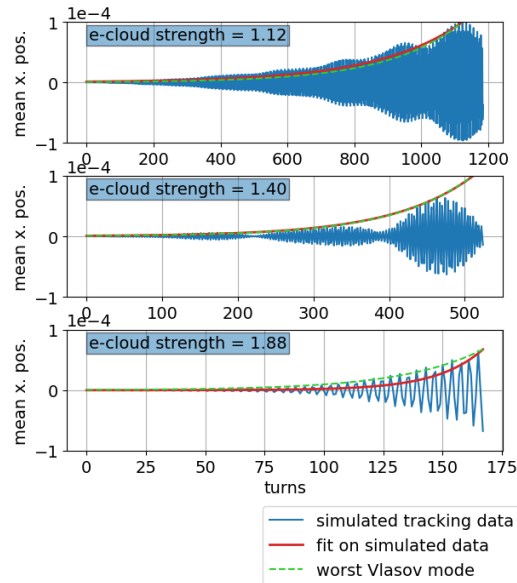


Figure 2.5: The turn-by-turn transverse position from the macroparticle tracking simulations is plotted in blue. The exponential fit of the tracking data is plotted in red and the predicted growth exponential from the Vlasov approach is plotted in green.

2.2 Effect of chromaticity

In this section, the complexity of the simulations is increased by adding the effect of chromaticity from the lattice. Simulation results with and without detuning from e-cloud will be discussed.

The growth rates from Vlasov simulations, plotted in blue, and the instability growth rate obtained from macroparticle simulations, black crosses, can be seen in Fig. 2.6a for the case with no detuning forces from e-cloud, $\Delta Q(r, \delta) = 0$, and for chromaticity -10 . In this case, the Vlasov modes are not symmetric around $-\Im m(\Omega) = 0$. In addition, a larger number of weakly unstable modes are visible compared to the case with zero chromaticity in Fig. 2.4a. An asymmetry of the instability growth rates around zero is also visible in the case with detuning from e-cloud plotted in Fig. 2.6b. The worst Vlasov mode has a higher growth rate when $\Delta Q(r, \delta) = 0$. In both cases, $\Delta Q(r, \delta) = 0$ and $\Delta Q(r, \delta) \neq 0$, the instability growth rate of the corresponding macroparticle tracking simulations, plotted as black crosses in Fig. 2.6a and Fig. 2.6b, are consistent with the growth rate of the worst Vlasov mode.

The results of simulations with chromaticity $= 10$ can be seen in Fig. 2.6c for no detuning from e-cloud and in Fig. 2.6d with detuning from e-cloud. The Vlasov modes in both figures are asymmetric around the x-axis, with a tendency for negative growth rates. This is the opposite of the asymmetry in growth rates visible in Fig. 2.6a and Fig. 2.6a indicating that negative chromaticity has a destabilizing effect on the Vlasov modes and that positive chromaticity has a stabilizing effect. In addition, the worst Vlasov mode has a higher growth rate when

Chapter 2. Vlasov approach for modeling e-cloud instabilities

$\Delta Q(r, \delta) = 0$ compared to when $\Delta Q(r, \delta) \neq 0$.

The instability growth rates from the macroparticle tracking simulations, black crosses, follow the worst Vlasov mode in Fig. 2.6c but not in 2.6d. In the latter, several Vlasov modes have a higher growth rate than observed in the macroparticle simulations for e-cloud strengths in the interval 0.75 to 1.5. Similarly, for stronger chromaticity, see the results from chromaticity 15 in Fig. 2.6e and Fig. 2.6f, the instability growth rate of the macroparticle simulations follows the growth rate of the worst Vlasov mode when no detuning from e-cloud is included but does not follow the worst Vlasov mode when the detuning term is included. In this case, Fig. 2.6f, no strong instabilities are visible in the macroparticle simulations until e-cloud strength 1.75, whereas weak Vlasov modes of increasing growth rates are visible for e-cloud strength > 0.5 . This indicates that the Vlasov modes overestimate the growth rate of the instabilities present in the macroparticle simulations for positive chromaticity when the detuning term, $\Delta Q(r, \delta)$, from the e-cloud is included in the simulations.

In order to investigate the discrepancy between the calculated instability growth rate from the macroparticle tracking data and the instability growth rate predicted by the worst Vlasov mode, a few individual simulations are plotted in Fig. 2.7 all with chromaticity = 15. Figure 2.7a displays the tracking data, blue, from the macroparticle simulations for three simulations where the e-cloud strength is set to 0.76, 1.20, 1.94 respectively, in the absence of detuning from e-cloud (meaning $\Delta Q(r, \delta) = 0$). For all three e-cloud strength values, the tracking data displays exponential growth behavior. The fit of the tracking data is plotted in red and an exponential with the growth rate predicted by the Vlasov simulations is plotted in green. Both the red and the green curves follow the behavior of tracking data for all three e-cloud strengths.

Similarly, the tracking data of the same three e-cloud strengths, 0.76, 1.20 and 1.94, are plotted in Fig. 2.7b for the cases with chromaticity = 15 and the detuning from e-cloud, $\Delta Q(r, \delta) \neq 0$. The fit for the tracking data is again plotted in red and the predicted instability from the Vlasov approach is plotted in green. Evidently, the growth rate obtained with the Vlasov method is higher than the growth rate from the macroparticle tracking data. The difference is larger for lower e-cloud strengths. It is evident that the discrepancy between the instability growth rate calculated from the macroparticle simulations and the instability growth rate predicted by the Vlasov approach cannot be explained by an error in the fit of the tracking data.

The resulting tune shift calculated using the Vlasov approach for e-cloud strengths 0 to 2 can be seen in Fig. 2.8. The results obtained for a negative chromaticity of -10 can be seen in Fig. 2.8a, where no detuning from e-cloud present, and in Fig. 2.8b, where detuning from e-cloud is included. In both of these plots, there are Vlasov modes at e-cloud strength 0.2 visible as turquoise dots, which indicates that these modes are unstable with an instability growth rate of about 20 s^{-1} . For this e-cloud strength, several unstable modes can be seen in Fig. 2.8a and no one mode is dominating until e-cloud strength 0.75, where a Vlasov mode at $(Q - Q_0)/Q_s = -2.5$ becomes dominant with a growth rate close to 100 s^{-1} . Similarly, unstable modes can be seen at e-cloud strength 0.2 in Fig. 2.8b, where $\Delta Q(r, \delta) \neq 0$. For this case, one

2.2 Effect of chromaticity

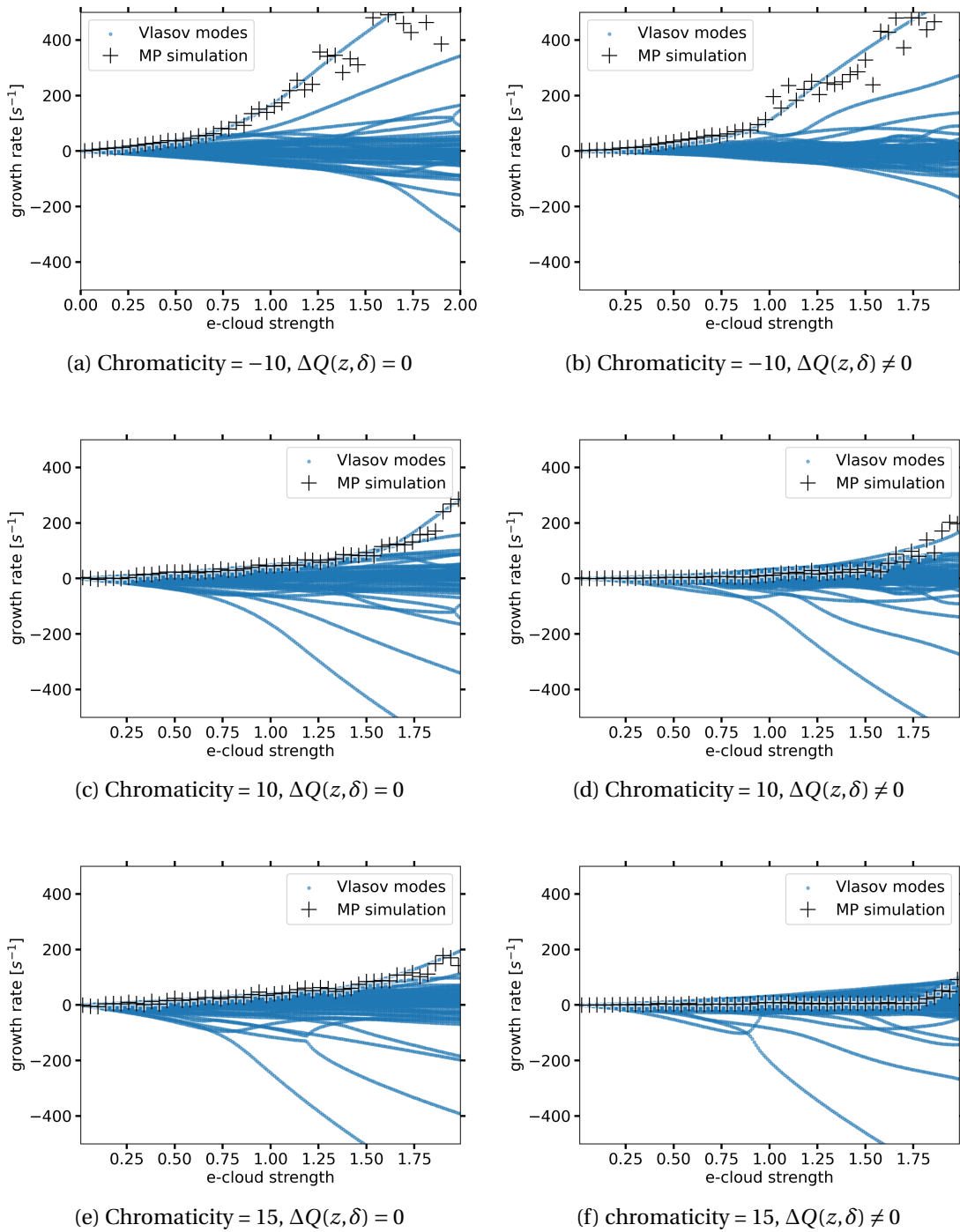


Figure 2.6: The resulting growth rates from Vlasov simulations, blue dots, and the instability growth rate obtained from macroparticle simulations, black crosses, for chromaticity -10 , 10 , and 15 . The left plots display the results of using only dipolar forces from e-cloud and the right plots display the results of including detuning from e-cloud, $\Delta Q(r, \delta)$.

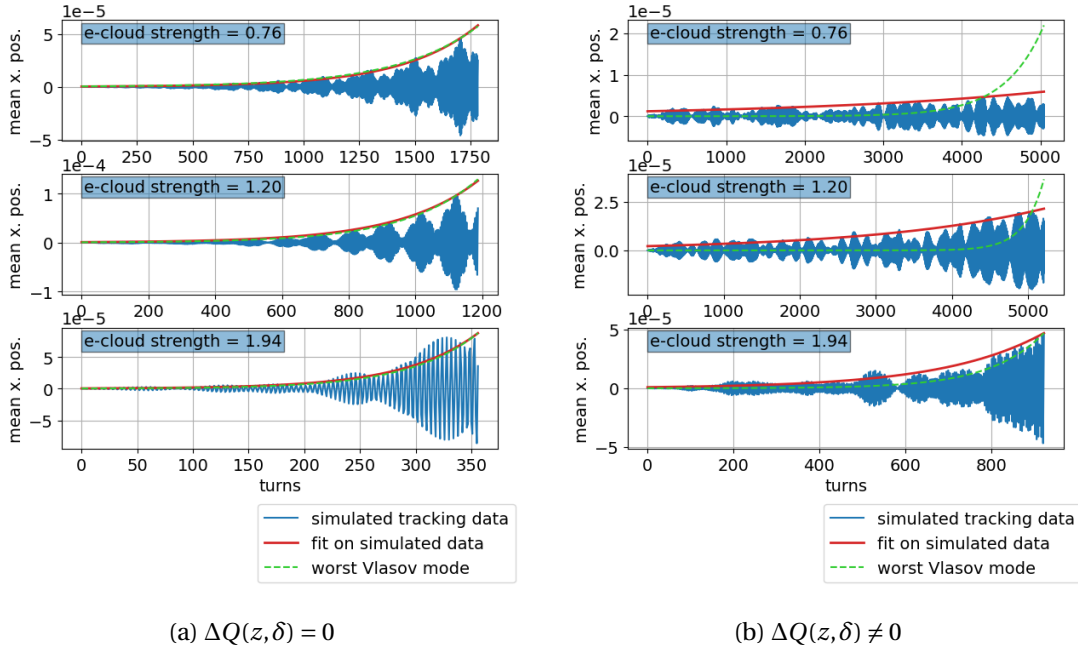


Figure 2.7: The tracking data from macroparticle simulations is plotted in blue, the fit of the tracking data is plotted in red and an exponential with the growth rate of the worst Vlasov mode is plotted as green. Chromaticity is set to 15 in all simulations.

Vlasov mode, the mode close to $(Q - Q_0)/Q_s = -1$, is stronger than the other modes. It is important to note that modes become unstable for lower e-cloud strengths than for the cases with zero chromaticity seen in Fig. 2.1a and in Fig. 2.2, and that no evident mode coupling is observed.

Vlasov simulations with chromaticity 10 results in the modes displayed in Fig. 2.8d for $\Delta Q(r, \delta) = 0$ and Fig. 2.8d for $\Delta Q(r, \delta) \neq 0$. Unstable modes of similar strengths can be seen, in Fig. 2.8c, on the integer lines -5 to 2 of $(Q - Q_0)/Q_s$ from e-cloud strength 0.5 to 1.0 . A strong unstable mode, with a growth rate of 200 s^{-1} , can be seen on the integer line $(Q - Q_0)/Q_s = -5$ at e-cloud strength 1.75 . Similarly, several unstable modes can be seen in Fig. 2.8d for e-cloud strengths higher than 0.5 , the modes are approximately parallel to each other but do not stay on the integer lines.

Benchmarks of the Vlasov modes tune shift compared to the spectral analysis of the macroparticle tracking simulations can be seen in Fig. 2.9 for the same three values of chromaticity plotted in 2.6, where a discrepancy between the two models was identified for positive chromaticity and $\Delta Q(r, \delta) \neq 0$. The plots on the left in Fig. 2.6 contain results from simulations with $\Delta Q(r, \delta) = 0$ while the plots on the right contain results from simulations with $\Delta Q(r, \delta) \neq 0$. The spectral lines from the macroparticle simulations are plotted as black dots where the size of the dot corresponds to the amplitude of the corresponding frequency component and the highest line for each e-cloud strength is marked with a big dot. The tune shift of the Vlasov modes is

2.2 Effect of chromaticity

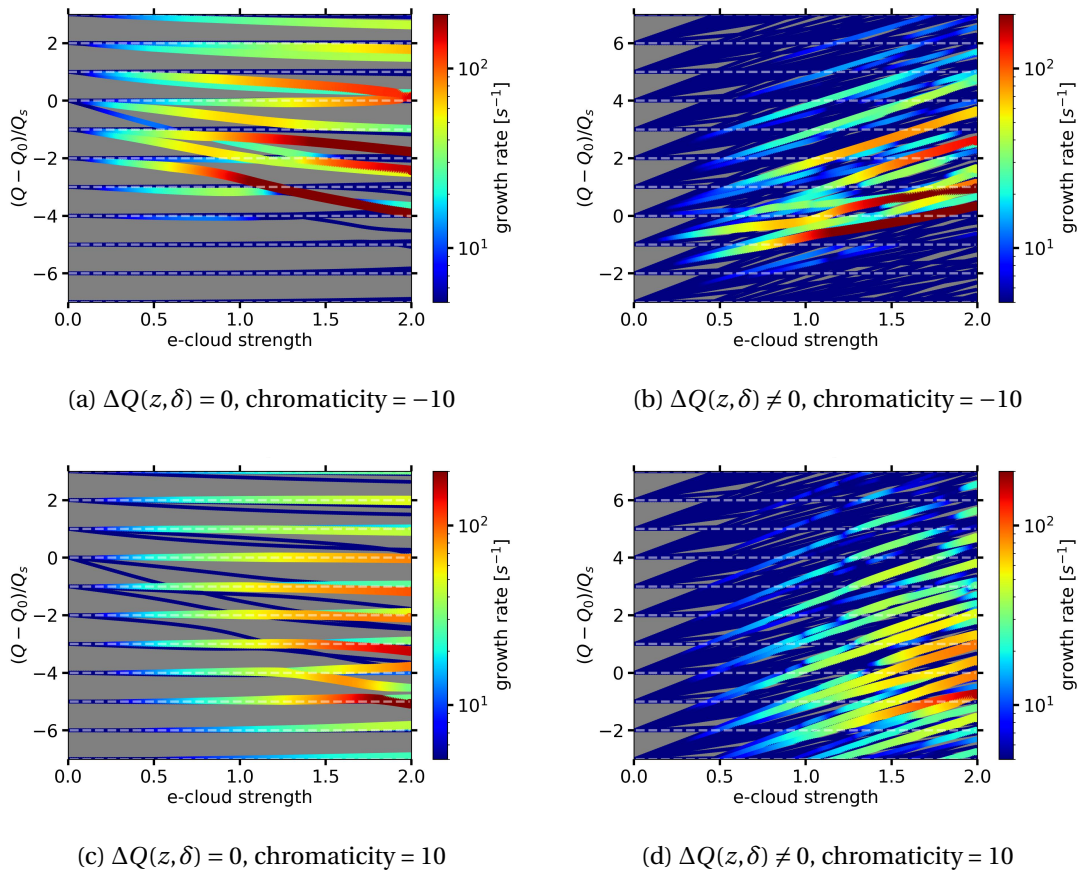


Figure 2.8: The tune shift of the calculated Vlasov modes in units of the synchrotron tune Q_s for chromaticity -10 and chromaticity 10 for simulations including or excluding the detuning term from e-cloud, $\Delta Q(r, \delta)$.

Chapter 2. Vlasov approach for modeling e-cloud instabilities

plotted in yellow-orange with the color corresponding to the growth rate of each mode. In Fig. 2.9a, several peaks are visible from the macroparticle spectrum for e-cloud strengths 0 to 0.5, and all of these peaks follow an expected Vlasov mode. At e-cloud strengths greater than 0.5, only one clear peak is visible in the macroparticle spectra and it follows the tune shift of the strongest Vlasov mode starting at $(Q - Q_0)/Q_s = -2$ and shifting down to $(Q - Q_0)/Q_s = -4$ at e-cloud strength 2. At high e-cloud strength, the macroparticle simulations contain too few turns to do an accurate spectral analysis.

In Fig. 2.9c and Fig. 2.9e the strongest spectral lines from the macroparticle simulations mostly follow the integer lines of $(Q - Q_0)/Q_s$, just as the strong Vlasov modes. Similarly, in Fig. 2.9d and Fig. 2.9f, the spectral lines plotted in black follow the same slope as the Vlasov modes. The frequency peaks from the macroparticle simulations follow the tune shift of the Vlasov modes in all six figures meaning the two simulation modes are in agreement about the expected spectral component of the bunch motion, even for positive chromaticity and with the detuning term from e-cloud, where a discrepancy on the rise time had been observed.

In summary, the Vlasov approach accurately predicts the behavior of the e-cloud driven instabilities in the macroparticle tracking simulations for chromaticity in the range -10 to 25 when only dipolar forces are included. There is also agreement between the two simulation methods for negative or zero chromaticity when the detuning term from e-cloud, $\Delta Q(r, \delta)$, is included. The agreement is in both tune shift and growth rate.

In order to further analyse the behavior depending on the chromaticity, the growth rate of both simulation approaches is plotted as a function of chromaticity for three e-cloud strengths in Fig. 2.10 in the presence of detuning forces from the e-cloud.

For all cases the agreement between the two methods is very good up to a certain value up to a the value of chromaticity marked by the vertical line. Above such value no dominant mode is identified by the Vlasov and in the macroparticle simulations the beams tends to be more stable than indicated by the Vlasov.

2.2 Effect of chromaticity

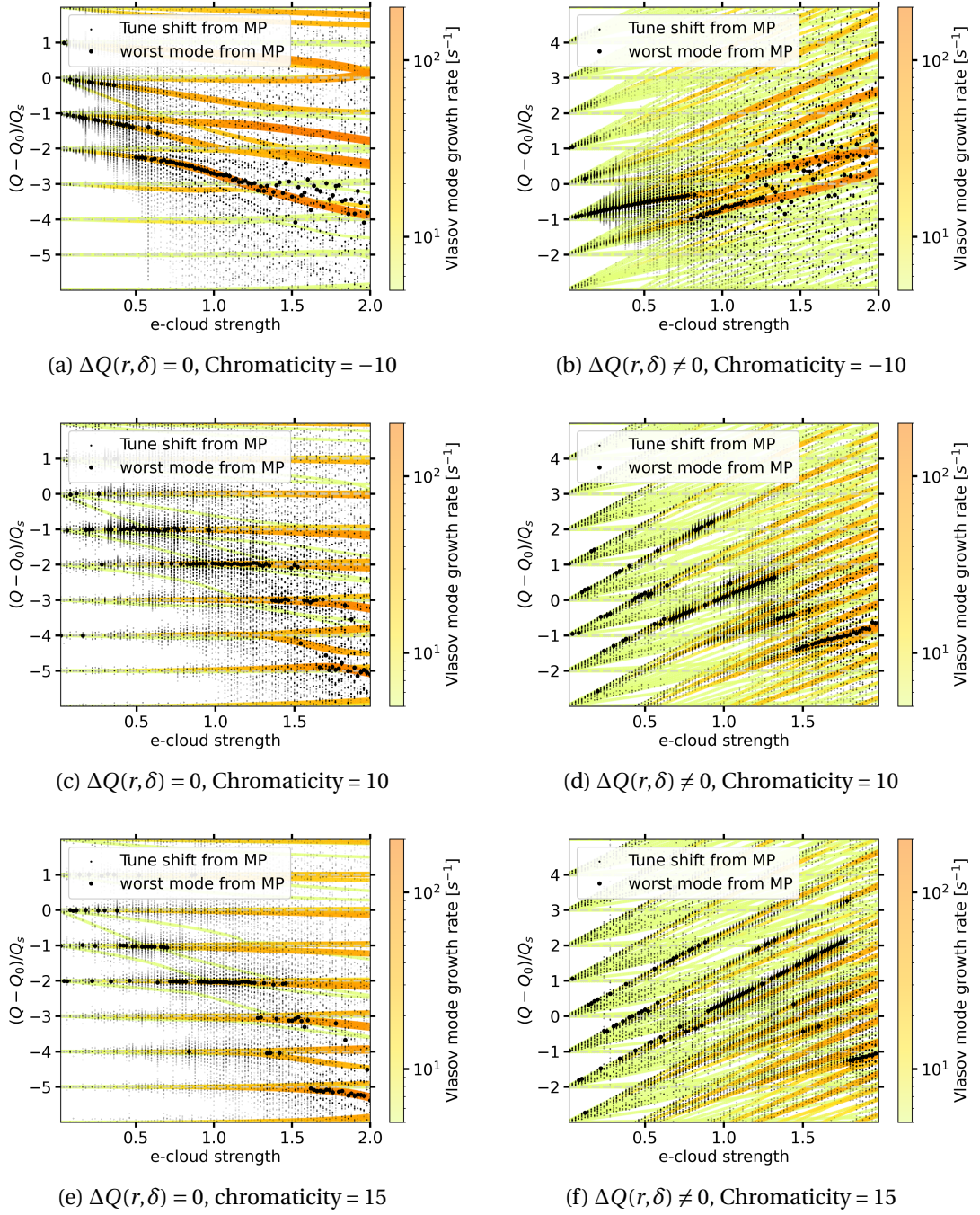


Figure 2.9: The tune shift calculated from the Vlasov approach, is plotted as yellow-orange dots, and the spectral analysis of the macroparticle tracking simulations, black dots. The highest peak of the macroparticle spectra is marked with a big dot at each e-cloud strength. The plots on the left hand side contains the results from simulations without detuning from e-cloud for chromaticity -10, 10 and 15. The plots on the right hand side contains the result from simulations including detuning from e-cloud, for the same three values of chromaticity.

Chapter 2. Vlasov approach for modeling e-cloud instabilities

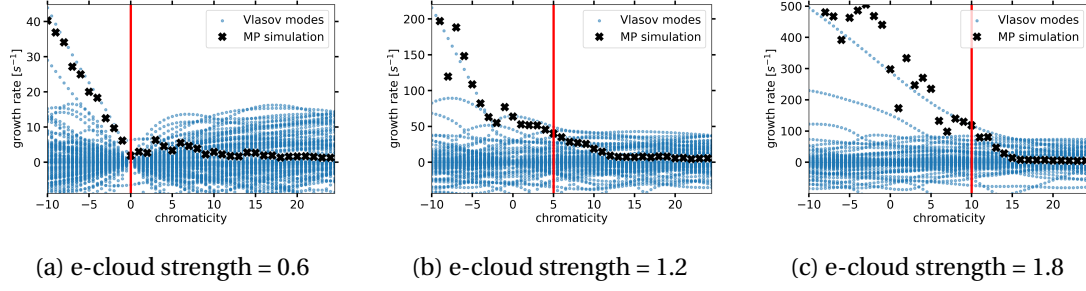


Figure 2.10: The instability growth rates of all Vlasov modes, plotted in blue, and the instability growth rates of macroparticle simulations, plotted in black, as a function of chromaticity for three different e-cloud strengths. The simulations agree for chromaticities to the left of the vertical red line.

2.3 Study the detuning term

2.3.1 Splitting the detuning function in two

The discrepancy between the macroparticle simulations and the Vlasov simulations only occurs when the detuning from e-cloud, as well as positive chromaticity, are included in the simulations. For this reason, the effects of the detuning term from e-cloud, $\Delta Q(r, \delta)$, will be more closely examined in the next section.

From Sec. 1.3.7 we know that the detuning from external forces can be expressed as a polynomial that depends on the longitudinal coordinates z and δ . The terms coming from the e-cloud forces are contained in the polynomial of z . Chromaticity also contributes to a detuning along the bunch and its contribution is contained in the term $Q'\delta$ where Q' is the chromaticity.

$$\Delta Q(z, \delta) = Q'\delta + \sum_{n=0}^{N_p} A_n z^n \quad (2.2)$$

The full detuning, containing contributions from both chromaticity and e-cloud forces, is then decomposed in two different terms after switching to polar coordinates in the longitudinal plane (r, ϕ) :

$$\Delta Q(r, \phi) = \Delta Q_R(r) + \Delta Q_\Phi(r, \phi) . \quad (2.3)$$

The term $\Delta Q_R(r)$ is the **detuning with longitudinal amplitude** and is defined as the average of the full $\Delta Q(r, \phi)$ over all angles ϕ . This term has no contribution from linear chromaticity:

$$\Delta Q_R(r) = \frac{1}{2\pi} \int_0^{2\pi} \Delta Q(r, \phi) d\phi . \quad (2.4)$$

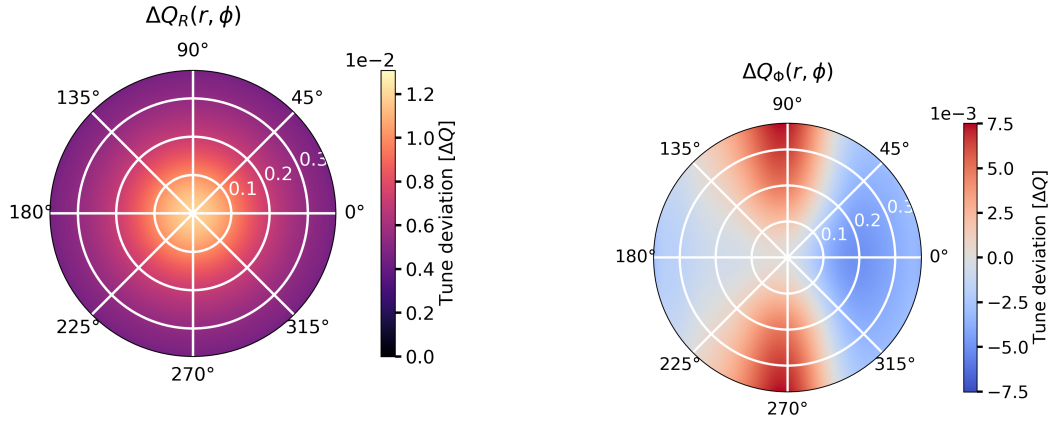
The remaining term, $\Delta Q_\Phi(r, \phi)$, introduces no average detuning over a synchrotron period, as seen in Eq. 2.5, but is only responsible for a **phase shift** as a function of longitudinal coordinates.

2.3 Study the detuning term

$$\frac{1}{2\pi} \int_0^{2\pi} \Delta Q_\Phi(r, \phi) = 0. \quad (2.5)$$

Figure 2.11a shows an example of the detuning with longitudinal amplitude, $\Delta Q_R(r)$, from e-cloud forces in plotted in polar coordinates (r, δ) . The plot is cylindrically symmetric with a peak in the middle of $\Delta Q = 1.2e-2$ and the edges have values close to $0.4e-2$. As expected, there is no dependence on the angle ϕ and no discontinuities.

An example of the head-tail phase shift, $\Delta Q_\Phi(r, \phi)$, from e-cloud can be seen in Fig. 2.11b. This plot is not cylindrically symmetric but instead has two peaks and two valleys. One peak follows the $\phi = 90^\circ$ line and the other peak follows the $\phi = 270^\circ$ line, moreover, the peak becomes stronger with increasing radius r . The two valleys are of different depths, the more shallow one following the $\phi = 180^\circ$ line and the more deep valley following the $\phi = 0^\circ$ line. No discontinuities are visible.



(a) An example of $\Delta Q_R(r)$ from the e-cloud in LHC quadrupoles plotted in longitudinal polar coordinates (r, δ) . This term has no contribution from linear chromaticity.

(b) An example of $\Delta Q_\Phi(r, \phi)$ from the e-cloud in LHC quadrupoles plotted in longitudinal polar coordinates (r, δ) . No chromaticity is included.

Figure 2.11: The figure displays the detuning along the bunch, $\Delta Q(r, \phi)$, caused by the e-cloud in an LHC quadrupole divided into a detuning with longitudinal amplitude and a phase shift plotted using longitudinal polar coordinates (r, ϕ) .

Including a chromaticity of $Q' = 10$ does not change the detuning with longitudinal amplitude, $\Delta Q_R(r)$. Chromaticity does however introduce a second phase shift term, $\Delta Q_{\Phi, Q'}(r, \phi)$ and this term for chromaticity 10 is plotted in Fig. 2.12. The tune shift is positive in the interval $0^\circ < \phi < 180^\circ$ with a maximum at $\phi = 90^\circ$ at high radius, whereas the tune shift is negative for $180^\circ < \phi < 360^\circ$ with a minimum at high r for $\phi = 270^\circ$. It differs from the phase shift from e-cloud forces since only one peak and one valley is present compared to the double amount of peaks and valleys present in the detuning term from e-cloud. The amplitude of the peak in the phase shift from chromaticity is about twice as high as the peaks in the phase shift term from e-cloud.

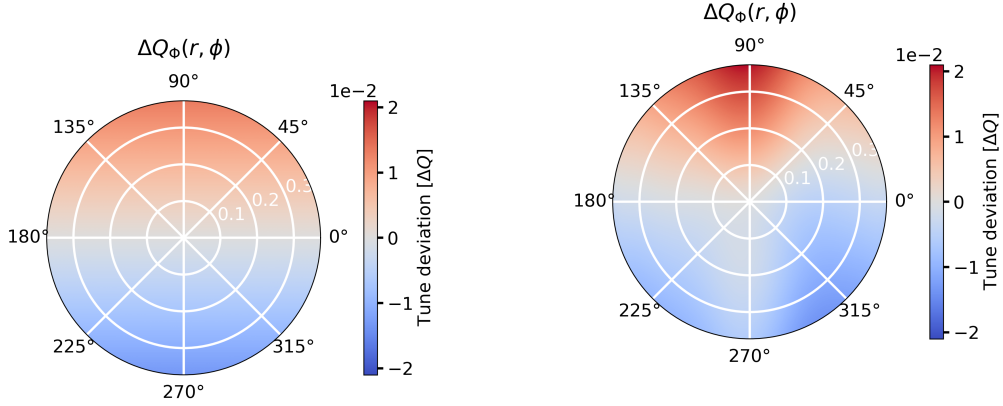


Figure 2.12: The phase shift term, $\Delta Q_{\Phi,Q'}(r, \phi)$, from first order chromaticity, $Q' = 10$, plotted in longitudinal polar coordinates (r, ϕ) .

Figure 2.13: The sum of the phase shift term from chromaticity 10, $\Delta Q_{\Phi,Q'}(r, \phi)$, and the phase shift term from e-cloud in an LHC quadrupole, $\Delta Q_{\Phi}(r, \phi)$, plotted in longitudinal polar coordinates (r, ϕ) .

The resulting phase shift term from e-cloud plus a linear chromaticity of 10 is plotted in Fig. 2.13. There is a peak at high radius r for $\phi = 90^\circ$ of $2e-2$, which is close to twice as high as the peak at the same degree in Fig. 2.12. The tune shift is positive for $40^\circ < \phi < 140^\circ$, and negative for $140^\circ < \phi < 270^\circ$ and $270^\circ < \phi < 40^\circ$ and at $\phi = 270^\circ$ there is a region with a tune deviation of $\Delta Q = 0$.

The phase shift term from negative chromaticity can be seen in Fig. 2.14. This plot is the equivalent of multiplying the tune shift in Fig. 2.12 with -1 . The sum of the phase shift from -10 chromaticity and the phase shift from e-cloud plotted in Fig. 2.11b, is plotted in Fig. 2.15. The tune shift is positive for angles $190^\circ < \phi < 320^\circ$ with a peak following the $\phi = 270^\circ$ line, with the highest point reaching a tune deviation of $\Delta Q = 2e-2$ located at the maximum radius. The rest of the circle has a negative tune shift apart from a peak following the $\phi = 90^\circ$ line at amplitude 0. In summary, this tune shift plot in the longitudinal phase space appears to be the tune shift plot in Fig. 2.13 mirrored in the $\phi = 180^\circ$, or 0 line.

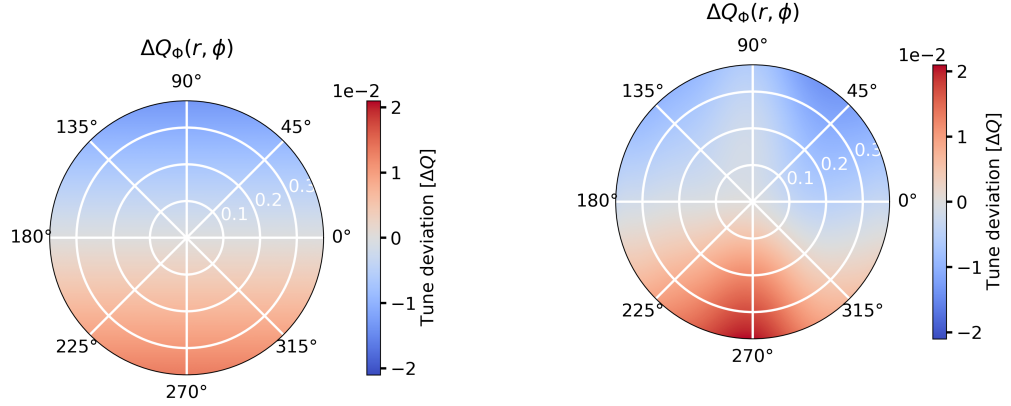


Figure 2.14: The phase shift term, $\Delta Q_{\Phi,Q'}(r, \phi)$, from first order chromaticity, $Q' = -10$, plotted in longitudinal polar coordinates (r, ϕ) .

Figure 2.15: The sum of the phase shift term from chromaticity -10 , $\Delta Q_{\Phi,Q'}(r, \phi)$, and the phase shift term from e-cloud in an LHC quadrupole, $\Delta Q_{\Phi}(r, \phi)$, plotted in longitudinal polar coordinates (r, ϕ) .

2.3.2 Simulations with individual detuning terms

Four categories of simulations were run to investigate the impact of each term of the detuning along the bunch from e-cloud: simulations with no detuning, $\Delta Q_R(r) = 0$ & $\Delta Q_{\Phi}(r, \phi) = 0$, simulations with only the phase shift term $\Delta Q_{\Phi}(r, \phi) \neq 0$ & $\Delta Q_R(r) = 0$, simulations with only the detuning with longitudinal amplitude, $\Delta Q_{\Phi}(r, \phi) = 0$ & $\Delta Q_R(r) \neq 0$ and simulation with full detuning from e-cloud, $\Delta Q_R(r) \neq 0$ & $\Delta Q_{\Phi}(r, \phi) \neq 0$. Note that a detuning in the form of a phase shift term from chromaticity, $\Delta Q_{\Phi,Q'}(r, \phi)$, is included in all simulations.

The resulting tune shifts as a function of chromaticity from the Vlasov approach and the macroparticle simulations are plotted for all four categories for e-cloud strength 1.0 and 1.8 in Fig. 2.16. The tune shift of the Vlasov modes is plotted in yellow-orange, with the color corresponding to the instability growth rate of that mode. The spectrum of the macroparticle simulations at each chromaticity is calculated using the SUSSIX algorithm and is plotted as black dots. The size of the dot corresponds to the amplitude of the frequency peak and the highest peak is marked by a big dot at each chromaticity.

The tune shift, $(Q - Q_0)/Q_s$, for simulations with only dipolar forces, meaning $\Delta Q_R(r) = 0$ & $\Delta Q_{\Phi}(r, \phi) = 0$, is plotted as function of chromaticity in Fig. 2.16a for e-cloud strength 1.0 and in Fig. 2.16b for e-cloud strength 1.8. The Vlasov modes are grouped on the integer lines of $(Q - Q_0)/Q_s$ for positive chromaticity. The modes in the interval $-3 < (Q - Q_0)/Q_s < 0$ are slightly stronger compared to the modes outside of that interval. The Vlasov modes on these lines are weakly unstable. For negative chromaticity, unstable Vlasov modes can be seen at $(Q - Q_0)/Q_s = 0.5, 0, -0.5, -1.5, -2, -2.75$ and 3.1. No clear tune shift dependence on chromaticity is seen. The spectra from the macroparticle simulations agree with the tune shift of the Vlasov modes.

Chapter 2. Vlasov approach for modeling e-cloud instabilities

The resulting spectrogram of simulations with higher e-cloud strength, 1.8, can be seen in Fig. 2.16b. At high chromaticity, $Q' > 10$, both the Vlasov modes, orange, and the frequency peaks from the macroparticle simulations, black, follow the integer lines of $(Q - Q_0)/Q_s$. At lower chromaticity, several strong modes are visible in the Vlasov spectrum, the strongest three have a tune shift of $(Q - Q_0)/Q_s = 0, -2.2$ and -3.8 at chromaticity -10 and all shift down at the same rate until they reach the integer lines $(Q - Q_0)/Q_s = -1, -3$ and -5 respectively at chromaticity $= 10$. The spectral analysis of the macroparticle simulations does not display multiple modes, however, the highest peak follows one of the strong Vlasov modes for all chromaticities.

The spectrograms as a result of simulations including the phase shift term from e-cloud, $\Delta Q_\Phi(r, \phi) \neq 0$ & $\Delta Q_R(r) = 0$, can be seen in Fig. 2.16c and Fig. 2.16d for e-cloud strength 1.0 and 1.8 respectively. These spectrograms are similar to the spectrograms when no detuning from e-cloud is included, Fig. 2.16a and Fig. 2.16b. In Fig. 2.16c, both the Vlasov modes and the frequency peaks in the macroparticle spectra follow the integer lines of $(Q - Q_0)/Q_s$ for positive chromaticity. For negative chromaticity in the same figure and for all chromaticities in Fig. 2.16d, the highest peak in the macroparticle spectrum follows the strongest Vlasov mode.

In Fig. 2.16e, displaying results from simulations with detuning with longitudinal amplitude from e-cloud, the Vlasov modes are parallel to the integer lines of $(Q - Q_0)/Q_s$ for positive chromaticity. The strongest modes are separated by Q_s and weak Vlasov modes are visible in between. For negative chromaticity, the Vlasov modes have a slight negative slope. A similar picture is painted by the macroparticle spectrum, however, the weak Vlasov modes are not visible. The strongest modes are in the interval $-1 < (Q - Q_0)/Q_s < 3$, which is higher than the interval of the strong modes in Fig. 2.16a. The spectrogram from simulations with higher e-cloud strength, Fig. 2.16f, is similar; the Vlasov modes have a slight slope down for negative chromaticity and are parallel to the Q_s lines for positive chromaticity. The difference, compared to the spectrogram at lower e-cloud strength, is that the Vlasov modes are stronger, and no grouping around lines separated by Q_s is visible. The macroparticle frequency peaks follow the strongest modes for negative chromaticity and for positive chromaticity, the frequency peaks are concentrated in the region $-2 < (Q - Q_0)/Q_s < 4$, although no clear structure is visible. This could be the result of several modes of similar frequency and growth rate being present, as indicated by the Vlasov simulations.

Finally, Fig. 2.16g and Fig. 2.16h, are the resulting spectrograms of simulations with full detuning from e-cloud. Figure 2.16g is very similar, but not identical, to the spectrogram as a result of simulations with only detuning with longitudinal amplitude from e-cloud at e-cloud strength 1.0, Fig. 2.16e. The Vlasov modes and the frequency peaks between the strongest modes separated by Q_s are slightly weaker. In Fig. 2.16h, two very strong Vlasov modes are visible for negative chromaticity starting at $(Q - Q_0)/Q_s = 1$ and $(Q - Q_0)/Q_s = 0$, both with a negative slope. The maximum frequency peak of the macroparticle simulations follows the tune shift of the worst Vlasov mode. In the interval between 0 and 15 chromaticity, the lower of the two strongest Vlasov modes becomes more unstable compared to the top one and continues its

negative tune shift. The maximum peak in the macroparticle spectrum follows this mode. For chromaticities greater than 15, several unstable Vlasov modes of equal growth rates are visible, with the strongest modes being in the interval $-2 < (Q - Q_0)/Q_s < 2$ and are all parallel to the Q_s lines. Similarly, the macroparticle spectrum has several peaks in the same interval but no clear mode structure.

The different categories of simulations, with the four combinations of $\Delta Q_R(r)$ and $\Delta Q_\Phi(r, \phi)$ produce spectrograms different to each other. This indicated that the contribution from each detuning term is significant. When detuning with longitudinal amplitude, $\Delta Q_R(r)$, from e-cloud is included, weak Vlasov modes between the Q_s lines are present. The spectral analysis of the macroparticle simulations reveals the same tune shifts as predicted by the unstable Vlasov modes for all simulations at e-cloud strength 1.0. At e-cloud strength 1.8, only the peak frequency can be deduced from the macroparticle simulations due to the strong instability and this peak follows the tune shift of the worst Vlasov mode for all categories of simulations. The predicted tune shift from the Vlasov approach agrees with macroparticle simulations.

The resulting growth rates for the four categories of simulations are plotted in Fig. 2.17, for e-cloud strength 1.0 corresponding to the plots on the left-hand side, and for e-cloud strength 1.8 corresponding to the plots on the right-hand side.

The results of simulations with only dipolar forces from e-cloud, $\Delta Q_R(r) = 0$ & $\Delta Q_\Phi(r, \phi) = 0$, for e-cloud strength 1 can be seen in Fig. 2.17a. In the region between chromaticity -10 and 0 , several Vlasov modes with positive growth rates are visible and one is visibly the strongest. This mode starts at a growth rate of 140 s^{-1} at chromaticity -10 and then decreases to a growth rate of 30 s^{-1} at chromaticity 0 . Most of the Vlasov modes visible in this region start at a high growth rate and decrease towards zero as the chromaticity increases. For positive chromaticities, many unstable Vlasov modes are visible and all have increasing growth rates in the interval for low chromaticities and then decreasing growth rates for higher chromaticities. The peak in growth rate is at different chromaticities for all modes but most peaks are grouped around a peak at chromaticity 10 or a peak at chromaticity 20 . For positive chromaticity, there is no Vlasov mode much stronger than the others. The growth rate achieved by doing an exponential fit in the macroparticle tracking data follows reasonably well the strongest Vlasov mode for all chromaticities. For high e-cloud strengths, Fig. 2.17b, a very strong Vlasov mode, which is clearly the strongest mode, is visible for all chromaticities. It starts at a growth rate 600 s^{-1} at chromaticity -10 and then has a decreasing growth rate with increasing chromaticity, ending at a growth rate 100 s^{-1} for chromaticity 25 where it meets other Vlasov modes. Weaker Vlasov modes are also present, five of which have a positive growth rate at chromaticity 0 . The other unstable modes appear to have low positive growth rates for negative chromaticities, zero growth rates at chromaticity 0 , and then again low positive growth rates at positive chromaticity. Also at this e-cloud strength does the growth rate of the macroparticle simulations follow the worst growth rate of the worst Vlasov mode.

Figure 2.17c and Fig. 2.17d shows the resulting growth rates of simulations including the phase

Chapter 2. Vlasov approach for modeling e-cloud instabilities

shift term from e-cloud, $\Delta Q_\Phi(r, \phi)$, for e-cloud strengths 1 and 1.8 respectively. These two plots are similar to the cases with only dipolar forces. For e-cloud strength 1, the difference is the most unstable Vlasov mode for negative chromaticity has a higher growth rate compared to Fig. 2.17a, and therefore decreases faster as the chromaticity approach 0 where the growth rate of this mode is again 30 s^{-1} . Similarly, the worst Vlasov mode in Fig. 2.17d has a higher growth rate for all chromaticities than the worst Vlasov mode in Fig. 2.17b. The growth rate of the macroparticle simulations agrees well with the worst Vlasov mode for both e-cloud strength 1 and e-cloud strength 1.8.

In the simulations with only the detuning with longitudinal amplitude from e-cloud, $\Delta Q_R(r)$, many Vlasov modes with growth rates seemingly independent of chromaticity are visible for both e-cloud strength 1, Fig. 2.17e, and e-cloud strength 1.8, Fig. 2.17f. The growth rates of the flat modes are below 40 s^{-1} for e-cloud strength 1 and below 100 s^{-1} for e-cloud strength 1.8. There are four Vlasov modes with growth rates higher than 40 s^{-1} for negative chromaticities in Fig. 2.17e, which all have a decreasing growth rate with increasing chromaticity. The growth rate of the macroparticle simulations follows the behavior of the worst Vlasov mode until the growth rate of this mode reaches 30 s^{-1} , where the growth rate of the macroparticle simulations continues to decrease with increasing chromaticity, although at a slower rate for positive chromaticity. Similarly for e-cloud strength 1.8, Fig. 2.17f, the growth rate of the macroparticle simulations follows the worst Vlasov mode until the flat Vlasov modes are reached, which in this plot is at chromaticity 4, and continues to decrease with the same rate until the growth rate is close to zero.

When the both detuning terms from e-cloud are included, $\Delta Q_R(r) \neq 0$ & $\Delta Q_\Phi(r, \phi) \neq 0$, the plots are similar to when only detuning with longitudinal amplitude, $\Delta Q_R(r)$, is included. The difference is that the phase shift term appears to have a destabilizing effect because the growth rates of all Vlasov modes are higher. The growth rate at chromaticity -10 for e-cloud strength 1 is about 80 s^{-1} in Fig. 2.17e compared to 120 s^{-1} in Fig. 2.17g. The growth rates of the macroparticle simulations agree with the worst Vlasov modes until the flat Vlasov modes are reached, at which point the growth rate of the macroparticle simulations continues to decrease until zero is reached at chromaticity 20. The discrepancy starts around chromaticity 0 for e-cloud strength 1 and at chromaticity 10 for e-cloud strength 1.8.

In summary, the phase shift term appears to have a destabilizing effect on the simulations whereas the detuning with longitudinal amplitude has a stabilizing effect on the simulations. Flat Vlasov modes are visible for positive chromaticity for all four categories of simulations. The flat Vlasov modes have growth rates of maximum 40 s^{-1} for all simulations with e-cloud strength s^{-1} and growth rate of maximum 100 s^{-1} in simulations with e-cloud strength 1.8. The growth rate of the macroparticle simulations follows the growth rate of the worst Vlasov mode, even if the mode is a flat mode when no detuning with longitudinal amplitude is present in the simulations. When this term is included, the macroparticle simulations agree with the worst Vlasov modes for negative chromaticity and for positive chromaticity until the worst Vlasov mode is one of the flat modes. For higher chromaticities, there is a stabilizing effect caused by

2.3 Study the detuning term

the detuning with longitudinal amplitude, which is not captured by the Vlasov approach.

Chapter 2. Vlasov approach for modeling e-cloud instabilities

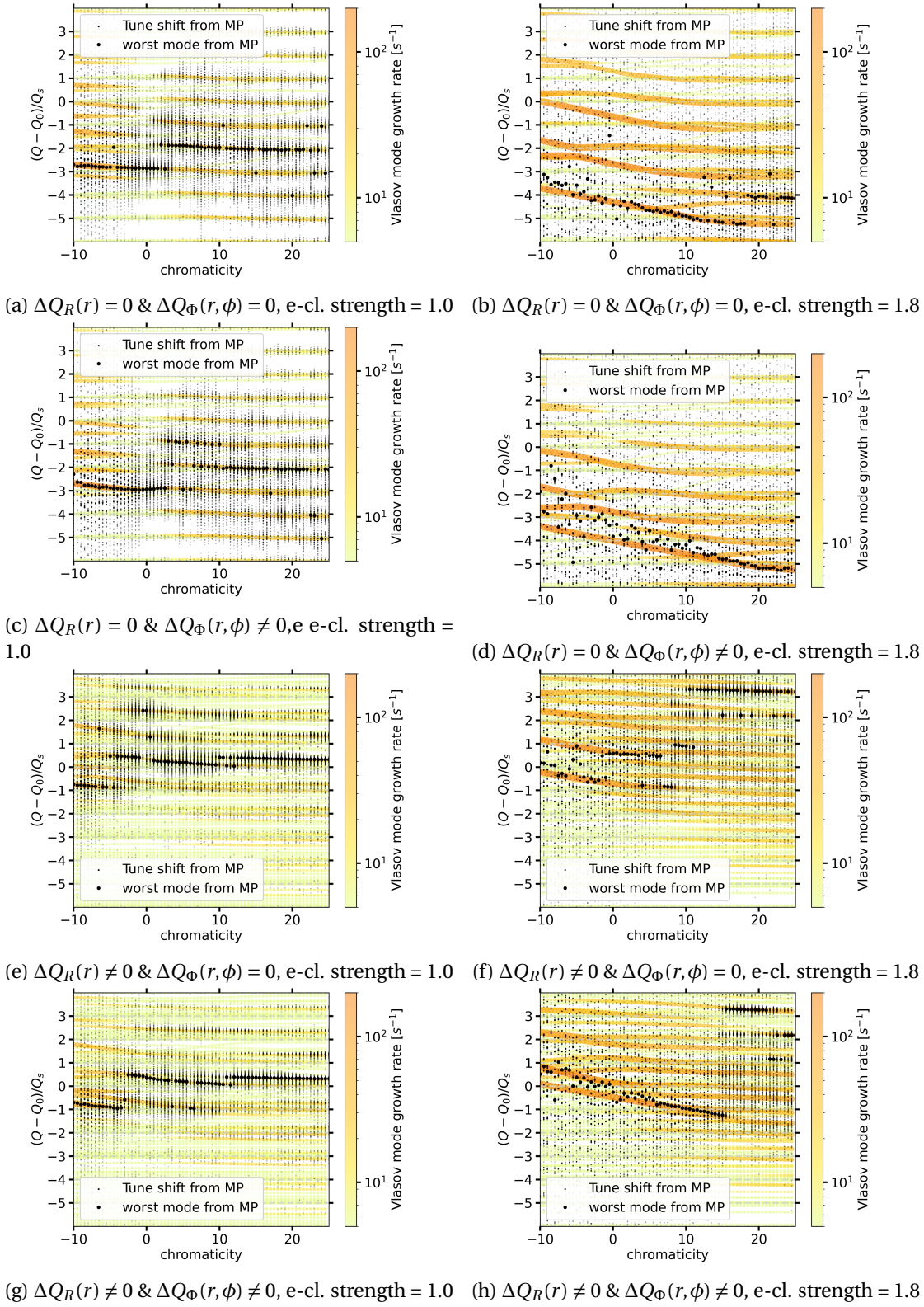


Figure 2.16: Tune shift as a function of chromaticity of the Vlasov modes, yellow-orange, and the spectral analysis of the macroparticle simulations, black. The peak frequency from the macroparticles is marked with a big dot at each chromaticity.

2.3 Study the detuning term

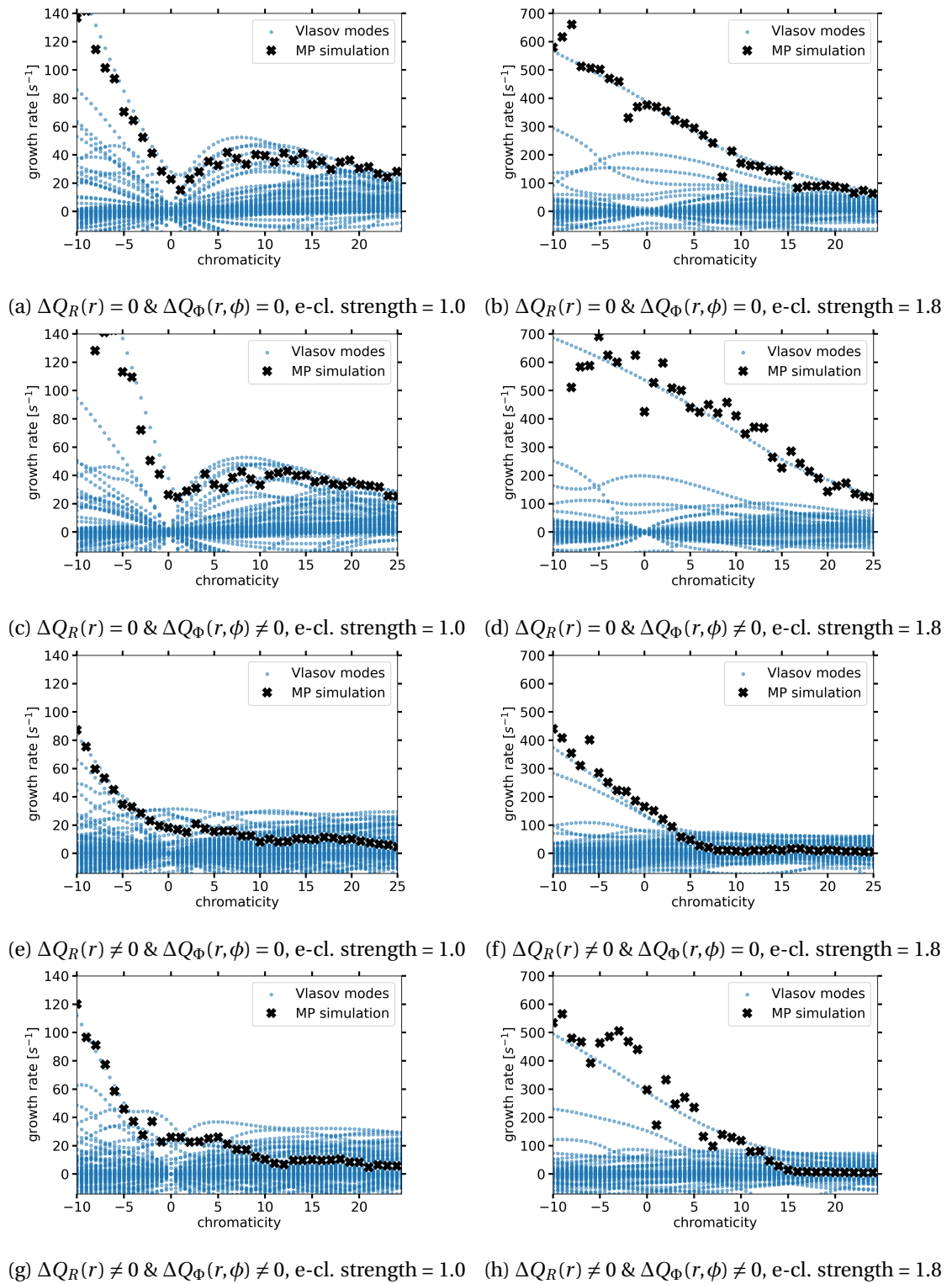


Figure 2.17: Instability growth rate as a function of chromaticity for Vlasov modes, blue, and the calculated growth rate from the macroparticle simulations, black.

2.4 Checks with impedance in the e-cloud Vlasov formalism

2.4.1 Impedance in the e-cloud formalism

When an electric charge passes through a metallic structure, such as a beam pipe or a magnet, an electromagnetic field is induced. This can be described using the concept of wake-fields. Consider two particles traversing through an accelerator element, for example, a cavity. The fields generated by the leading particle, the source particle, act on the trailing particle, the witness particle. These fields are called the wakefield. The Fourier transform of the generated wake fields is called the impedance. Just as the e-cloud, impedance is a collective effect that can drive instabilities in particle accelerators [73].

Impedance-driven instabilities have been studied more than e-cloud driven instabilities and more conventional simulation models exist that are still less computationally heavy than full PIC simulations. Impedance forces can also be expressed using the same formalism for the e-cloud forces introduced in the introduction, as will be done in this section in order to provide additional validation of the developed method. Simulations using this new force formalism can be compared to simulations using a conventional description of impedance forces, which will be done in the next section.

Impedance can be described using the same formalism used to describe the e-cloud forces by generating a set of responses and simulating the detuning along the bunch caused by quadrupolar impedance. This force model can then be put into both a macroparticle tracker and into a Vlasov solver. The impedance used for this example is a broad-band resonator with the parameters listed in Tab. 2.3.

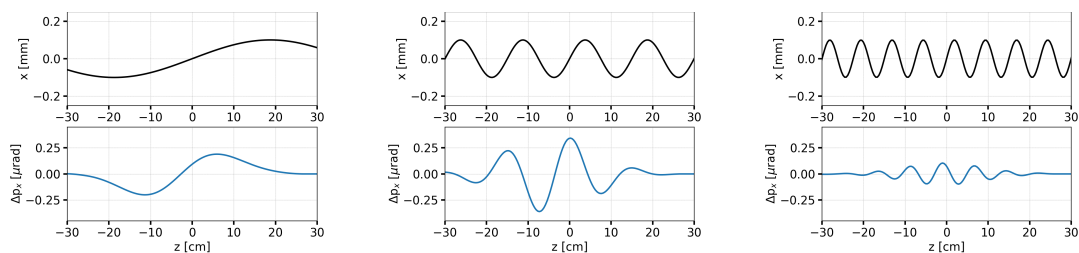
First, a set of response functions $k_n(z)$ are calculated by letting a bunch with bunch distortion $h_n(z)$ and a bunch intensity of $1.2e11$ protons per bunch pass through a broadband resonator and calculating the resulting response $k_n(z)$. Three examples of the test function $h_n(z)$, with one, five, and 20 oscillations along the bunch respectively, and the corresponding response functions $k_n(z)$ are plotted in Fig. 2.18.

The maximum amplitude of each response function, $k_n(z)$, as a function of a number of oscillations along the bunch, can be seen in Fig. 2.19. The amplitude of the responses to cosine bunch distortions, blue, decreases with an increasing number of oscillations whereas the amplitude of the responses to sinusoid bunch distortions, orange, first increases with

Table 2.3: The parameters used in the simulations with impedance-driven instabilities.

Variable	Value
bunch intensity	1.2e11 ppb
Shunt impedance	75e6
Resonator freq.	2e9 Hz
Resonator Q	1

2.4 Checks with impedance in the e-cloud Vlasov formalism



(a) The response to a sinusoid with one oscillation along the bunch. (b) The response to a sinusoid with 5 oscillations along the bunch. (c) The response to a sinusoid with 10 oscillations along the bunch.

Figure 2.18: Calculated responses $k_n(z)$, blue, from to bunch distortions $h_n(z)$, black, from passage through a broad band resonator.

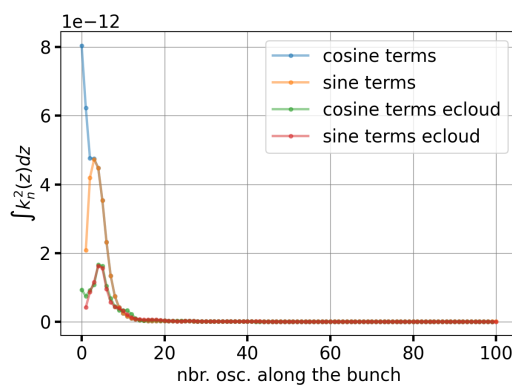


Figure 2.19: The amplitude of the responses for each number of oscillations along the bunch from impedance and e-cloud.

the number of oscillations along the bunch until it reaches the blue curve after which it also decreases with the number of oscillations along the bunch. The amplitude of the responses from the e-cloud is also plotted in the same figure, in green and red, and is lower than the amplitude of the impedance responses for the chosen impedance and e-cloud parameters. The simulations are therefore done for low impedance strengths to have similar amplitude of responses. The amplitude of e-cloud responses first increases with the number of oscillations along the bunch, until the number of oscillations along the bunch is 4, and then decreases as the number of oscillations along the bunch increases. Just like the amplitude of the responses from impedance, the cosine terms have a higher amplitude than the sine terms for the first two points plotted, but then the difference is smaller between the amplitude of the cosine terms and sine terms from the impedance.

The detuning along the bunch caused by the broad-band resonator, described by Tab. 2.3, is plotted in Fig. 2.20 in blue. The tune deviation is largest at the center of the bunch with an amplitude of $\Delta Q = 4e - 3$ and goes towards zero for both the head and the tail of the bunch. This detuning is again modeled by fitting a polynomial of degree 10 to the curve, plotted in

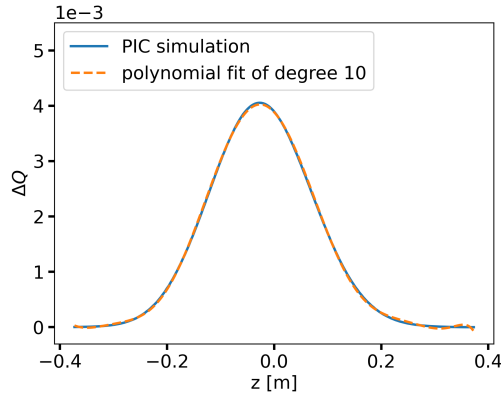


Figure 2.20: The detuning along the bunch is caused by a broadband impedance with a polynomial fit of degree 10.

orange in Fig. 2.20.

The impedance of a broadband resonator is now described with the same formalism used for the e-cloud.

2.4.2 Comparison with conventional impedance modeling

macroparticle simulations with impedance forces described by the e-cloud formalism are benchmarked against conventional macroparticle simulations performed with the PyHEADTAIL code.[74].

The impedance strength was varied by multiplying dipolar and quadrupolar forces with a factor. The resulting instability growth rates from PyHEADTAIL simulations, as a function of impedance strengths, are plotted in Fig. 2.21 as whole lines where the color of the line corresponds to the chromaticity used in the simulations. The growth rates of simulations with chromaticity -10 , plotted in dark blue, are higher than the growth rates of simulations with higher values of chromaticity for all impedance strengths. For impedance strengths < 0.2 , the growth rate increases from 0 to 50 s^{-1} and then stays at this value for impedance strengths 0.2-0.3. At impedance strength 0.3, the instability growth rate grows rapidly with increasing impedance strength, from 50 s^{-1} to 400 s^{-1} at impedance strength 0.6. The behavior is similar for simulations with chromaticity -5 , plotted as light blue, with growth rates slightly lower for all impedance strengths. In the curves for chromaticity 0, 5, 10, and 15 the growth rate is close to zero until impedance strength 0.3, 0.46, 0.52, and 0.58 respectively. At this threshold impedance strength, the growth rates increase with chromaticity at the same rate as the growth rate for chromaticity -10 in the same region. The instability growth rate for simulations with chromaticity 20, slowly increases but stays below 20 s^{-1} for all impedance strengths.

In the same figure, the instability growth rates from macroparticle simulations using the e-cloud formalism for the impedance forces are plotted as crosses. The color again corresponds

2.4 Checks with impedance in the e-cloud Vlasov formalism

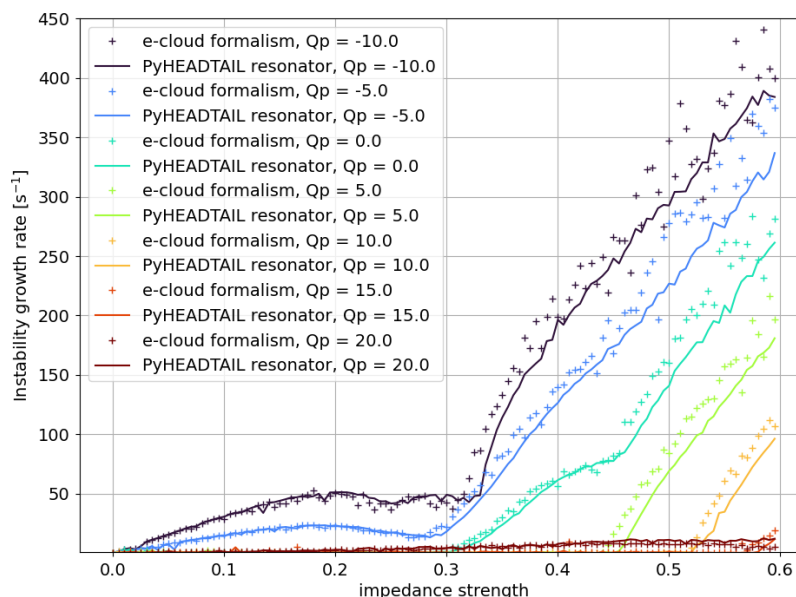


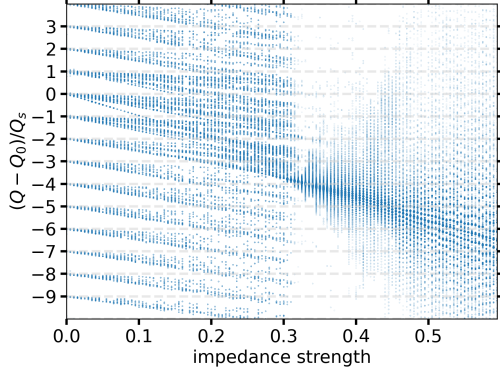
Figure 2.21: The instability growth rate calculated from macroparticle simulations using the e-cloud formalism to express impedance, plotted as crosses, and conventional macroparticle simulations using PyHEADTAIL, plotted as whole lines. The growth rate is plotted as a function of impedance strength for seven different values of chromaticity.

to the chromaticity. It is evident that the growth rates from these simulations match the growth rates obtained from PyHEADTAIL simulations.

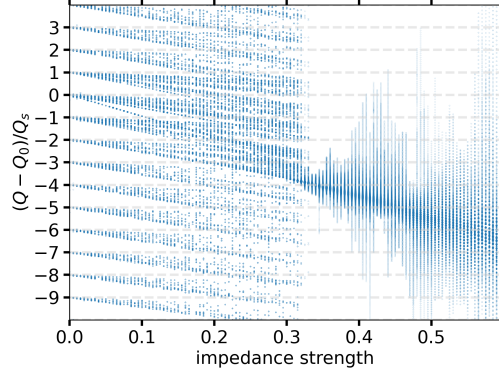
The resulting spectra from macroparticle simulations using the e-cloud formalism of impedance forces for zero chromaticity can be seen in Fig. 2.22a. For impedance strengths 0-0.3, several frequency peaks are visible and are grouped on the Q_s lines. As the impedance strength increases the peaks spread down from each integer line in a fanlike pattern. For impedance strengths higher than 0.3, one major frequency peak is visible which shifts down in tune as the impedance strength increases. The resulting spectrogram for simulations using the conventional simulations see Fig. 2.22b, are very similar. In conclusion, both force modes of impedance produce the same spectrograms for zero chromaticity.

When chromaticity is set to 20, the simulations using the e-cloud formalism of forces produce the spectrogram displayed in Fig. 2.22c. In the region with impedance strengths < 0.2 , the frequency peaks are grouped in fans originating from the integer lines at impedance strength 0. At higher impedance strengths the frequency peaks following the lower line of the fans moving to more negative $(Q - Q_s)/Q_0$ values are visible. As the impedance strength increases more, fewer and fewer peaks are visible. The lines visible at impedance strengths > 0.5 are the lines originating from $(Q - Q_s)/Q_0 = 1, -1, -2,$ and -3 , with the two center lines being slightly more pronounced. The spectrogram from conventional PyHEADTAIL simulations, Fig. 2.22d, is again very similar to the spectrogram from simulations with impedance in the

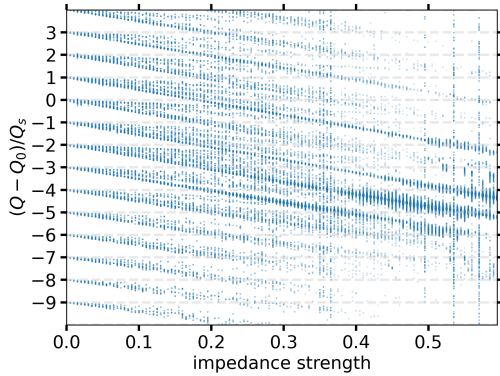
e-cloud formalism.



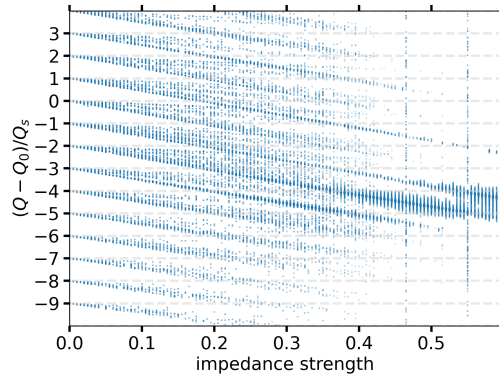
(a) The frequency spectra of macroparticles simulations using the e-cloud formalism of impedance for chromaticity 0.



(b) The frequency spectra of macroparticles simulations using PyHEADTAIL for chromaticity 0.



(c) The frequency spectra of macroparticles simulations using the e-cloud formalism of impedance for chromaticity 20.



(d) The frequency spectra of macroparticles simulations using PyHEADTAIL for chromaticity 20.

Figure 2.22: The frequency spectra at each impedance strength evaluated using the SUSSIX algorithm for macroparticle simulations using the e-cloud formalism of forces, left, and conventional PyHEADTAIL simulations, right. The size of the dot corresponds to the amplitude of that frequency peak.

2.4.3 Results with impedance forces in the e-cloud Vlasov formalism

The impedance forces in the e-cloud formalism are then put into the Vlasov approach and the results are compared to the tune shift from macroparticles using the same force formalism. The resulting tune shifts of the Vlasov modes as well as from the macroparticle simulations are plotted in Fig. 2.23a for chromaticity 10 with no detuning from impedance. The color of the Vlasov modes corresponds to the instability growth rate of each mode, with the most unstable modes being plotted in orange. There are Vlasov modes with tune shifts following the integer lines of $(Q - Q_s)/Q_0$ for all e-cloud strength and for impedance strengths > 0.4 , there is also a strong Vlasov mode going from $(Q - Q_s)/Q_0 = -3$ to $(Q - Q_s)/Q_0 = -4$ at impedance strength

2.4 Checks with impedance in the e-cloud Vlasov formalism

0.6. The frequency peaks of the macroparticle simulations follow the Vlasov modes very well. For impedance strength > 0.4 , only the strong Vlasov mode can be seen in the macroparticle spectra.

In Fig. 2.23c, the detuning from impedance is included in both simulation approaches. The Vlasov modes are fanned down from the integer lines of $(Q - Q_s)/Q_0$ and a strong mode is visible going from $(Q - Q_s)/Q_0 = -6$ to -7 for impedance strengths > 0.5 . The frequency peaks of the macroparticle simulations follow the Vlasov modes very well also in this case.

The instability growth rate of the Vlasov modes for simulations with chromaticity 10 without detuning from impedance can be seen in Fig. 2.23b. The instability growth rates of the corresponding macroparticle simulations are also plotted in this figure. Several unstable Vlasov modes are visible with growth rates below 40 s^{-1} . Two Vlasov modes have higher growth rates, and the growth rate of the macroparticle simulations follows the worst Vlasov modes for all impedance strengths.

The instability growth rates resulting from simulations with detuning from impedance as well as a chromaticity of 10 can be seen in Fig. 2.23d. Several unstable Vlasov modes with growth rates increasing with impedance strength can be seen in this plot. The growth rate of the worst Vlasov mode is 125 s^{-1} at impedance strength 0.6. The macroparticle simulations have no instabilities until impedance strength 0.5, after which the instability growth rate grows rapidly until the instability rate of the worst Vlasov mode is reached at impedance strength 0.6.

Interestingly, as in the case of the e-cloud, in the presence of quadrupolar forces and chromaticity, we find unstable Vlasov modes that are not visible in the macroparticle simulation modes.

Also in this case, we can decompose the detuning term i decomposed into a phase shift $\Delta Q_\Phi(r, \phi)$ and a detuning with longitudinal amplitude, $\Delta Q_R(r)$, to introduce into the simulations separately.

The resulting growth rates from simulations with impedance strength 0.5, plotted as a function of chromaticity, can be seen in Fig. 2.24a. Here no detuning from impedance is included in the simulations. The growth rates of the Vlasov modes are plotted in blue and the growth rates of the macroparticle simulations are plotted as black crosses. Weak Vlasov modes of growth rates below 50 s^{-1} are visible for all chromaticities. A strong Vlasov mode of growth rate 320 s^{-1} at chromaticity -10 decreasing to a growth rate of 50 s^{-1} at chromaticity 12 is seen. The growth rate of the macroparticle simulations follows the worst Vlasov mode for all chromaticities.

When a phase shift term from impedance is introduced, $\Delta Q_R(r) = 0$ & $\Delta Q_\Phi(r, \phi) \neq 0$, the growth rates in Fig. 2.24b are obtained. Unstable Vlasov modes with growth rates fanning out from both sides of chromaticity 0 can be seen in this plot. The growth rates are higher for negative chromaticity. The macroparticle simulations again follow the growth rate of the most unstable Vlasov mode.

Chapter 2. Vlasov approach for modeling e-cloud instabilities

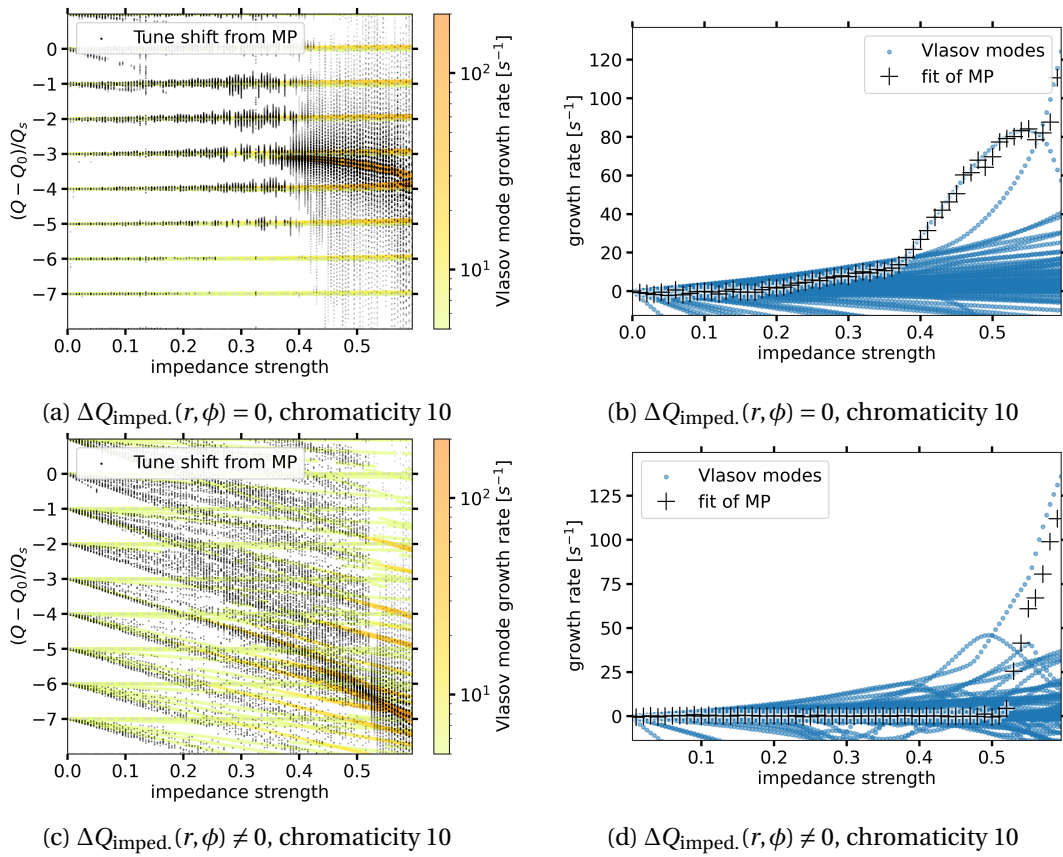


Figure 2.23: The simulation results with and without detuning from impedance for chromaticity 10.

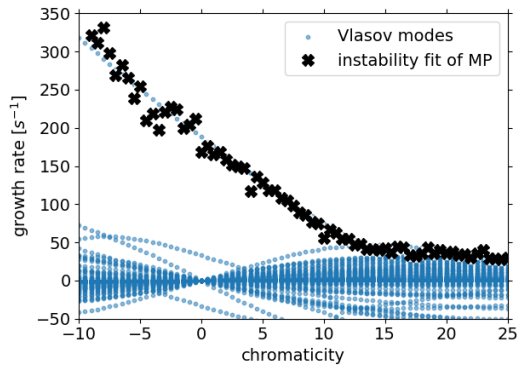
2.4 Checks with impedance in the e-cloud Vlasov formalism

In Fig. 2.24c, the growth rates from simulations including only the detuning with longitudinal amplitude, $\Delta Q_R(r) = 0$ & $\Delta Q_\Phi(r, \phi) \neq 0$, are plotted. The growth rates of the Vlasov modes are similar to the growth rate of the Vlasov modes in Fig. 2.24a. The growth rate of the macroparticle simulation follows the worst Vlasov mode until the weaker Vlasov modes are reached around chromaticity 15, after which the growth rate of the macroparticle simulations continues to decrease with chromaticity until a growth rate of 0 is reached at chromaticity 20.

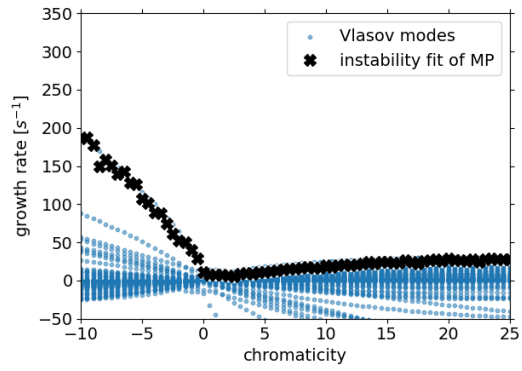
A similar image is obtained from simulations that incorporate both phase shifts and longitudinal amplitude detuning, as illustrated in Fig. 2.24d. The growth rate of the macroparticle simulations follow the worst Vlasov mode until chromaticity 5. Here weak Vlasov modes with growth rates independent of chromaticity are present. The growth rate of the macroparticle simulations reaches zero at chromaticity 10 and stays at zero for higher chromaticities, while in this region weak Vlasov modes are still visible.

In summary simulations performed with impedance forces in the presence of detuning forces and chromaticity, show strong similarities to the results found with the e-cloud.

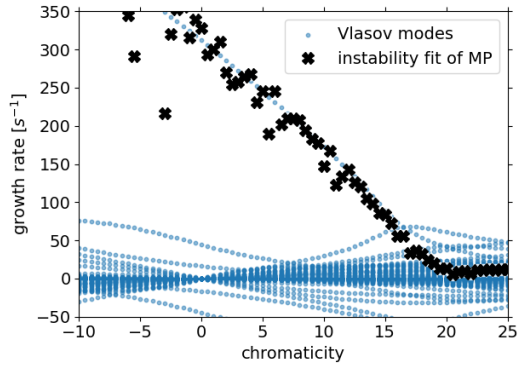
Chapter 2. Vlasov approach for modeling e-cloud instabilities



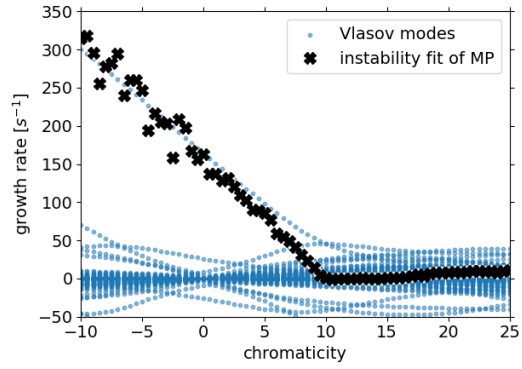
(a) $\Delta Q_R(r) = 0$ & $\Delta Q_\Phi(r, \phi) = 0$,
impedance strength = 0.5



(b) $\Delta Q_R(r) = 0$ & $\Delta Q_\Phi(r, \phi) \neq 0$,
impedance strength = 0.5



(c) $\Delta Q_R(r) \neq 0$ & $\Delta Q_\Phi(r, \phi) = 0$,
impedance strength = 0.5



(d) $\Delta Q_R(r) \neq 0$ & $\Delta Q_\Phi(r, \phi) \neq 0$,
impedance strength = 0.5

Figure 2.24: The resulting growth rates from the Vlasov approach, blue, and the instability growth rates from corresponding macroparticle simulations, black.

2.4 Checks with impedance in the e-cloud Vlasov formalism

To further demonstrate this discrepancy, growth rates from simulations including the full detuning from impedance are plotted as a function of impedance strength in Fig. 2.25 for six different values of chromaticity. The scale of the y-axis is the same of all six figures plotting growth rates -10 to 250 s^{-1} .

In Fig. 2.25a, no unstable Vlasov modes and no instabilities are visible in the macroparticle simulations until impedance strength 0.3, which will now be referred to as the stable region. For impedance strengths 0.3 to 0.4, the mid-region, an unstable Vlasov mode is visible and the growth rates of the macroparticles follow this mode perfectly. At impedance strength 0.45, the growth rate of the worst Vlasov mode increases faster with impedance strength compared to the behavior at lower impedance strengths, and the growth rates of the macroparticle simulations follow. This is a strong region.

As the chromaticity increases the growth rates at all impedance strengths decrease. The growth rate of the macroparticle simulations follow the worst Vlasov mode in the stable region and in the strong region for all values of chromaticity plotted. However, this is not the case in the mid-region.

When chromaticity is 1, see Fig. 2.25b, the growth rate of the worst Vlasov mode is slightly higher than the growth rate of the macroparticle simulations in the mid-region. The difference is bigger for chromaticity 2, see Fig. 2.25c.

For chromaticity 3 (Fig. 2.25d), the growth rates in the mid-region of the macroparticle simulations resemble the curve of the worst Vlasov mode but with lower values. At higher chromaticity, Fig. 2.25e and Fig. 2.25f, no curve is visible in the macroparticle simulations for in the mid-region whereas a Vlasov mode is still visible.

As chromaticity is increased gradually from 0 to 5, the instability growth rates of the Vlasov modes as well as the macroparticle simulations decrease. For impedance strengths 0.3-0.45, the growth rates of the macroparticle simulations decrease faster with chromaticity than the Vlasov modes suggesting the presence of a damping mechanism not captured by the Vlasov formalism.

Chapter 2. Vlasov approach for modeling e-cloud instabilities

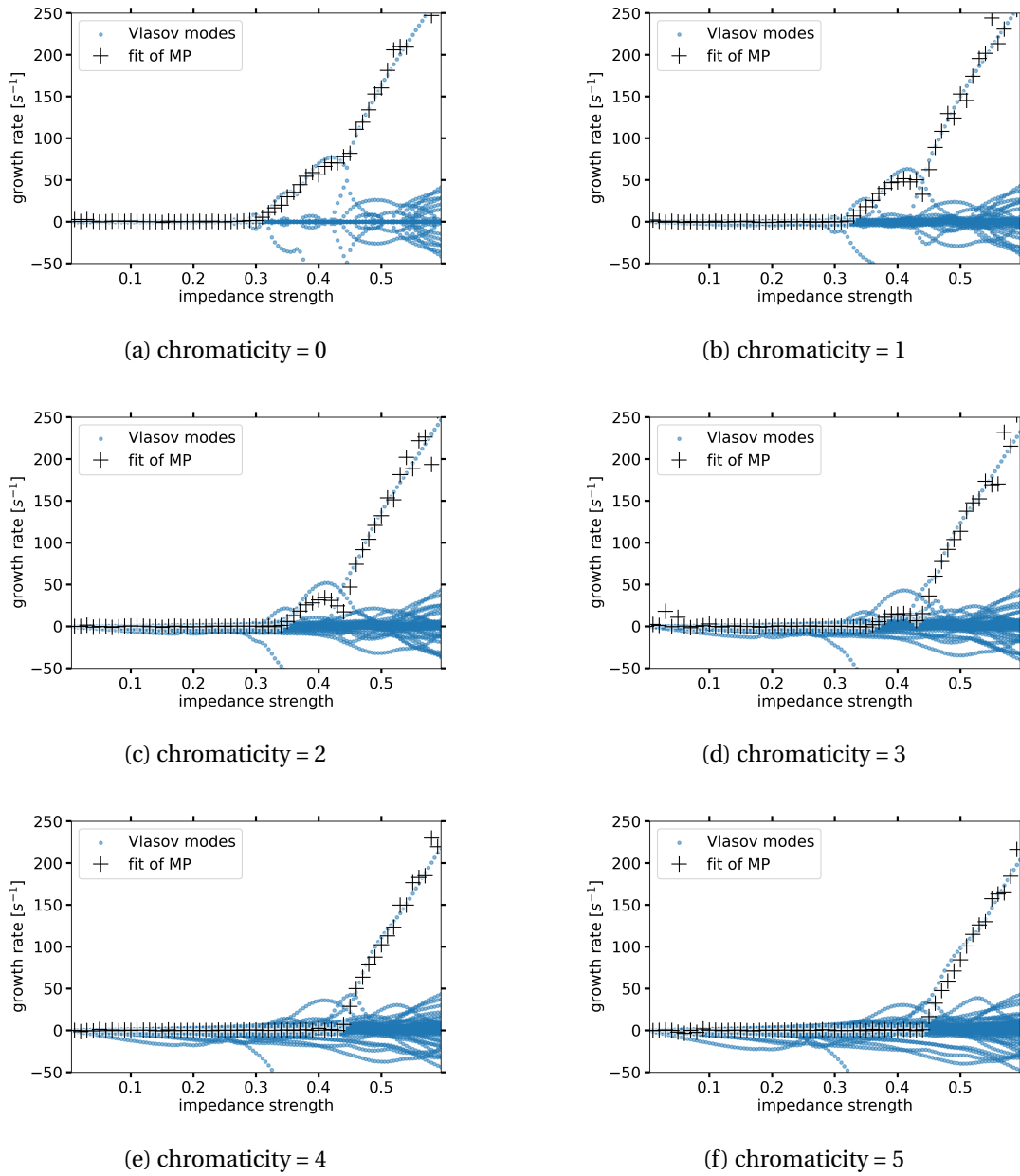


Figure 2.25: The growth rates obtained through the Vlasov approach, blue, and the growth rates from corresponding macroparticle simulations, black, plotted as a function of impedance strength for six different values of chromaticity.

3 Experimental characterization of e-cloud driven instabilities in the LHC

This chapter discusses several measurements were carried out to categorize the e-cloud driven instabilities in the LHC.

3.1 Measurements at high e-cloud conditions

As discussed in Sec. 1.2, the initial SEY estimates for each sector of the LHC in the beginning of run 3 were found to be high as a result of the air exposure of a large fraction of the beam elements in the long shutdown that preceded the run. The SEY values varied across machine sectors, but the estimated range for all sectors was between 1.8 and 2.2[75]

Measurements to characterize beam instabilities were carried out before the scrubbing run at the beginning of run 3, which meant that strong e-clouds were expected. Taking measurements at this stage offers a unique opportunity to study the characteristic of strong e-cloud driven instabilities.

3.1.1 Methodology

The conducted measurements focused on single-bunch instabilities in the vertical plane. Especially the dependence on linear chromaticity was investigated. Therefore a scan in vertical chromaticity was performed while the horizontal chromaticity was held constant. An overview of the machine parameters for the measurements can be seen in Tab. 3.1. Due to strong e-cloud using bunch trains longer than 24 bunches was not possible.

We constructed the filling schemes specifically for these measurements, which were tailored to avoid cross talk between the two beams due to beam-beam effects.

The measurement procedure was as follows:

1. The chromaticity and tune were measured and adjusted on the pilot bunches;

Table 3.1: Machine parameters during measurements.

Bunch Intensity	1.2e11 ppb
Beam energy	450 GeV (injection energy)
Horizontal Tune	62.27
Vertical Tune	60.29
Octupole current	0 A
Horizontal Chromaticity Q'_H	20
Bunch train in each beam	12b + 24 b
Bunch spacing	25 ns
Bunch length	1.15 ns
Transverse damper	on
Vertical chromaticity Q'_V	[5.0, 7.5., 10.0, 12.5, 15.0, 20.0., 25.0]

2. Next, a train of 24 bunches was injected and the transverse oscillations were measured turn by turn and bunch by bunch using the ADTobsbox [76, 77];
3. The head-tail monitors were used to measure the intra-bunch motion with an injection trigger, which captured the first 3000 turns of all 24 bunches;
4. The train was kept in the machine as long as possible, at injection energy, which for low chromaticity meant a few hundred turns, whereas for high chromaticity the beam could be kept for tens of thousands of turns;

This procedure was carried out for all points in chromaticity for both beam 1 and beam 2. To assess reproducibility, some measurements were repeated multiple times.

3.1.2 Overview of measured instabilities

The bunch-by-bunch and turn-by-turn data for beam 1 for the case where $Q'_V = Q'_H = 20$ is displayed in Fig. 3.1. The vertical position is plotted in the top plot and the horizontal position of the same bunches is plotted in the bottom plot. As expected, the vertical motion is much stronger than the horizontal motion, which suggests the presence of vertical instabilities. This is also observed in Beam 2 for the same chromaticity, as shown in Fig. 3.2. Horizontal instabilities are also observed in both beams but much later than the vertical instabilities, usually when the beam has already degraded.

The bunch by bunch behavior for a measurement in beam 1 with chromaticity 5 can be seen in Fig. 3.3a and for measurements with chromaticity 15 in Fig. 3.3b, where the vertical motion of each bunch is plotted. The vertical position of bunch 1 is plotted on the top plots and the bunch position of each consecutive bunch is plotted in order in the plots below. Figure 3.3a shows that vertical motion of the later bunches has a higher amplitude compared to the vertical motion of the earlier bunches. In other words, the observed instability is stronger towards the end of the train. In Fig. 3.3b, a similar trend is observed with the amplitudes of the

3.1 Measurements at high e-cloud conditions

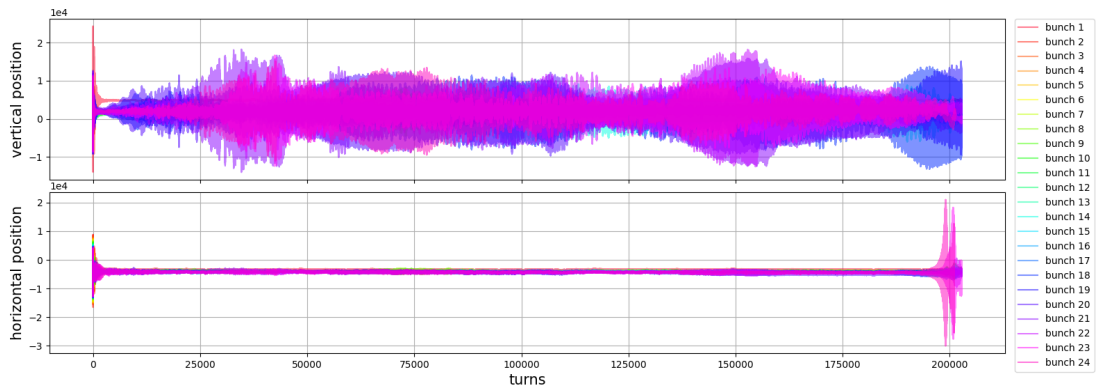


Figure 3.1: The plot shows the turn-by-turn data for all 24 bunches in beam 1 in both vertical (top) and horizontal (bottom) plane for the case $Q'_V = Q'H = 20$. The position of each bunch is plotted as a different color.

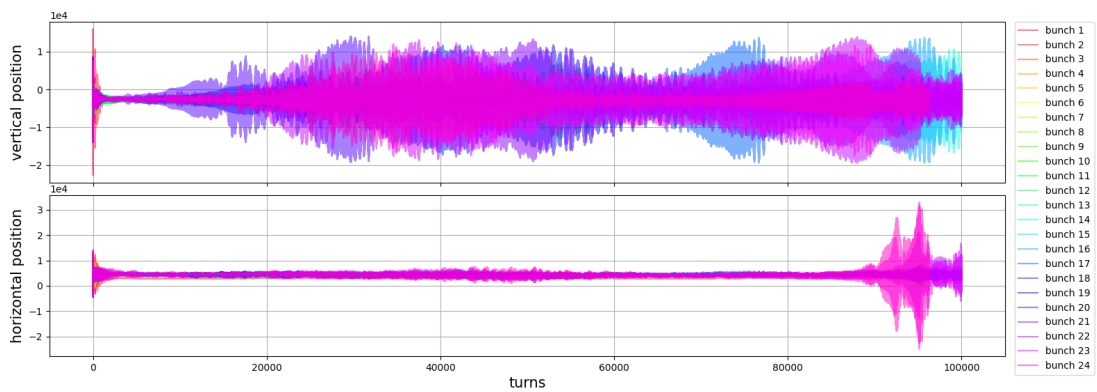


Figure 3.2: The plot shows the turn-by-turn data for all 24 bunches in beam 2 in both vertical (top) and horizontal (bottom) plane for the case $Q'_V = Q'H = 20$. The position of each bunch is plotted as a different color.

Chapter 3. Experimental characterization of e-cloud driven instabilities in the LHC

vertical motion is higher for the later bunches in the train compared to the earlier bunches. Notably, for high chromaticity, the middle bunches, bunch 10-13, appear to be more unstable than the following bunches. Nevertheless, the overarching trend remains that the observed instability is more pronounced among the last bunches in the train.

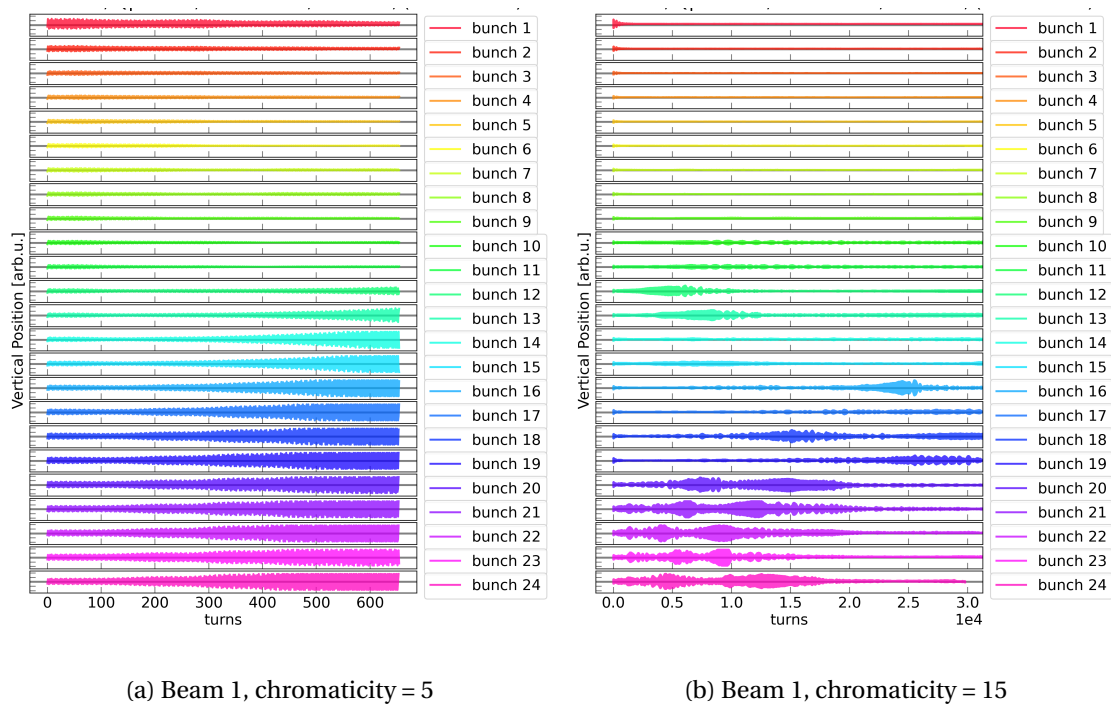


Figure 3.3: Vertical position measurements turn-by-turn for each bunch in the trains right after injection into the LHC. Transverse instabilities can be observed at the tail of each bunch train.

3.1.3 Instability Growth Rate

Growth Rate Calculation

The instability growth rate quantifies how fast an instability grows over time. As discussed in Sec. 2.1, it can be associated to the imaginary part of the eigenfrequency associated with the instability, also known as the complex mode frequency. The instability growth rate is the exponential rate at which the amplitude of the centroid motion grows. Figure 3.4 shows the centroid vertical position turn-by-turn for the first 1200 turns of one bunch. The signal oscillates at a frequency of 60.292 oscillations per turn and the oscillation amplitude grows until turn 1000, after which the oscillation amplitude decreases.

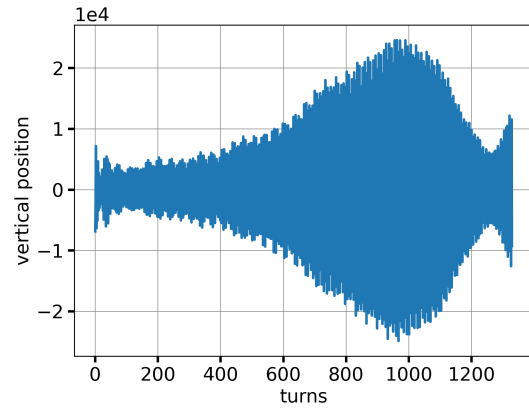


Figure 3.4: An example of the measured vertical position turn-by-turn for one bunch.

The procedure to calculate the instability growth rate from the measured data starts with choosing the first interval at which the centroid appears to have exponential growth. This is done to exclude injection oscillations and to exclude the effect of amplitude decrease due to losses or saturation of measuring equipment. The interval chosen for the data presented in Fig. 3.4 was turn 150-1000 and is plotted in orange in Fig. 3.5.

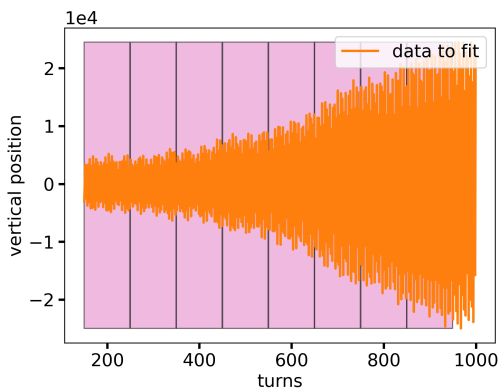


Figure 3.5: Example of windowing with no overlap using windows of width 100.

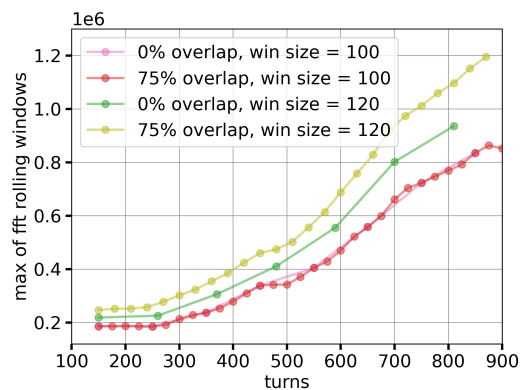
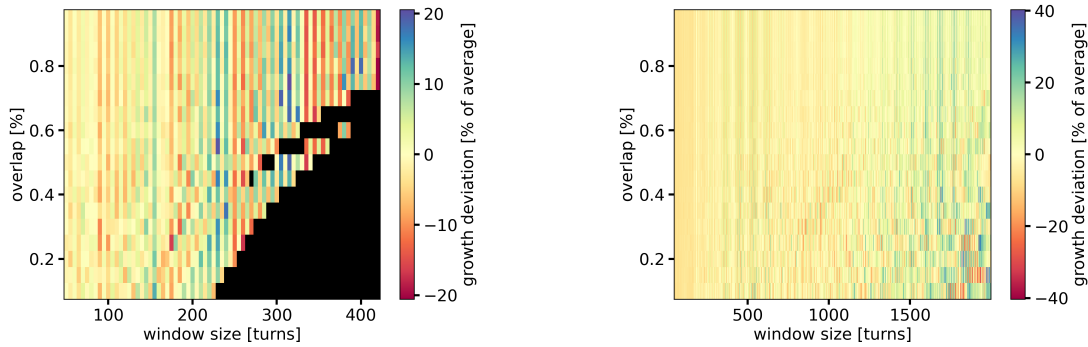


Figure 3.6: The tracked oscillation amplitudes from doing a rolling window FFT on the data in Fig. 3.4 using windows of width 100 or 120, and using 0% or 75% overlap. The results from using the windowing in 3.5 is plotted as pink.

Chapter 3. Experimental characterization of e-cloud driven instabilities in the LHC

The oscillations amplitude of measured data is then extracted by doing a sliding window FFT and plotting the maximum amplitude of the FFT for each window. An example of windowing using a window of 100 turns and no overlap can be seen in Fig. 3.5 and the corresponding amplitude of the FFT of each window is plotted as a pink line in Fig. 3.6.

If the window width is varied the resulting amplitude plot also varies slightly. The amplitudes obtained using a window width of 100 and 120 are represented by the pink and green colors, respectively, in Fig. 3.6. In addition, the overlap of consecutive windows was also varied and the resulting amplitudes are also plotted in Fig. 3.6. All plotted lines increase with the turn number, however, the rate of increase is not exactly the same. As a consequence, the estimated growth rate will depend to some extent on the parameters of the rolling window FFT.



(a) Calculations on a data set of length 850 turns with an average growth rate of $1/370$ turns⁻¹.

(b) Calculations on a data set of length 25 000 turns and an average growth rate of $1/10000$ turns⁻¹.

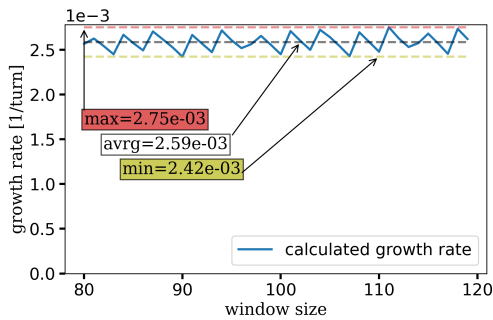
Figure 3.7: Variation of the calculated growth rate using the rolling window FFT technique for different window sizes and window overlap.

Figure 3.7a and 3.7b illustrate the extent to which the growth rate varies, expressed in percentage terms, for two different data sets of length 850 turns and 25000 turns respectively. A structure of vertical lines is visible in both plots, meaning the calculated growth rate does not vary much with respect to window overlap. There is an oscillating behavior with respect to window size, meaning the calculated growth rate displays an oscillating behavior with respect to window size that increases in amplitude as the window size increases. In addition, when the window size becomes comparable with the length of the data set and little overlap is used, no fit is possible. These cases are colored black in Fig. 3.7a. This situation is never reached in the data set of length 25 000, since the window size was limited to 2000. However, the calculated growth rate varies more for a longer window size.

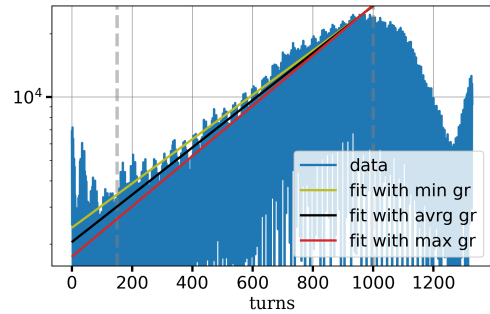
In order to counteract the oscillatory behavior of the growth rate calculation with respect to window size. A range of window-sizes of 80-120 was used, together with a 95% overlap, to calculate a set of growth rates for each bunch. An example of calculated growth rates as a function of windows size is plotted in blue in Fig. 3.8a, the corresponding measured data is plotted in log scale in Fig. 3.8b. The minimum, average and maximum growth rate is indicated

3.1 Measurements at high e-cloud conditions

as dashed lines and the corresponding fits are plotted in the same colors in the left graph. All three fits appear to agree quite well with the growth rate of the data and the average growth rate was then selected to be as best indicator. This technique, based on the averaged rolling window FFT fitting, is used to calculate the instability growth rate of the data collected during all measurements.



(a) The calculated growth rate using the rolling window FFT technique with an overlap of 95% as a function of window size is plotted as a blue curve. The minimum, average and maximum growth rate is marked with dashed lines of colors green, grey and red.



(b) The measured data of the vertical centroid position is plotted in log scale. Three exponentials with growth rates corresponding to the minimum, average and maximum growth rate calculated using the rolling window FFT technique for a range of window sizes 80-120 is plotted as green, black and red lines.

Figure 3.8: An example of the developed averaged rolling window FFT technique for finding the instability growth rate of turn-by-turn measured data for one unstable bunch.

Growth Rates of Measured Bunches

The growth rate calculated using the averaged rolling window FFT technique, described in the previous section, can be seen for all bunches in Fig. 3.9. The growth rate is plotted as a function of the bunch position for each injected bunch in the 24-bunch trains and the results from measurements in beam 1 are plotted in blue and measurements of of beam 2 are plotted in red. In Fig. 3.9a, Fig. 3.9b, Fig. 3.9c, and Fig. 3.9d, corresponding to growth rate from measurements with chromaticity 5, 7.5, 10 and 12.5 respectively, the bunches 10-24 have a non-zero growth rate indicating that these bunches are unstable. Earlier bunches are found to be stable. The instability was mainly seen in the later bunches of the train, which is typical for e-cloud-driven instabilities.

In measurements with chromaticity 15 and 20, see Fig. 3.9e and Fig. 3.9f, a trend of increasing growth rate with bunch position is observed. At these chromaticities, the growth rates are of the order of magnitude of 1 s^{-1} and the difference in growth rate between bunches is small.

Lastly, in measurements with high chromaticity, chromaticity 25, several bunches in the center of the train are unstable as well as the last 6 bunches of the trains. The growth rates of the center bunches are higher than the bunches at the end of the train, however the order it

Chapter 3. Experimental characterization of e-cloud driven instabilities in the LHC

magnitude if all growth rates are 1 s^{-1} for all bunches.

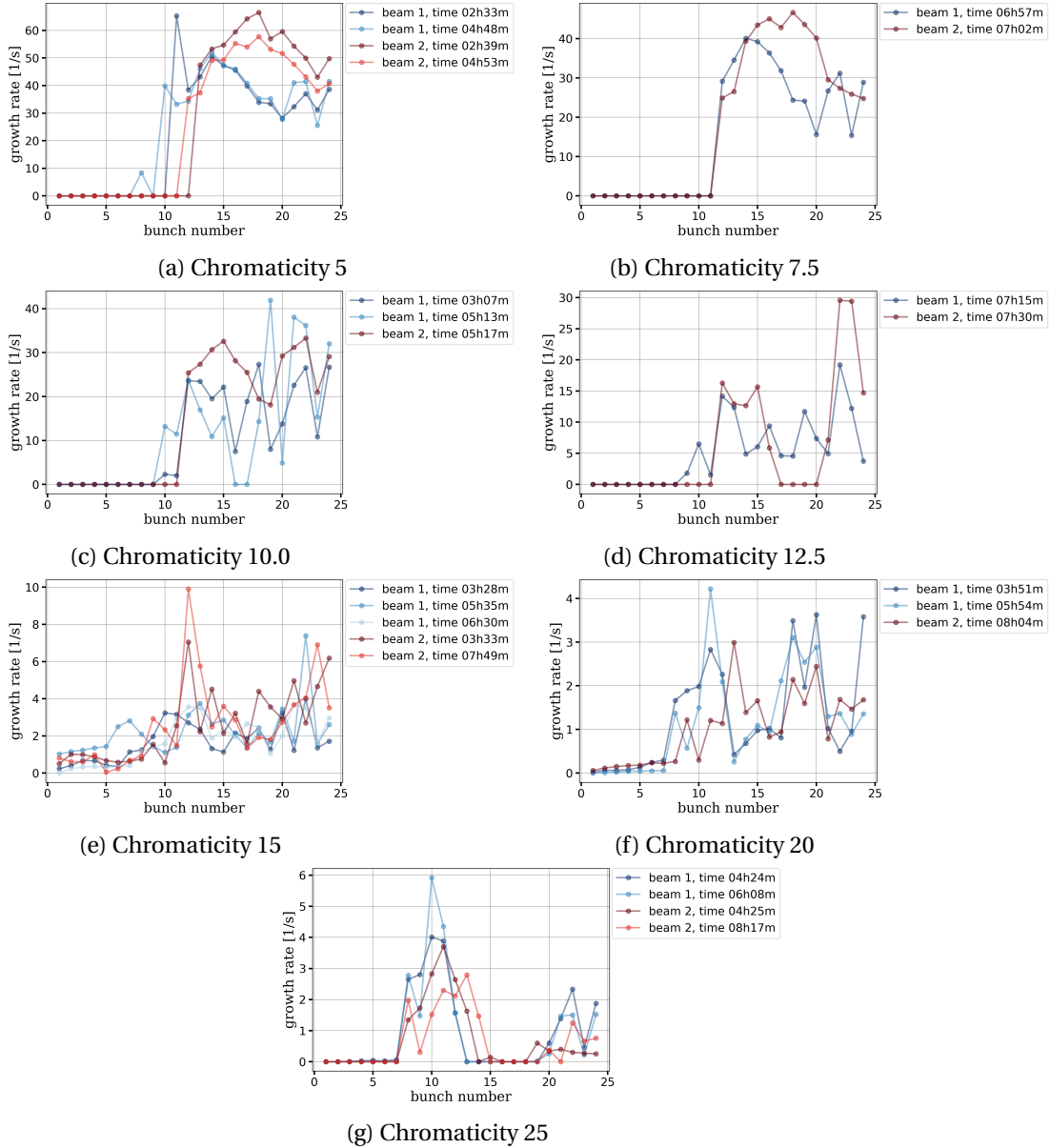


Figure 3.9: The calculated instability growth rate in the vertical plane for all injected trains. The results from beam 1 are plotted in blue and the results from beam 2 are plotted in red.

The calculated instability growth rates for all measurements and all bunches are plotted in Fig. 3.10. The points plotted are color-coded with respect to the bunch position, which means that all data points at one chromaticity for on specific bunch position have the same color.

In order to have a better overview of the growth rate dependence as a function of chromaticity, the average growth rate of the last 10 bunches is calculated and plotted in Fig. 3.11 with error bars representing one standard deviation. The growth rate of beam 1 starts at 35 s^{-1} and

3.1 Measurements at high e-cloud conditions

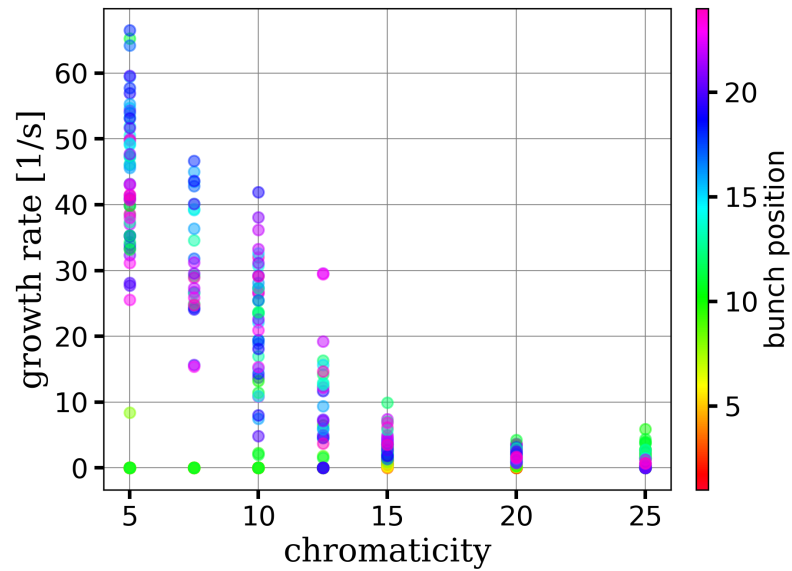


Figure 3.10: The growth rates for all bunches for all measurements. The points plotted are color-coded with respect to the bunch position, which means that all datapoints at one chromaticity for one specific bunch position have the same color.

the growth rate of beam 2 starts at 52 s^{-1} at chromaticity 5. The growth rate of both beams decreases with increasing chromaticity until chromaticity 15 at which the growth rates are less than 5 s^{-1} . For higher chromaticities, the calculated growth rates continue to decrease with increasing chromaticity but at a slower rate. The growth rates in beam 2 are slightly higher than the growth rates of beam 1 for chromaticities 5-15.

Chapter 3. Experimental characterization of e-cloud driven instabilities in the LHC

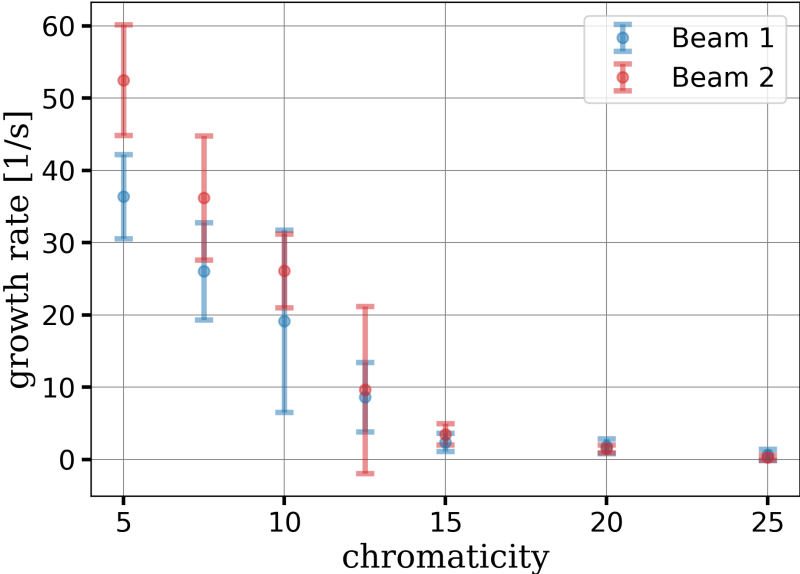


Figure 3.11: The average growth rate of the last 10 bunches as a function of chromaticity for beam 1 (blue) and beam 2 (red) with errorbars of one standard deviation.

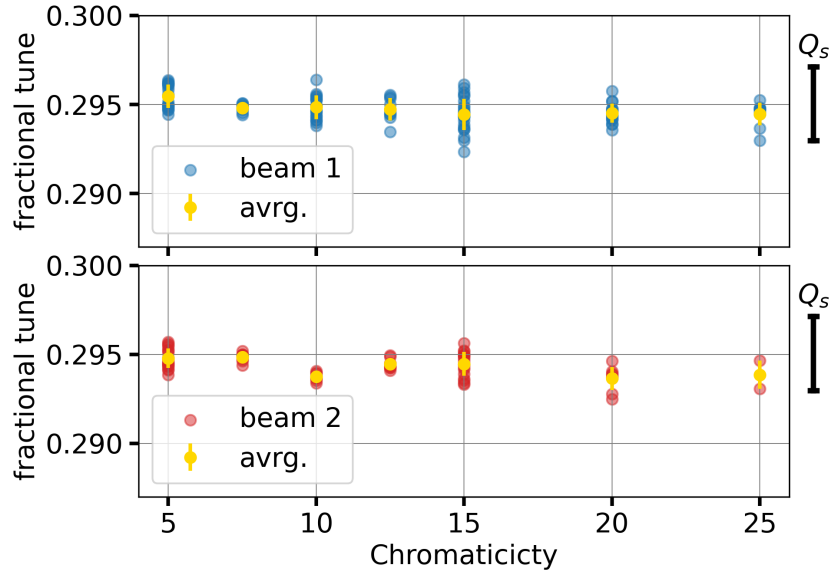


Figure 3.12: The fractional tune of the last 10 bunches in beam 1 is plotted as blue dots in the top plot and the fractional tune of the last 10 bunches in beam 2 is plotted as red in the bottom plot. The average fractional tune at each chromaticity in beam 1 and beam 2 is plotted in yellow with error bars of one standard deviation.

3.1.4 Spectral analysis of measured data

Bunch-by-Bunch Spectral analysis

Spectral analysis of the turn-by-turn and bunch-by-bunch measured data was done. The same turn intervals used for the growth rate instability fit were also used for the spectral analysis, meaning the turn interval that showed the first indication of exponential vertical amplitude growth. For stable bunches, the whole measured data set was used apart from the first 150 turns to avoid including the injection oscillations. The SUSSIX algorithm is used to analyze the spectral content of the instabilities and the NAFF algorithm, (described in [78]), is used to find the tune from the injection oscillations.

To visualize the general trend of the fractional tune of the unstable bunches, the tune of just the last 10 bunches is plotted in Fig. 3.12 for each chromaticity. The fractional tune from beam 1 is plotted in the top plot in blue and the average fractional tune at each chromaticity is plotted in yellow with error bars of one standard deviation. Similarly, the fractional tune of the last 10 bunches of beam 2 is plotted in red in the bottom plot of Fig. 3.12. The average is again plotted in yellow with error bars of one standard deviation. In addition, the synchrotron tune is marked as a scale bar on the right-hand side for reference. There is no strong dependence on chromaticity visible.

The spectral content of each bunch in the train of a measurement with chromaticity 5 of beam

Chapter 3. Experimental characterization of e-cloud driven instabilities in the LHC

1 can be seen in Fig. 3.13a. All frequencies found by the SUSSIX algorithm are plotted in a vertical line and the size of each dot is proportional to the amplitude of that frequency. Each vertical line corresponds to the spectral content from the measured data of one bunch. The tune found by the NAFF algorithm on the injection oscillation is plotted as a red dot for each bunch. The size of the synchrotron tune, Q_s , is plotted as a scale bar in the upper right corner. The tune is 0.292 for bunches 1-11. For bunches 12-19, the tune gradually increases from 0.292 to 0.295, and bunches 20-24 all have the tune 0.295. For these bunches (bunch 12-24) a strong peak is visible in the SUSSIX spectrum. No sidebands at a distance Q_s from the main mode are visible for any bunch.

Figure 3.13b displays the results of the spectral analysis of measurement in beam 2 for chromaticity 10. The tune of bunch 1-5 increases gradually from 0.291 to 0.2915. The tune changes from 0.2915 to 0.92 from bunch 5 to bunch 7 and then increases gradually to 0.2951 at bunch 20. The tune of the last 5 bunches is the same. A strong peak is visible in the SUSSIX spectrum for bunches 11-24. No obvious side bands are visible.

Similarly, the results from the spectral analysis of measurement of beam 2 at chromaticity 15 are displayed in Fig. 3.13c. The tune of the first 3 bunches is 0.291. The tune shifts up until it reaches 0.292 for bunch 5, and then shifts down to 0.289 for bunch 7 and up again to 0.291 at bunch 10. The tune calculated from the injection oscillation, red dots, stay between 0.29 and 0.291 for bunch 10-24. There is a peak visible in the SUSSIX spectrum, calculated from the turns where instability is visible, for bunches 12-14. This peak gradually increased from 0.291 to 0.292. This means that there is a difference between the tune measured at injection and the tune measured when instability is visible later in the fill. Side-bands of width Q_s are visible in the SUSSIX spectrum of bunch 11.

Finally, the spectral analysis of a measurement of beam 1 with chromaticity 20 can be seen in Fig. 3.13d. The tune of the first 5 bunches is approximately 0.292, then there is a jump to tune 0.291 for bunch 6-9, and another jump to tune 0.29 for bunch 10. The tune of bunches 10-24 increases gradually from 0.29 to 0.91. A peak is visible in the SUSSIX spectrum for bunches 14-24 and the position of the beam increases gradually from 0.29 to 0.292 at bunch 18 and stays at 0.292 for bunch 18-24. Side bands are visible for bunch 7,8,11 and 18.

The tune, calculated using the SUSSIX algorithm on the turn interval of the onset of the observed instabilities, for all measured bunch trains, can be seen in Fig. 3.14. If no instability was visible the tune was calculated on the full measured data. The resulting tunes with chromaticity 5 can be seen in Fig. 3.14a where the result from beam 1 is plotted in blue and the result from beam 2 is plotted in red. The fractional tunes of bunches 1-10 are all close to the nominal tune of 0.292. The fractional tune of subsequent bunches increases with increasing bunch number until bunch 18 where the following bunches all have fractional tunes close to 0.295. Similar behavior is seen in Fig. 3.14b, Fig. 3.14c, and Fig. 3.14d which displays the fractional tune of measurements with chromaticity 7.5, 10 and 12.5 respectively.

For high chromaticity, the spectral analysis showed signs of non-linear modulation, see

3.1 Measurements at high e-cloud conditions

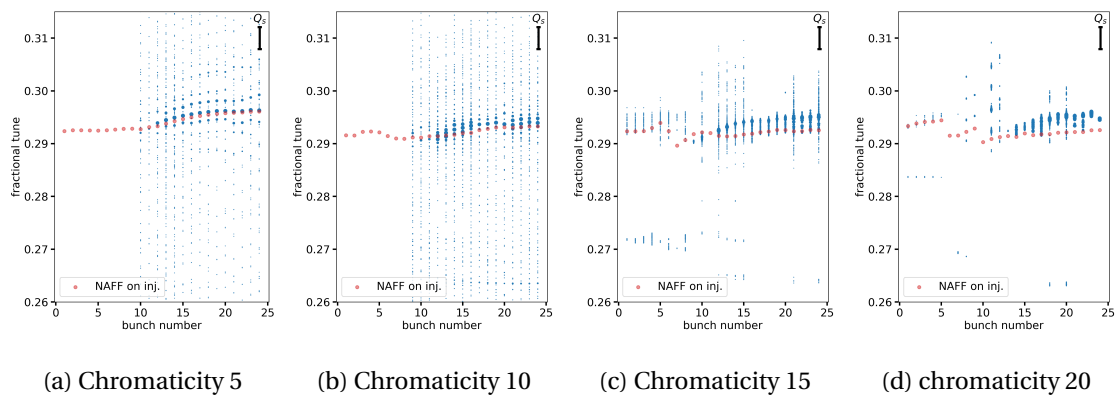


Figure 3.13: The spectral content of 4 different measurements calculated using the SUSSIX algorithm on the measured data of the turns and instability is visible, blue, compared to the tune of the injection oscillations calculated using the NAFF algorithm, red.

Fig. 3.14e, Fig. 3.14f and Fig. 3.14g displaying the fractional tune of measurements with chromaticity 15, 20 and, 25 respectively. Some of the bunches in the first half of the train have a fractional tune close to 0.27 which is the horizontal tune indicating a coupling between the two transverse planes.

Chapter 3. Experimental characterization of e-cloud driven instabilities in the LHC

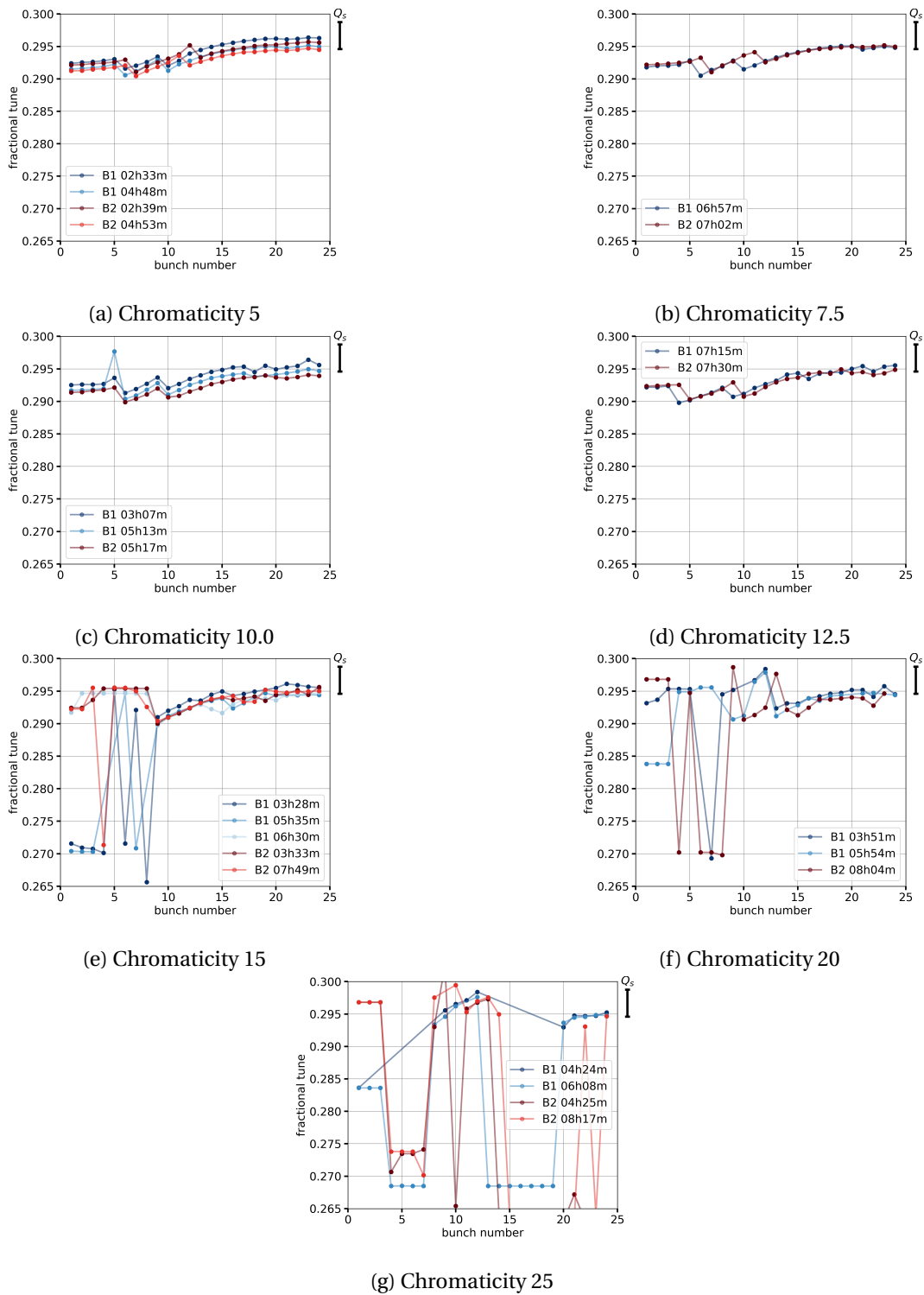


Figure 3.14: The calculated fractional tune in the vertical plane for all bunches in the injected trains. Measurements of beam 1 are plotted in blue and measurements of beam 2 are plotted in red. The synchrotron tune, Q_s is plotted for scale on the right side of each plot.

Turn-by-Turn spectral analysis

By conducting a rolling window FFT one can extract the spectral content of the beam as a function of time. The resulting spectra as a function of turns using a FFT window of 2000 turns can be seen in Fig. 3.15a for a measurement on bunch 24 in beam 1 with chromaticity 15. The turn-by-turn vertical position is plotted in the bottom plot for the same time scale as the spectra. An instability is seen in the measured data for turns 0-10000 turns and a strong peak as 0.295 can be seen in the spectral plot for the same turns. After about 10000 turns the beam quality has been degraded but the sideband separated by the synchrotron tune Q_s can be seen in the spectral plot. After 30000 turns, a peak at the horizontal tune 0.27 with sidebands can be seen in the spectral plot indicating a coupling to the horizontal plane at this time.

Similarly, the spectral data of the vertical data of a measurement of bunch 24 in beam 1 at chromaticity 20 can be seen in Fig. 3.15b. The data is plotted in the bottom plot for the same bunch and turns. Here the FFT window was 5000 which means that the spectral plot has a higher resolution of the vertical axis. There is a peak at 0.295 in the spectral data at turns 0-20000 and a growth can be seen in the measured data at the same time. Then the vertical amplitude increases and a strong peak is visible in the spectral data going from 0.291 to 0.295 for turns 20000-50000. In the spectral data for turn 50000-150000 the highest peak varies between 0.291 and 0.295 which is about one Q_s wide. Additionally, sidebands with a distance of Q_s are visible in this region. At a high turn number, when the beam has already been degraded, there is coupling to the horizontal tune.

Lastly, the same analysis was conducted on the last bunch of a measurement with chromaticity 25, again using an FFT window of 5000 turns, and the results can be seen in Fig. 3.15c. The spectral plot has similar features compared to the plot in Fig. 3.15c however, the band between 0.291 and 0.295 is not visible until turn 100000, which is about 50000 turns later.

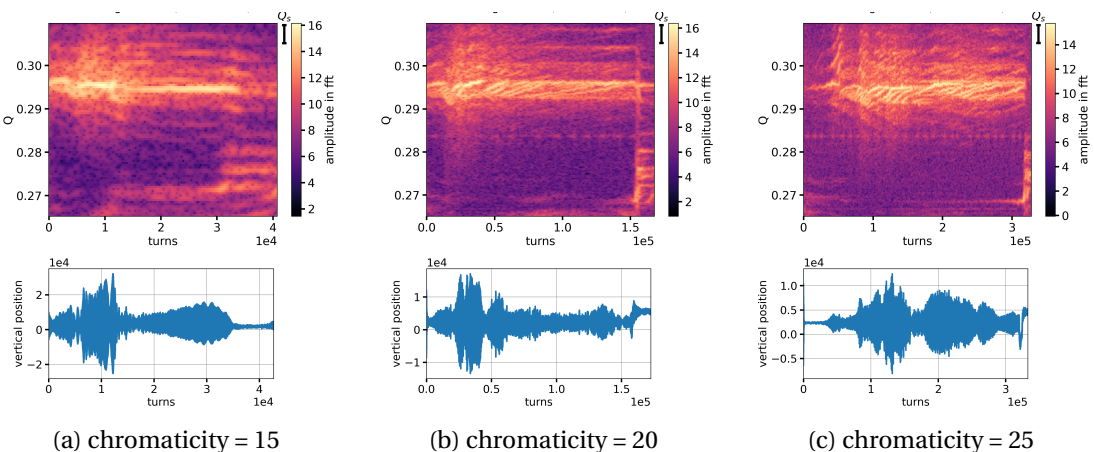


Figure 3.15: A rolling window FFT, top, over a set of measured data, bottom, for three different chromaticity settings.

Chapter 3. Experimental characterization of e-cloud driven instabilities in the LHC

Table 3.2: A summary of the simulation parameters used in the build-up simulations

	LHC Dipole	LHC quadrupole
Beam energy	450 GeV	
Bunch Intensity	1.2e11	
Bunch length	1.15 ns	
SEY	2.0	
E_{MAX}	332 eV	
Angular distribution	cosine_3D	
# macro-particles	2e6	5e5

3.1.5 Comparison with Simulations

Simulations were conducted to compare the model with the measured data. In these simulations, only single-bunch instabilities were considered, and no coupled bunch motion was taken into account. The simulations utilized the Vlasov model, as well as macro-particle simulations using the forces derived from the Vlasov model, as described in Sec. 1.4.

Build-up Studies

In order to build an accurate model of the e-cloud forces, the amount of e-cloud is estimated using build-up simulations performed with PyELOUD, as described in Sec. 1.4. In these measurements, to account for the beam screen state before conditioning, the SEY is estimated to be 2.0. Build-up studies were conducted in both dipoles and quadrupoles using the simulation parameters listed in Tab. 3.2.

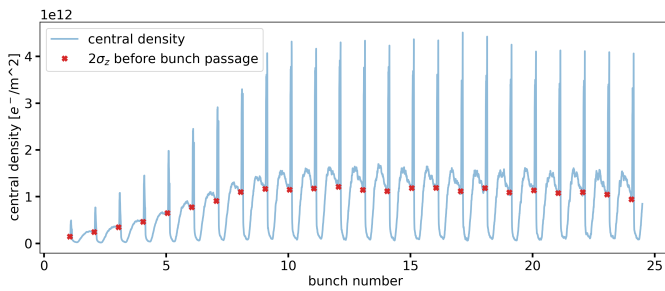
The electron density in the center of the beam pipe in a dipole with SEY = 2 during the passage of a 24-bunch train of intensity 1.2e11 ppb can be seen in Fig. 3.16a as a blue curve. When a bunch passes through the e-cloud the electrons are drawn towards the center of the pipe, causing a peak in central density. The density used to simulate responses is the density of the e-cloud right before a bunch passage, as the electron dynamics during the bunch passage need to be re-simulated for the distorted bunch. In Fig. 3.16a the density $2\sigma_z$ before each bunch passage is marked with a red cross. The density used to calculate the e-cloud forces is therefore $1e12 e/m^2$. The cross section of the e-cloud distribution in a dipole can be seen in Fig. 3.16b. The majority of the electrons are arranged in two vertical stripes away from the chamber center, however, there is a non-negligible amount of electrons between the two stripes. This is where the interaction with the beam occurs.

Similarly, the central density in a quadrupole magnet during the passage of the same 24 bunches used in the dipole simulations can be seen in Fig. 3.16c. The electron density $2\sigma_z$ before each bunch passage is again marked with red crosses. When a bunch passes through the e-cloud in a quadrupole, the central density is increased, which can be seen as the peaks in the blue curve. The peaks, reaching about $7e13$ electrons/ m^2 , are higher than the corresponding

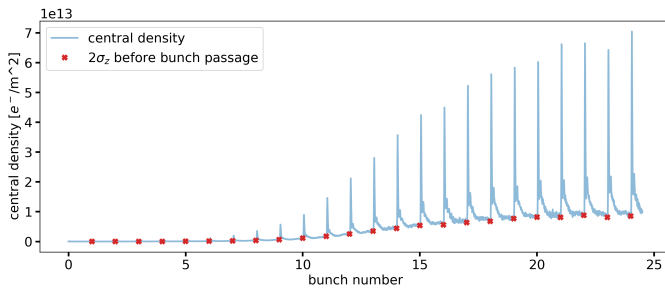
3.1 Measurements at high e-cloud conditions

peaks in the dipole magnets.

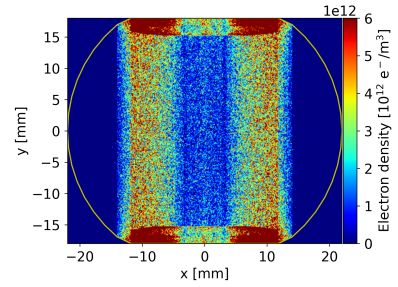
The cross section of the electron density in an LHC quadrupole after saturation of e-cloud density can be seen in Fig. 3.16d. The distribution is an average of the distribution right before the passage of bunches 16-24. The electrons have as expected arrange themselves in a cross determined by the quadrupolar field.



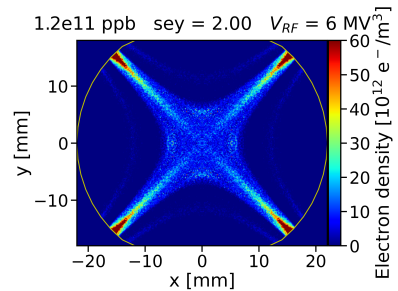
(a) The central electron density in a LHC dipole during a passage of 24 bunches 25 ns apart with a bunch intensity of $1.2 \cdot 10^{11}$ protons/bunch.



(c) The central electron density in a LHC quadrupole during a passage of 24 bunches 25 ns apart with a bunch intensity of $1.2 \cdot 10^{11}$ protons/bunch.



(b) The cross section of electron distribution in an LHC dipole at injection. The cross section is an average of the distributions right before bunch passages 15-23, which is after the central density has saturated.



(d) The cross section of electron distribution in an LHC quadrupole at injection. The cross section is an average of the distributions right before bunch passages 15-23, which is after the central density has saturated.

Figure 3.16: The electron density in the center of the beam pipe with SEY = 2, as a 24 bunch train of intensity $1.2 \cdot 10^{11}$ ppb and energy 450 GeV passes through. The e-cloud density just before each bunch passage, $2 \sigma_z$, is marked by a red cross in the two left plots. The two right plots display the electron distribution in a dipole and a quadrupole magnet.

Chapter 3. Experimental characterization of e-cloud driven instabilities in the LHC

Table 3.3: Simulations parameters for generating responses from e-cloud build-up in LHC dipoles and LHC quadrupoles with a SEY of 2.

	LHC Dipole	LHC Quadrupole
interaction points around the ring	8	
octupole current	0 A	
V_{RF}	6e6 V	
Transverse Damper	off	
# slices in along the bunch	200	
Macro-particles per slice	2500	
Fraction of device with magnets	60 %	7%
Magnetic field	0.54 T	12.1 T/m
cos and sin amplitude	$1e-4$	
# oscillations along the bunch	0-100	
Detuning fit order	20	10
SEY	2	

Modeling of the e-cloud forces

A set of responses was calculated using the same procedure described in Sec. 1.4 using the simulation parameters in Tab. 3.3. A bunch with a sinusoid bunch distortion was passed through the e-cloud distributions calculated in the previous section using single-pass PIC simulations. The resulting kick on the bunch as a function of the longitudinal coordinate z was calculated. The top plots in Fig. 3.17 display three different vertical bunch distortions with 1, 5, and 20 oscillations along the bunch respectively. The resulting vertical kick along the bunch, $\Delta p_y(z)$, is plotted in blue for the e-cloud distribution in the LHC dipoles, and in orange from the e-cloud distribution in the LHC quadrupoles.

The sum of the two responses is plotted in black in the bottom plots of Fig. 3.17 and is the kick a bunch going through both the e-cloud in LHC dipoles and LHC quadrupoles is assumed to experience.

The amplitude of the kicks from sine and cosine bunch distortions as a function of the number of oscillations along the bunch is plotted in Fig. 3.18a for the horizontal plane and in Fig. 3.18b in the vertical plane. The amplitudes from responses from the e-cloud in a dipole are plotted in red and the amplitudes resulting from the e-cloud distribution in quadrupoles are plotted in purple. In the horizontal plane, the amplitude of the responses from the e-cloud in dipoles is very small compared to the amplitude of the responses from the e-cloud in quadrupoles. The two purple curves, corresponding to the responses from cosine and sine horizontal bunch distortions both have a peak at 7 oscillations per bunch and then decrease until the amplitude is close to zero at 30 oscillations along the bunch. The amplitude of responses from distortions of a higher number of oscillations along the bunch is close to zero.

In the vertical plane, see Fig. 3.18b, the amplitude of the responses resulting from the e-cloud

3.1 Measurements at high e-cloud conditions

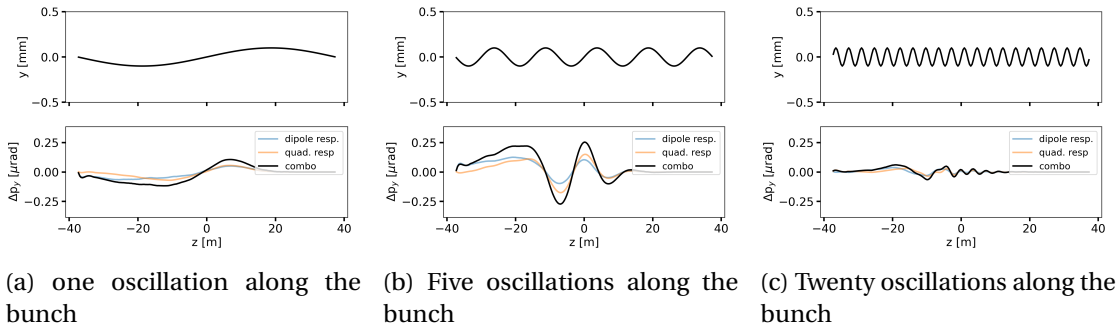


Figure 3.17: Sinusoid bunch distortions with three different numbers of oscillations along the bunch are plotted in black in the top plots. The responses to each distortion after one turn in the LHC are plotted in the bottom plots. The responses from e-cloud in dipoles are plotted in blue and the responses from e-cloud in quadrupoles are plotted in orange. The sums of the two responses are plotted in black.

distribution in the LHC quadrupoles is identical to the amplitude plot in the horizontal plane, as expected from the symmetry of the configuration. This is not the case for the red curves, which represent the amplitude of the responses from e-cloud in dipoles. For the dipoles, the amplitude of the responses resulting from cosine bunch distortions has an amplitude close to $1.5e-12$ for 1-6 oscillations along the bunch and then decreases with the number of oscillations until zero is reached as 40 oscillations along the bunch. In contrast, the amplitudes of the responses from sinusoid bunch distortions passing through the e-cloud build-up in the LHC dipoles have a peak of $3.3e-12$ at 7 oscillations along the bunch and then decrease until zero is reached at around 30 oscillations per bunch. The shape of this curve is similar to the amplitude of the responses from quadrupoles.

The detuning along the bunch, meaning the change in tune ΔQ as a function of the longitudinal coordinate, caused by the e-cloud in LHC dipoles (red) and LHC quadrupoles (purple) is plotted in Fig. 3.19 for the horizontal plane (left) and the vertical plane (right). The detuning obtained from PIC simulations is plotted in a lighter color and the polynomial fit used to model the detuning is plotted in a darker shade. The purple lines are seemingly identical in the horizontal and vertical plane with a peak of $\Delta Q = 1.5e-2$ at the center of the bunch. Again, this is to be expected as the e-cloud distribution is symmetric in the horizontal and vertical plane in an LHC quadrupole, see Fig. 3.16d. The red curve on the left, corresponding to the detuning along the bunch from the e-cloud in LHC dipoles in the horizontal plane, has a wide peak of $\Delta Q = 0.25e-2$ at the center of the bunch. This peak is about 15% of the height observed peak from quadrupoles. In the vertical plane, the red curve has one major wide peak at the center of the bunch of $\Delta Q = 1.25e-2$ and a local maximum towards the tail of the bunch at $z = -0.3$ of $\Delta Q = 1.0e-12$.

In summary, in the horizontal plane the forces acting on the bunch come mostly from the e-cloud in the quadrupoles whereas in the vertical plane, the contribution from the e-cloud in dipoles is comparable with the contribution from quadrupoles. In the machine, the bunches

Chapter 3. Experimental characterization of e-cloud driven instabilities in the LHC

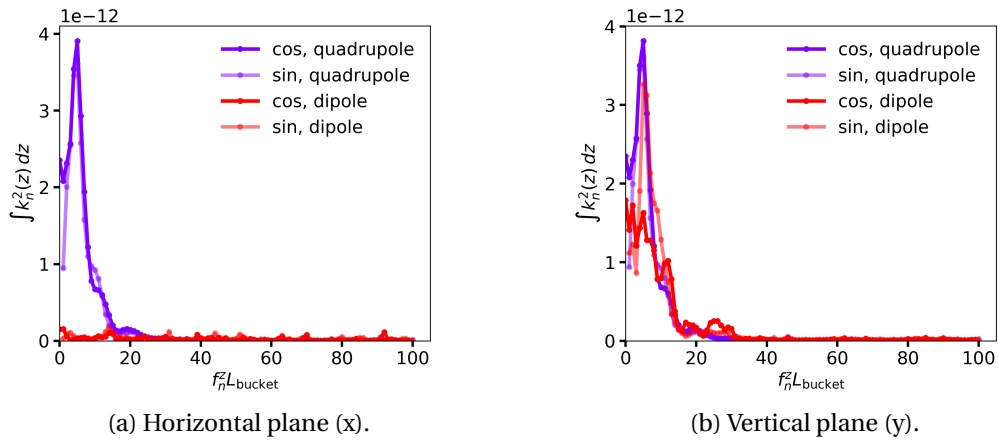


Figure 3.18: The amplitude of the responses (resulting kick) from sinusoids (transparent lines) and cosine (opaque lines) transverse bunch distortions passing through the e-cloud in LHC quadrupoles (purple) and LHC dipoles (red) as a function of number of oscillations along the bunch.

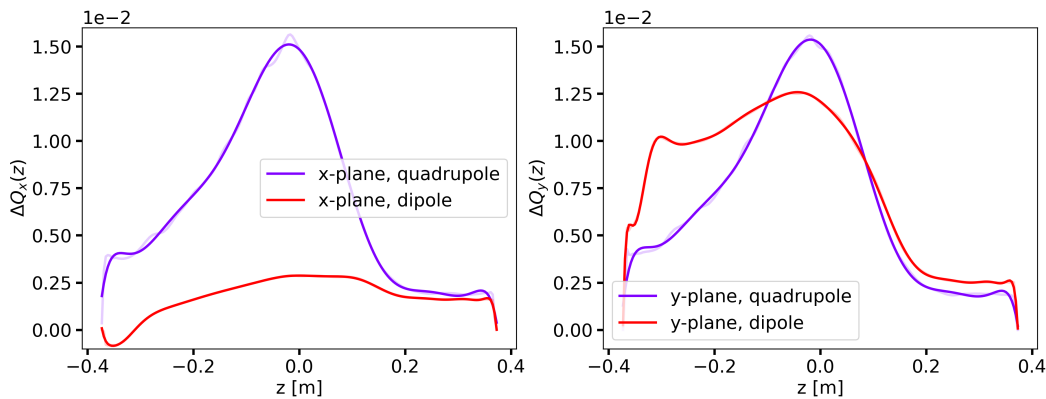


Figure 3.19: The detuning along the bunch from quadrupoles (purple) and dipoles (red) in the horizontal plane (left) and the vertical plane (right). The simulated detuning is plotted as transparent lines, and the polynomial fit used in the force model is plotted as solid lines.

3.1 Measurements at high e-cloud conditions

would be affected by both the e-cloud in quadrupoles and the e-cloud in dipoles, therefore the sum of the force contribution from both is used in the following simulations.

Instability simulations with strong e-cloud

Simulations of the beam dynamics in the vertical plane were conducted using the force model presented in the previous section. The other simulation parameters were the same as in Chapter 2, see Tab. 2.1 and Tab. 2.2. In building the force model, the assumption that the SEY was the same in all magnets along the ring was made. In reality, this assumption does not hold true, as the SEY varies between different magnets within the machine, as noted in a previous study [79]. The assumption of a uniform SEY may be overly simplistic. Consequently, we explore different e-cloud strengths to find the best match for the observed instabilities. This exploration is based on the assumption that an uneven distribution of e-cloud within the machine can be effectively described by a smooth e-cloud model with a specific e-cloud strength. As a reminder, e-cloud strength 1 corresponds to the e-cloud built up in the LHC magnets where all magnets have an SEY of 2.

Firstly, the comparison of measured growth rates and the simulated growth rates from macro-particle simulations of various e-cloud strengths as a function of chromaticity can be seen in Fig. 3.20. The measured growth rates from beam 1 and beam 2, also plotted in Fig. 3.11, are plotted as blue and red dots with error bars. The growth rates from simulations with e-cloud only in dipoles are plotted as a dotted line. The simulations with comparable growth rates are the simulations with an e-cloud strength of 0.75, however, the simulated growth rate does not follow the behavior of the measured data well.

The growth rates from simulations with e-cloud only in quadrupoles with an e-cloud strength of 0.75 are plotted as a dashed black line. This line follows the measured growth rates well. However, in the machine, it is expected to have contributions from e-cloud in both dipoles and quadrupoles.

The blue and green curves correspond to the simulation with even e-cloud in both quadrupoles and dipoles for strength 0.4, and 0.5 respectively. These lines have similar behaviors to the measured data, however, the simulated growth rates are about 50% higher and flatten out at chromaticity 20 instead of 15 where the measured growth rates flatten out. Lastly, the growth rate from macro-particle simulations with an e-cloud strength of 0.2 from dipoles and an e-cloud strength of 0.5 from quadrupoles is plotted in red. This line starts at a growth rate of 60 s^{-1} at chromaticity 5 which is within the errorbar of the measured growth rate of beam 2. Then the red curve decreases with chromaticity but slower than the measurements until it flattens at chromaticity 20.

The best agreement with simulations is achieved with simulation including only e-cloud in quadrupoles for e-cloud strength 0.75. The estimated e-cloud from build-up simulations was expected to be high since it assumed a SEY of 2 for all magnets, meaning an e-cloud at 75% of that could be reasonable. However, since the instabilities were very clear in the vertical plane, we know that there is a contribution from e-cloud in dipoles because it affects the vertical and the horizontal plane differently, whereas e-cloud in quadrupoles affects the two transverse planes the same.

3.1 Measurements at high e-cloud conditions

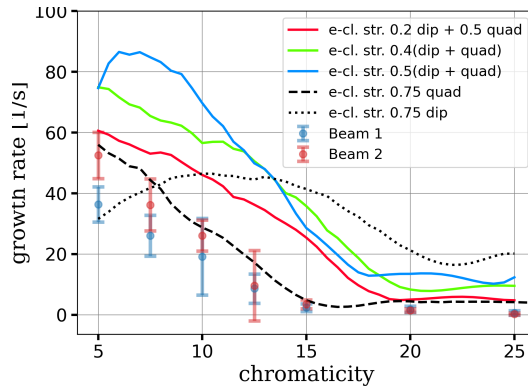


Figure 3.20: The growth rate from measurements of beam 1 (blue dots) and beam 2 (red dots) together with the growth rates from various simulations. Simulations only including e-cloud in LHC quadrupoles at e-cloud strength 0.75 are plotted as a dashed black line and simulations only including e-cloud in LHC dipoles also at e-cloud strength 0.75, are plotted as a dotted black line. Simulations with e-cloud strengths 0.4 and 0.5 with even e-cloud from both LHC dipoles and LHC quadrupoles are plotted in green and blue. Finally, the growth rates of simulations including e-cloud from dipoles at e-cloud strength 0.2 and e-cloud from quadrupoles at e-cloud strength 0.5 are plotted in red.

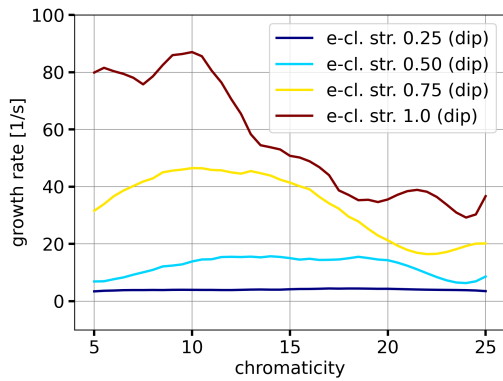
From simulations with e-cloud in both dipoles and quadrupoles, a comparable but not exact growth rate could be achieved with an e-cloud strength of 0.4. The estimate of an even SEY might be too simple to accurately predict the effect of the real e-cloud in the LHC on the beam dynamics. However, a stabilizing effect of a similar slope can be seen in both measurements and macro-particle simulations. Note that the force model used is the simplified formalism developed for the Vlasov approach and not a full PIC simulation.

The growth rates obtained from the entire set of simulations that were conducted are reported in Fig. 3.21. The decreasing trend with chromaticity is observed in most of the cases.

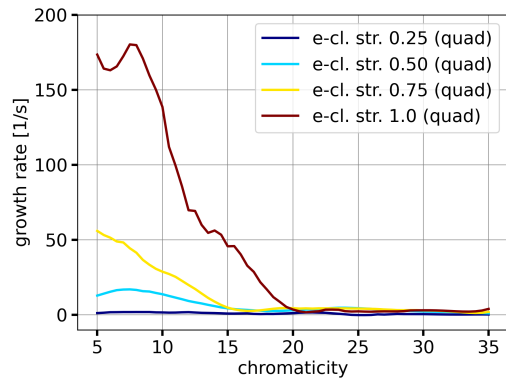
In Fig. 3.22 we compare for the same case plotted in Fig. 3.20 the results of macroparticle simulations and Vlasov calculations. The same behavior discussed in Sec. 2.2 is observed, with good agreement between the two methods when one dominant mode is present and additional damping visible in the macroparticle simulations when the Vlasov approach predicts a large number of weakly unstable modes.

Figure 3.23 shows the corresponding spectral content. As observed in the measurements, see Fig. 3.12, the dependence of more frequencies on chromaticity is rather weak.

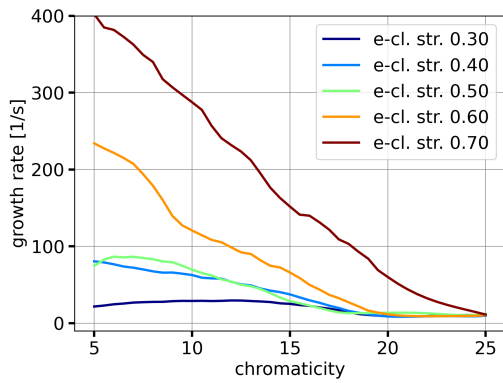
Chapter 3. Experimental characterization of e-cloud driven instabilities in the LHC



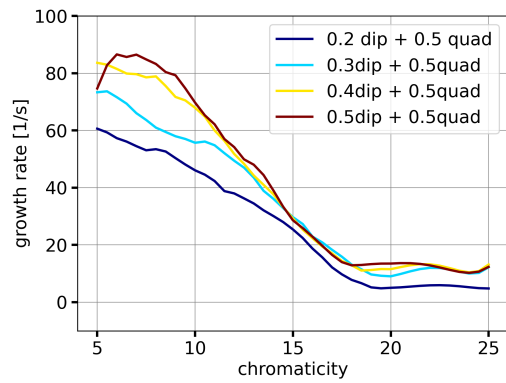
(a) Only e-cloud in LHC dipoles.



(b) Only e-cloud in LHC quadrupoles.



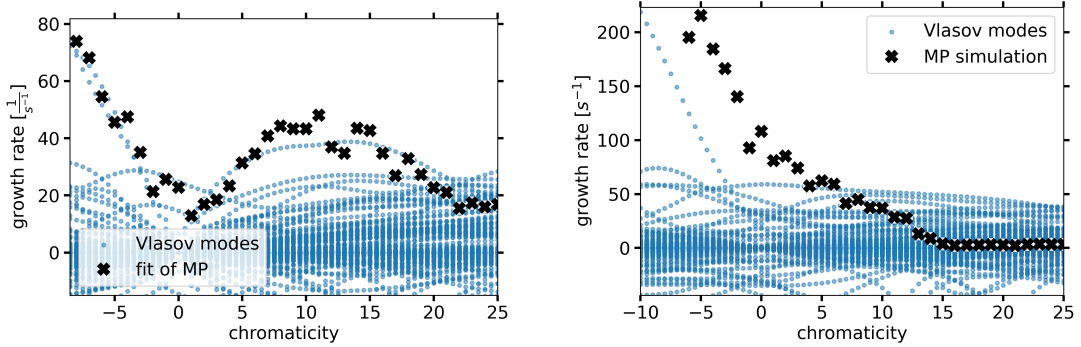
(c) e-cloud in both LHC dipoles and LHC quadrupoles



(d) A fixed e-cloud strength in LHC quadrupoles of 0.5 and varying e-cloud strength in LHC dipoles.

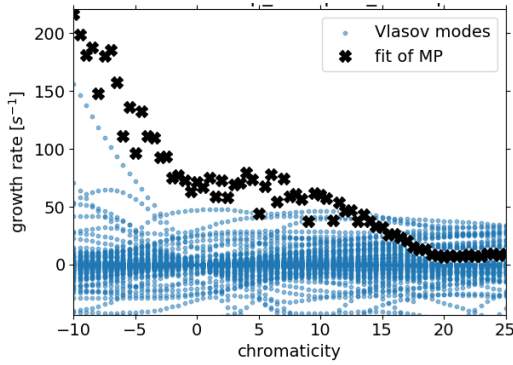
Figure 3.21: The instability growth rate in the vertical plane was calculated from macro-particle simulations using the Vlasov formalism of e-cloud forces for several configurations of e-cloud in the LHC. An e-cloud strength 1 corresponds to an SEY of 2 in all magnets.

3.1 Measurements at high e-cloud conditions

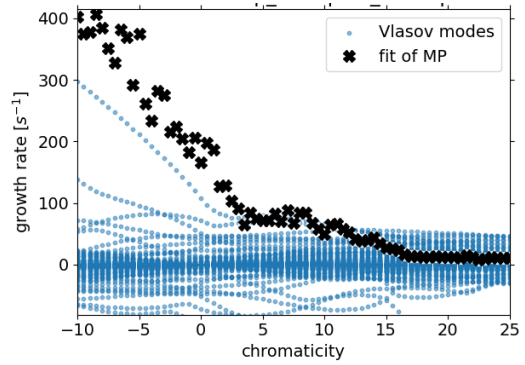


(a) E-cloud strength 0.75, only e-cloud in LHC dipoles

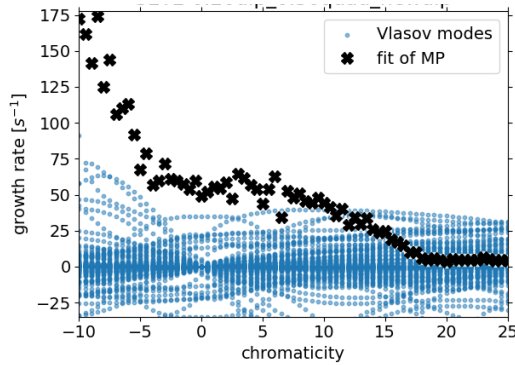
(b) E-cloud strength 0.75, only e-cloud in LHC quadrupoles



(c) e-cloud strength 0.4, even contribution from LHC quadrupoles and LHC dipoles.



(d) e-cloud strength 0.5, even contribution from LHC quadrupoles and LHC dipoles.



(e) e-cloud strength 0.2 from LHC dipoles and 0.5 from LHC quadrupoles.

Figure 3.22: The negative imaginary part of the complex mode frequency of the Vlasov modes at each chromaticity is plotted as blue dots. The instability growth rate from macro-particle tracking simulations is plotted as a black cross at each chromaticity.

Chapter 3. Experimental characterization of e-cloud driven instabilities in the LHC

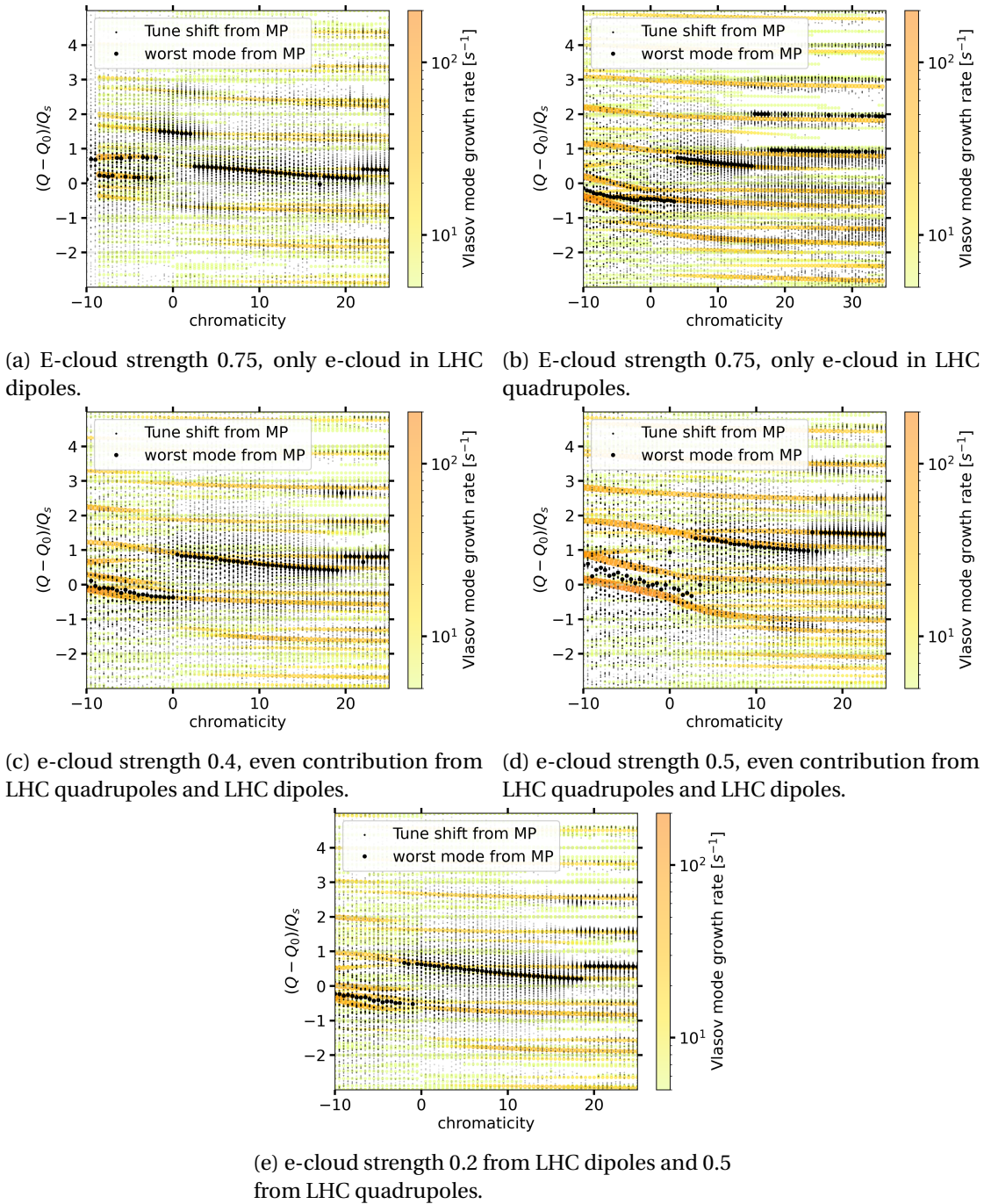


Figure 3.23: The tune shift calculated from the Vlasov approach, plotted as dots in a yellow-orange color map, and the spectral analysis of the macro-particle tracking simulations, black dots. The highest peak of the macro-particle spectra is marked with a big dot at each chromaticity.

3.2 Measurements of octupole thresholds after conditioning

In the LHC, e-cloud driven instabilities are mitigated by chromaticity, momentum-dependent detuning, and octupole magnets by inducing amplitude detuning [80]. Octupole magnets introduce non-linear effects in the machine and it is therefore of interest to operate with as low octupole fields as possible [81]. In the following section the sign of the octupole is defined such that a positive current corresponds to a positive amplitude detuning in the horizontal plane [82]. Measurements were conducted at the LHC to determine at what octupole current e-cloud driven instabilities were no longer stabilized by the octupole magnets. Simulations predict weaker instabilities at higher bunch intensities [83]. To confirm this prediction the octupole threshold was measured for three different bunch intensities.

3.2.1 Methodology

Beams with the filling scheme of 12 bunches + four trains of 72 bunches were injected into the LHC, meaning a total of 300 bunches were injected in each beam. Bunch intensities of 1.8×10^{11} , 1.4×10^{11} and 1.1×10^{11} protons/bunch were tested. Each injection followed the following procedure:

1. Inject at high chromaticity and high octupoles
2. Lower chromaticity to a specific value. Chromaticities 5, 25, 20 and 25 were used.
3. Slowly lower the octupole strengths until an instability is observed
→ this octupole current is the octupole threshold for that bunch intensity and chromaticity.

The total intensity, in blue for beam 1 and red for beam 2, as a function of time can be seen in Fig. 3.24. The octupole current is plotted in grey, with the scale on the right axis. The first four fills had a bunch intensity of 1.8×10^{11} protons/bunch with chromaticity 25, 20, 15, and 5 respectively. The following three fills had a bunch intensity of 1.4×10^{11} protons/bunch with chromaticities 25, 15 and 5 respectively. Lastly, the three last fills had a bunch intensity of 1.1×10^{11} protons/bunch also with the chromaticities 15, 15, and 5 respectively. When the octupole current is lowered past its threshold, transverse instabilities occur, causing the beam to dump.

3.2.2 Measured Thresholds

If the beam is unstable in the transverse plane the amplitude of the transverse position starts to grow and/or the transverse emittance increases.

The transverse position was monitored turn by turn and bunch by bunch. The maximum absolute transverse bunch position of the four 72-bunch trains in beam 1 is plotted as a

Chapter 3. Experimental characterization of e-cloud driven instabilities in the LHC

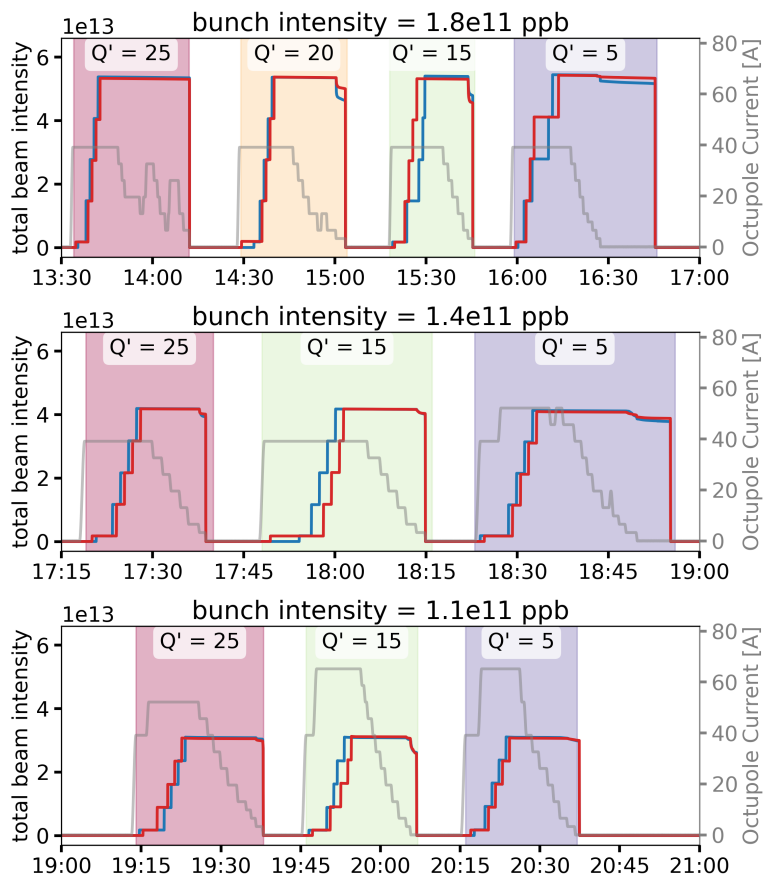


Figure 3.24: The figure shows the ten fills that were done during these measurements. The four fills of the first row had a bunch intensity of $1.8e11$ protons/bunch, the three new fills had a bunch intensity of $1.4e11$ protons/bunch and the three fills on the last row had a bunch intensity of $1.1e11$ protons/bunch. The chromaticity of each fill is marked with a colored area, where red corresponds to a chromaticity of 15, yellow to a chromaticity of 20, green to a chromaticity of 15, and blue to a chromaticity of 5.

3.2 Measurements of octupole thresholds after conditioning

function of time in Fig. 3.25 as blue crosses every 5 s. Similarly, the emittance was monitored but was recorded less frequently, about every 25 s, and is plotted as light blue dots. The scale on the y-axis is arbitrary and normalized with the maximum recorded emittance and the maximum recorded transverse position respectively. The data from the horizontal plane is plotted as the top plots whereas the data from the vertical plane is plotted in the bottom plots. The octupole current is plotted in the same time interval.

In the fill with bunch intensity 1.1×10^{11} protons/bunch and chromaticity 5, Fig. 3.25a, both the vertical emittance and the vertical position start to grow when the octupole current was changed to 38 A. The horizontal position and emittance also start to grow after the vertical plane becomes unstable.

A fill with the same intensity but with chromaticity 25 was also performed and the resulting maximum emittance and transverse position as a function of time can be seen in Fig. 3.25b. There is a hint of emittance growth when the octupole current is lowered to 13 A in the vertical plane and a hint of vertical amplitude growth when the octupole current is 20 A. Then, both plane becomes strongly unstable when the octupole current is lowered to 10 A.

The maximum emittance and transverse position for fills with bunch intensity 1.4×10^{11} protons/bunch and chromaticity 5 can be seen in Fig. 3.25c and for chromaticity 25 in Fig. 3.25d. At octupole current 20 A in Fig. 3.25c, there is an emittance growth in the vertical plane. This is before anything is seen in the transverse position in either plane. Both the horizontal emittance and the vertical emittances start to grow at the same time in Fig. 3.25d, at octupole current 6 A. The transverse position in both planes also starts to grow at the same time.

Finally, the fills with bunch intensity 1.8×10^{11} protons/bunch resulted in the maximum emittances and transverse positions seen in Fig. 3.25e for chromaticity 5 and Fig. 3.25f for chromaticity 25. For chromaticity 5 the horizontal emittance and position start to grow at octupole current 10 A, whereas the vertical counterparts start to grow about a minute later when the octupole current is lowered to 6 A. In Fig. 3.25f, the horizontal emittance grows a few percent when the octupole current is lowered to 13 A, a growth that is not visible in the vertical plane. However, both planes see an emittance growth that stabilizes at a higher value at octupole current 6 A. At this time, a peak in the vertical transverse position can be seen, which is later suppressed to nominal values.

In summary, the vertical plane becomes unstable before the horizontal plane for low intensity and low chromaticity. For high chromaticity and/or high bunch intensity, there is not a clear dominant plane, as instabilities are seen in the two planes roughly at the same time.

To get an overview of the dependence on the octupole current the maximum transverse position and the maximum emittance for the four 72-bunch trains at each time is plotted as a function of the octupole current. During some of the fills, the octupole current was increased when the first sign of instability was detected, which might give misleading results if the emittance is directly mapped onto the octupole current at each time. To remove this effect,

Chapter 3. Experimental characterization of e-cloud driven instabilities in the LHC

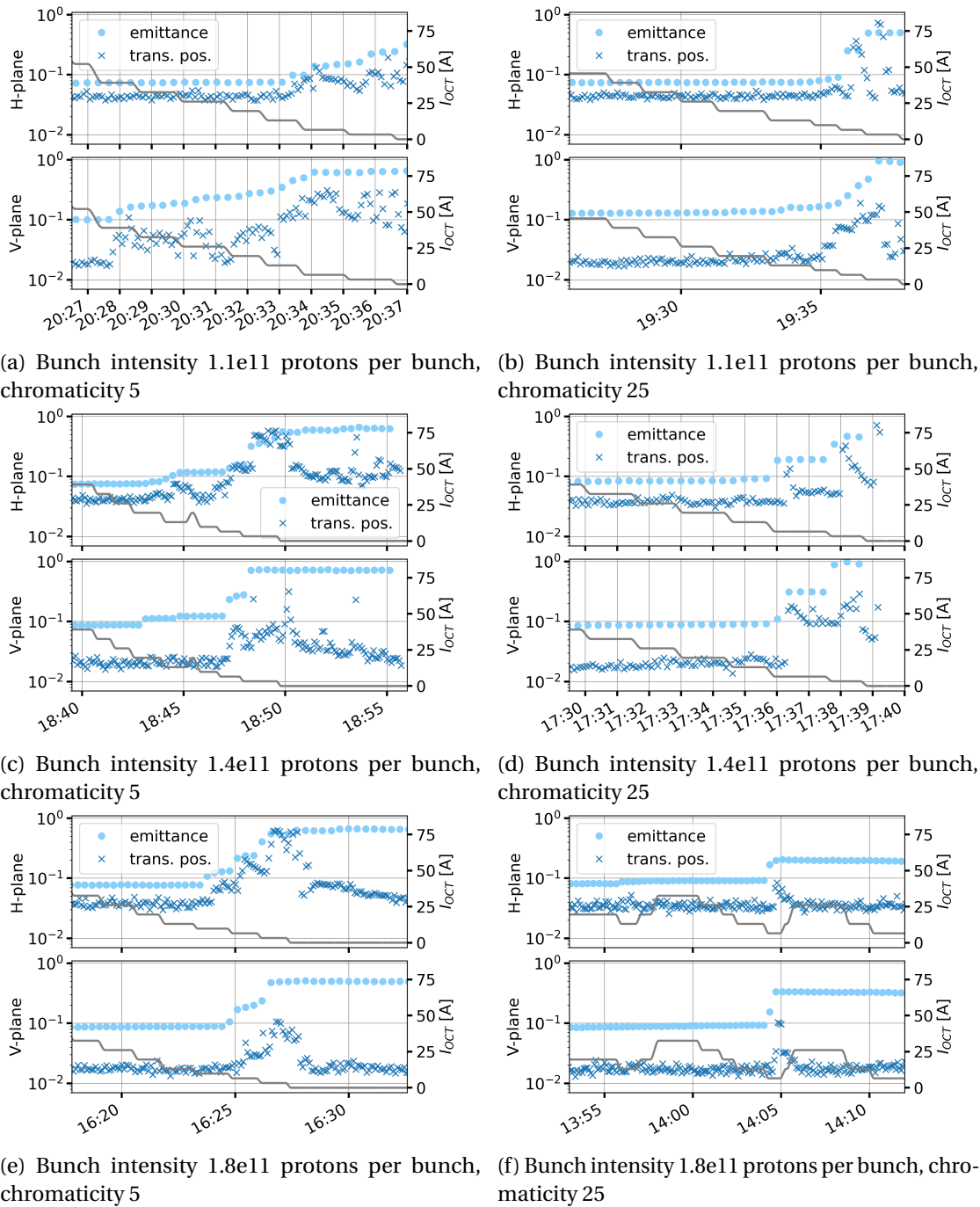


Figure 3.25: The maximum emittance, light blue dots, and the maximum transverse position, blue crosses, of the four 72-bunch trains as a function of time. The horizontal data (top plots) and the vertical data (bottom plots) are plotted for six different fills of beam 1. The octupole current, grey, is plotted as a function of time with the scale plotted on the right-hand side.

3.2 Measurements of octupole thresholds after conditioning

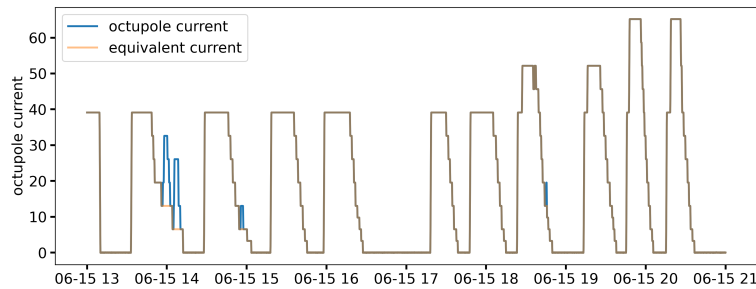


Figure 3.26: The octupole current during the measurements is plotted in blue, and the equivalent octupole current used to map emittance and transverse position to octupole current is plotted in orange.

the emittance is mapped onto the equivalent octupole current, plotted in orange in Fig. 3.26.

The maximum emittance among the four trains of 72 bunches as a function of octupole current is plotted for beam 1 Fig. 3.27. The horizontal emittance is plotted as whole lines and the vertical emittance is plotted as dotted lines on a logarithmic scale. The color of the line corresponds to the bunch intensity of the fill. The emittance for all the fills with chromaticity 5 is plotted in the top graph, the fills with chromaticity 15 are reported in the middle plot, and the fills with chromaticity 25 are reported in the bottom plot. As the octupole current approaches zero, all plotted emittances exhibit fast growth. The highest octupole current at which there is a first hint of emittance growth is considered to be the octupole current threshold. The corresponding emittances for beam 2 can be seen in Fig. 3.29.

Similarly, the maximum transverse position of the bunches in the four 72-bunch trains is plotted as a function of octupole current in Fig. 3.28 for beam 1 and in Fig. 3.30 for beam 2. The maximum transverse position shows a similar behavior to the maximum emittance with respect to octupole current.

To get the octupole threshold, the emittance data was studied carefully, and the highest octupole current at which the first sign of instability was identified. The resulting thresholds for beam 1 (top) and beam 2 (bottom) in horizontal (left) and vertical (right) can be seen in Fig. 3.31. The octupole thresholds for bunch intensity $1.8e11$ protons/bunch are plotted in red, for bunch intensity $1.4e11$ protons/bunch in green, and for bunch intensity $1.1e11$ protons/bunch in blue. The instability threshold is higher in the vertical plane for bunch intensity $1.1e11$ and $1.4e11$ protons/bunch, whereas the thresholds are equivalent in horizontal and vertical for bunch intensity $1.8e11$ protons/bunch.

The highest threshold for each plane and beam at each value of chromaticity is plotted in Fig. 3.32 for all three bunch intensities. Beams with higher bunch intensity consistently show lower octupole thresholds.

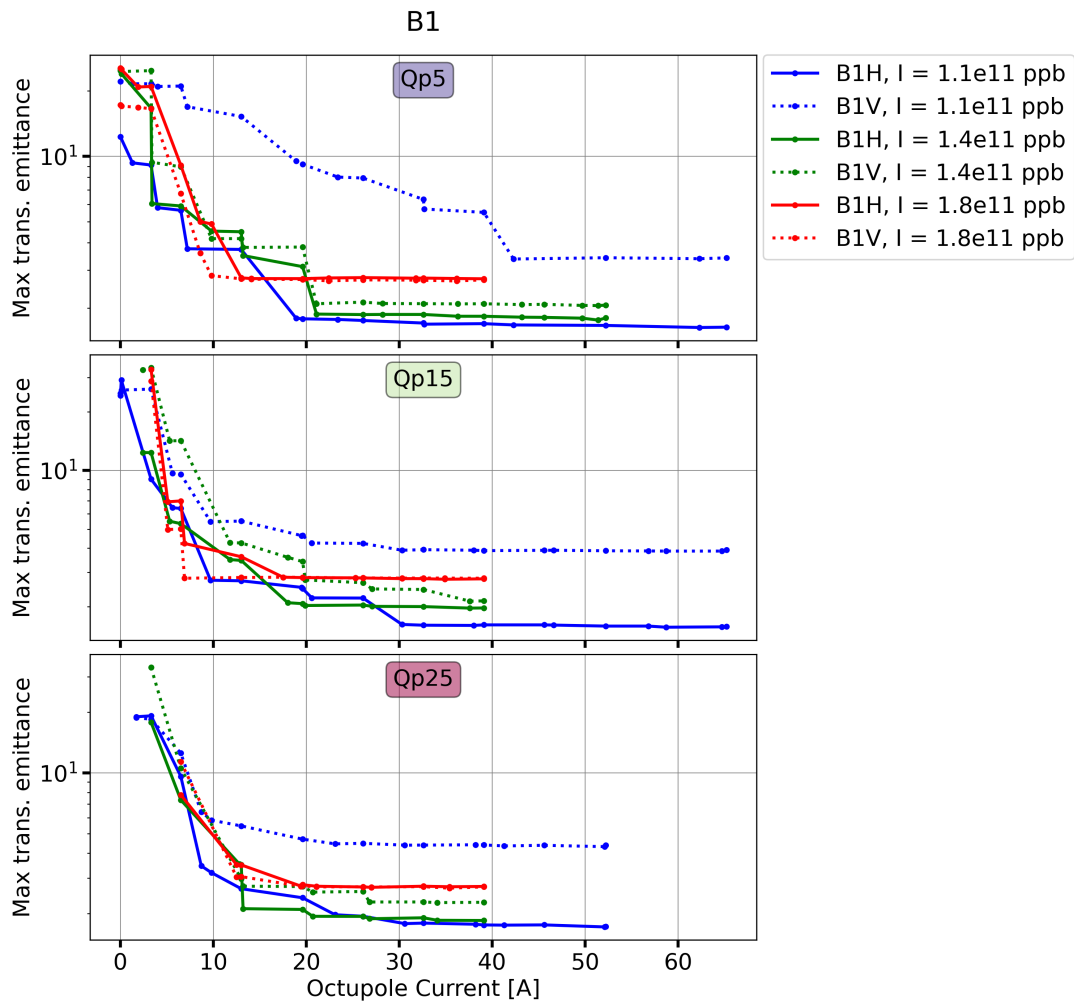


Figure 3.27: The figure contains the maximum bunch emittance of the four 72-bunch trains emitted into beam 1 of the LHC. Results from fills with chromaticity 5 are plotted in the top plot, from chromaticity 15 in the middle plot, and from chromaticity 25 in the bottom plot. The color of each line corresponds to the bunch intensity where red, green, and blue correspond to $1.8e11$, $1.4e11$, and $1.1e11$ protons/bunch respectively. The horizontal emittance is plotted as dotted lines and the vertical emittance as whole lines.

3.2 Measurements of octupole thresholds after conditioning

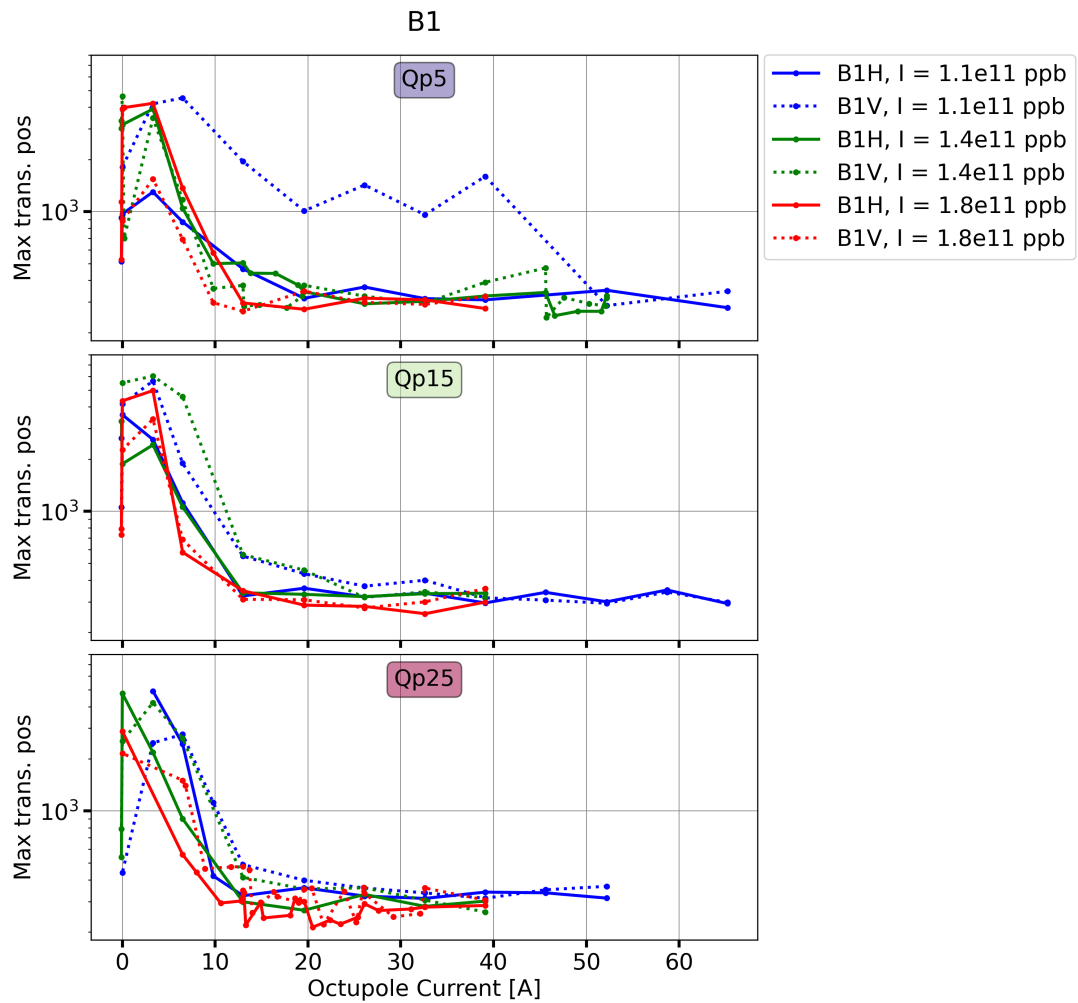


Figure 3.28: The figure contains the maximum transverse position of the four 72-bunch trains emitted into beam 1 of the LHC. Results from fills with chromaticity 5 are plotted in the top plot, from chromaticity 15 in the middle plot, and from chromaticity 25 in the bottom plot. The color of each line corresponds to the bunch intensity where red, green, and blue correspond to $1.8e11$, $1.4e11$, and $1.1e11$ protons/bunch respectively. The horizontal emittance is plotted as dotted lines and the vertical emittance as whole lines.

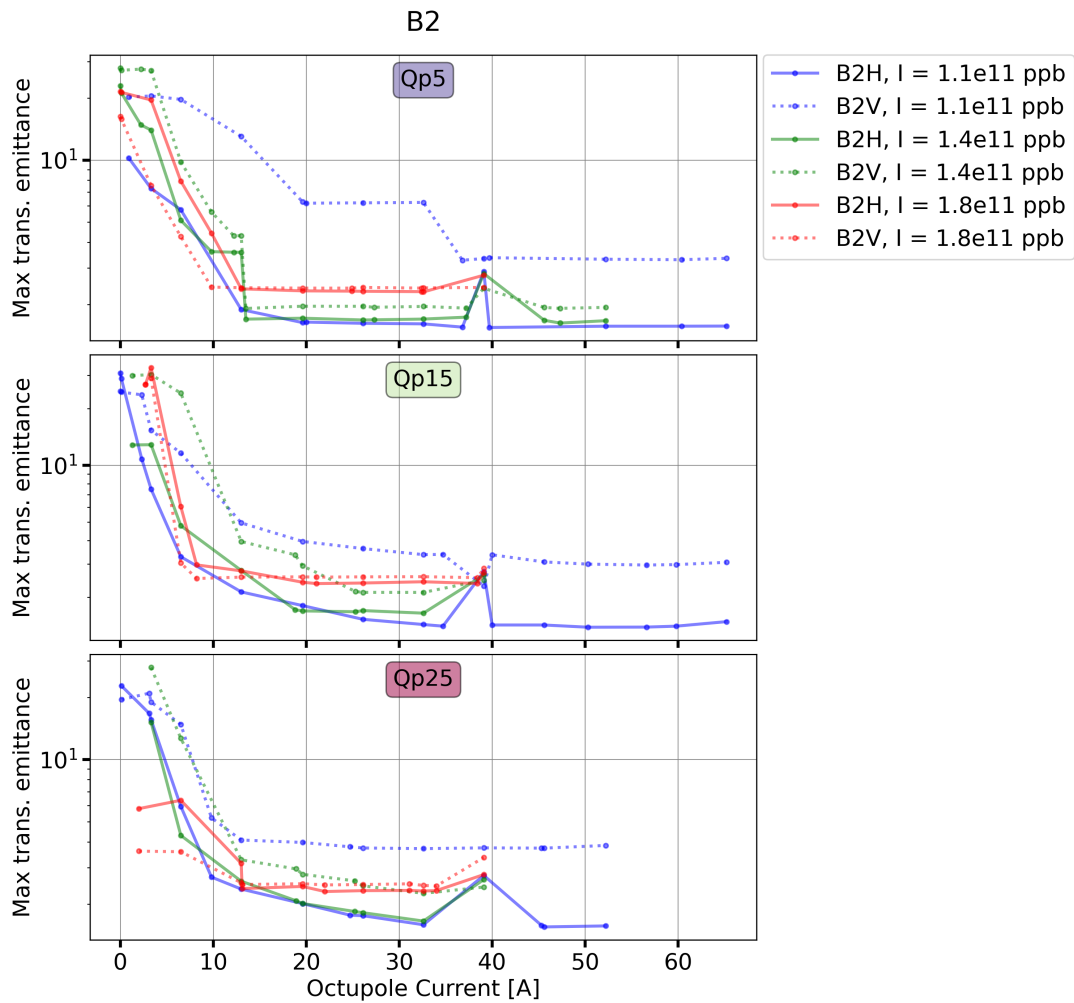


Figure 3.29: The figure contains the maximum bunch emittance of the four 72-bunch trains emitted into beam 2 of the LHC. Results from fills with chromaticity 5 are plotted in the top plot, from chromaticity 15 in the middle plot, and from chromaticity 25 in the bottom plot. The color of each line corresponds to the bunch intensity where red, green, and blue correspond to $1.8e11$, $1.4e11$, and $1.1e11$ protons/bunch respectively. The horizontal emittance is plotted as dotted lines and the vertical emittance as whole lines.

3.2 Measurements of octupole thresholds after conditioning

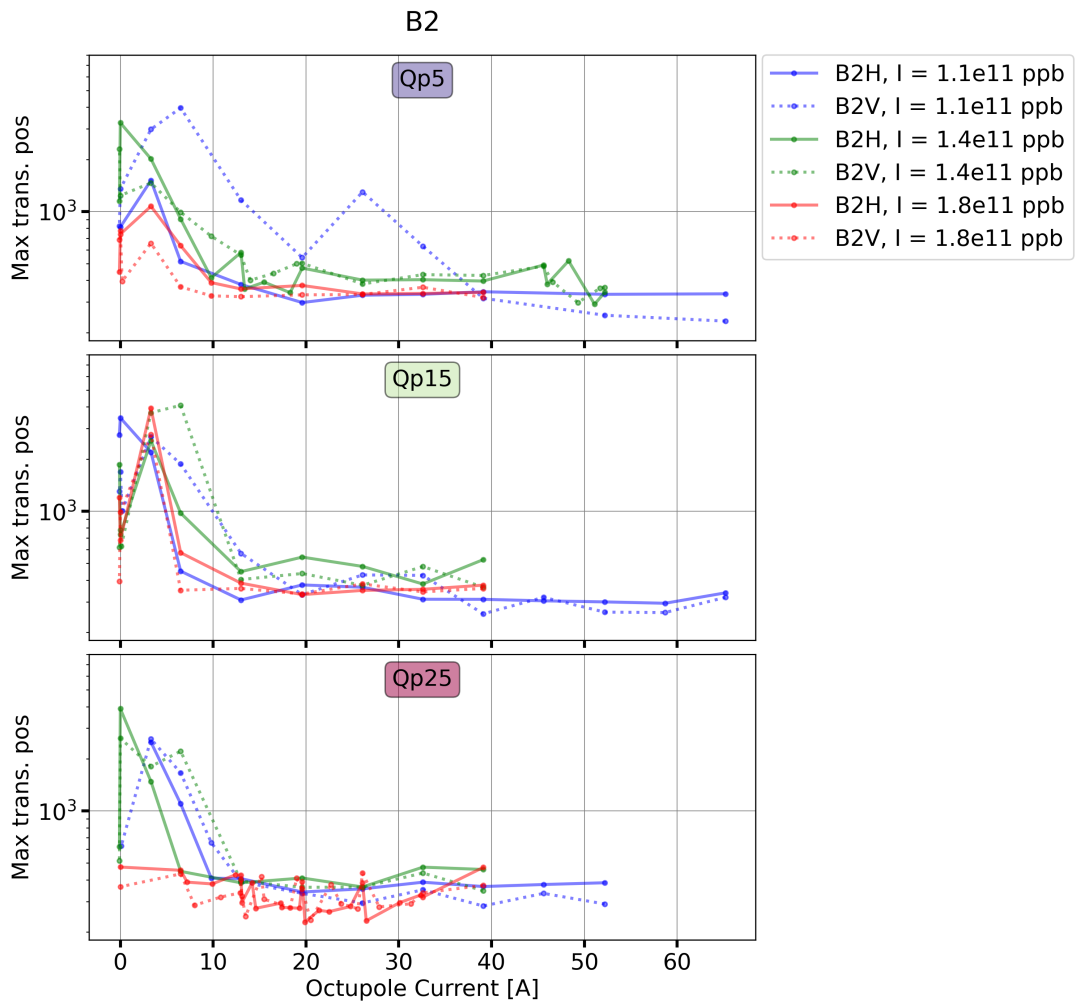


Figure 3.30: The figure contains the maximum transverse position of the four 72-bunch trains emitted into beam 2 of the LHC. Results from fills with chromaticity 5 are plotted in the top plot, from chromaticity 15 in the middle plot, and from chromaticity 25 in the bottom plot. The color of each line corresponds to the bunch intensity where red, green, and blue correspond to 1.8e11, 1.4e11, and 1.1e11 protons/bunch respectively. The horizontal emittance is plotted as dotted lines and the vertical emittance as whole lines.

Chapter 3. Experimental characterization of e-cloud driven instabilities in the LHC

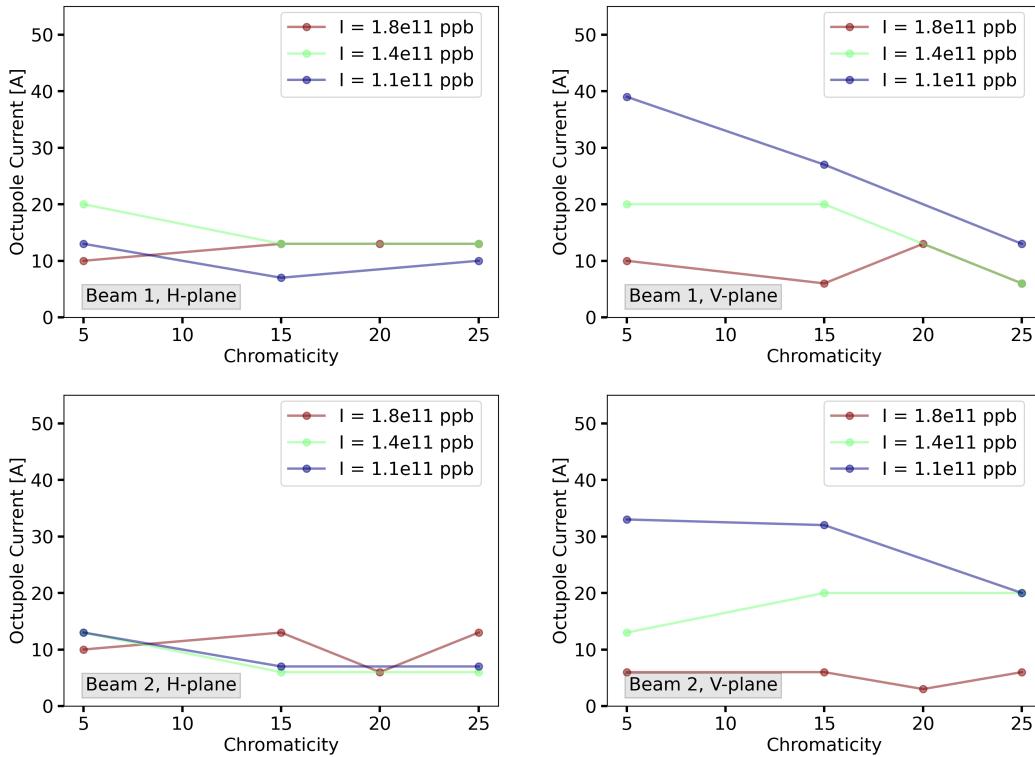


Figure 3.31: The octupole current thresholds for bunch intensity $1.8e11$ protons/bunch (red), $1.4e11$ protons/bunch (green), and $1.1e11$ protons/bunch (blue) as a function of chromaticity for beam 1 (top) and beam 2 (bottom) in horizontal (left) and vertical (right) planes.

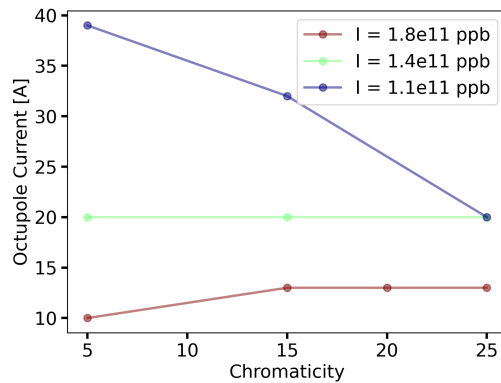


Figure 3.32: The highest octupole current thresholds of the two planes and the two beams for bunch intensity are $1.8e11$ protons/bunch (red), $1.4e11$ protons/bunch (green), and $1.1e11$ protons/bunch (blue) as a function of chromaticity.

3.2 Measurements of octupole thresholds after conditioning

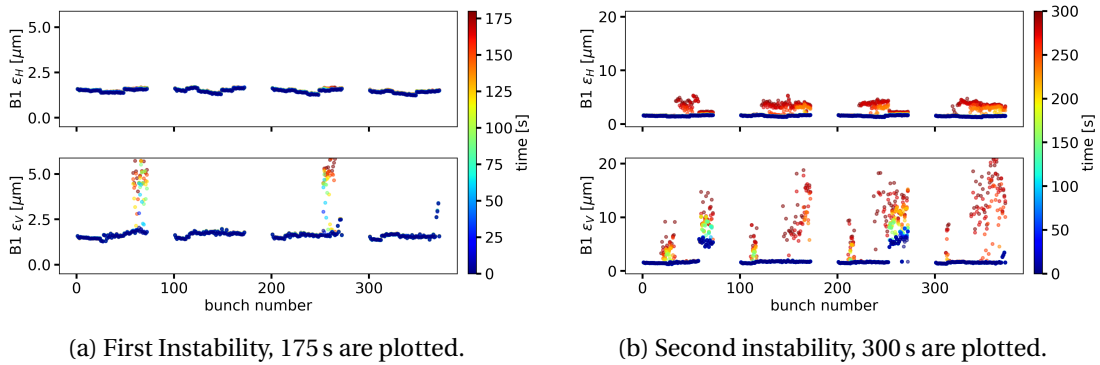


Figure 3.33: The emittance of each bunch along the four bunch trains of 72-bunches for beam 1 during a fill with 1.1×10^{11} protons/bunch and chromaticity 5. The color of the dot corresponds to time chronologically from blue to red.

3.2.3 Observed instabilities

Low bunch intensity

The emittance along the train at the onset of an instability recorded for the fill in beam 1 with bunch intensity 1.1×10^{11} protons/bunch and chromaticity 5 can be seen in Fig. 3.33a for both the horizontal (top) and vertical (bottom) planes. The color of the dot corresponds to the time passed, with blue corresponding to the selected reference ($t = 0$) and red to 175 s after the reference time. No change in emittance is observed at this time in the horizontal plane and all emittances are stable at around $2 \mu\text{m}$. In the vertical plane, some bunches towards the end of the last train are already blown up from injection. The later bunches in train 1 and train 3 have their emittances blown up during the 175 s plotted in the figure. The emittances in both planes for the next 300 s are plotted in Fig. 3.33b, meaning the reference time, plotted in deep blue, corresponds to the last time plotted in Fig. 3.33a. All of the trains are now unstable, both the later bunches and a few bunches earlier in the train. Also, a small emittance increase can be seen in the horizontal plane.

The turn-by-turn vertical position for bunch 60-72 in train 1 can be seen in Fig. 3.34 for the first onset of instability while the second observed instability, one and a half a minute later is shown in Fig. 3.34b. The bunches become unstable at different times from one another, with growing vertical amplitude but are then stabilized without causing a beam dump.

The growth rates were estimated by using a rolling window FFT fit described in Sec. 3.1.3. The vertical data of bunch 64 of train 1 at the onset of the first instability is plotted in blue in Fig. 3.34a and at the onset of the second instability in Fig. 3.34b. The data that is used in the fit is the data between the two grey, dashed, and vertical lines. Varying the window size and overlap of the rolling FFT window results in growth rates between the green and red lines with the average growth rate being plotted in black. The estimated growth rate of the first instability is 0.56 s^{-1} and 0.35 s^{-1} for the second instability which corresponds to rise times of $\tau \sim 20000$ turns and $\tau \sim 32000$ turns.

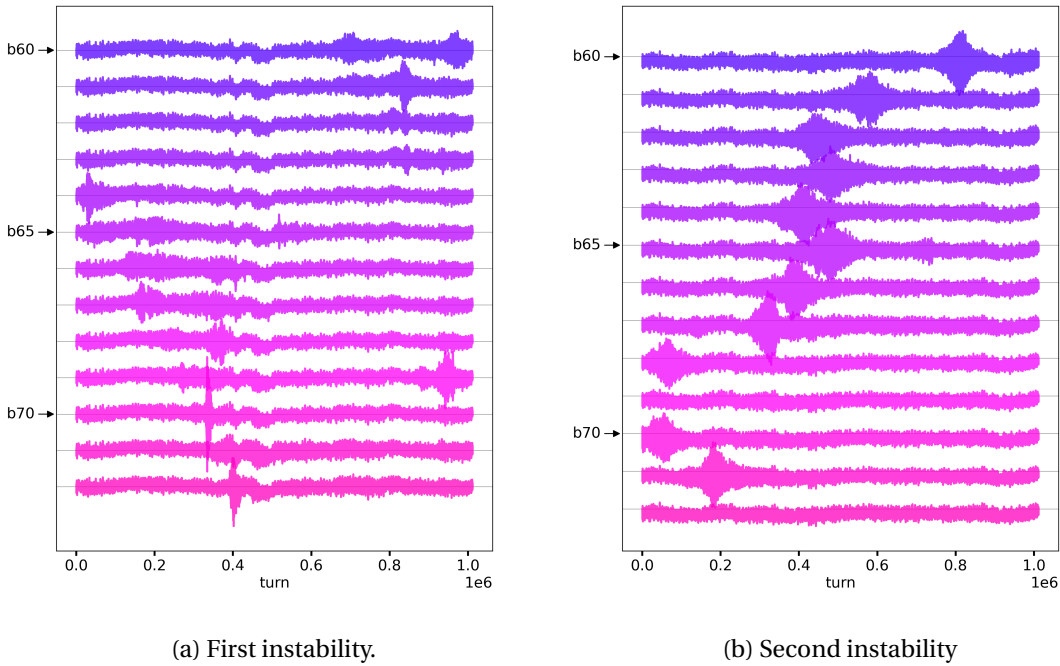


Figure 3.34: The vertical position turn-by-turn of bunch 60-72 in bunch train 1 for beam 1 during a fill with 1.1×10^{11} protons/bunch and chromaticity 5. The unit on the y-axis is arbitrary.

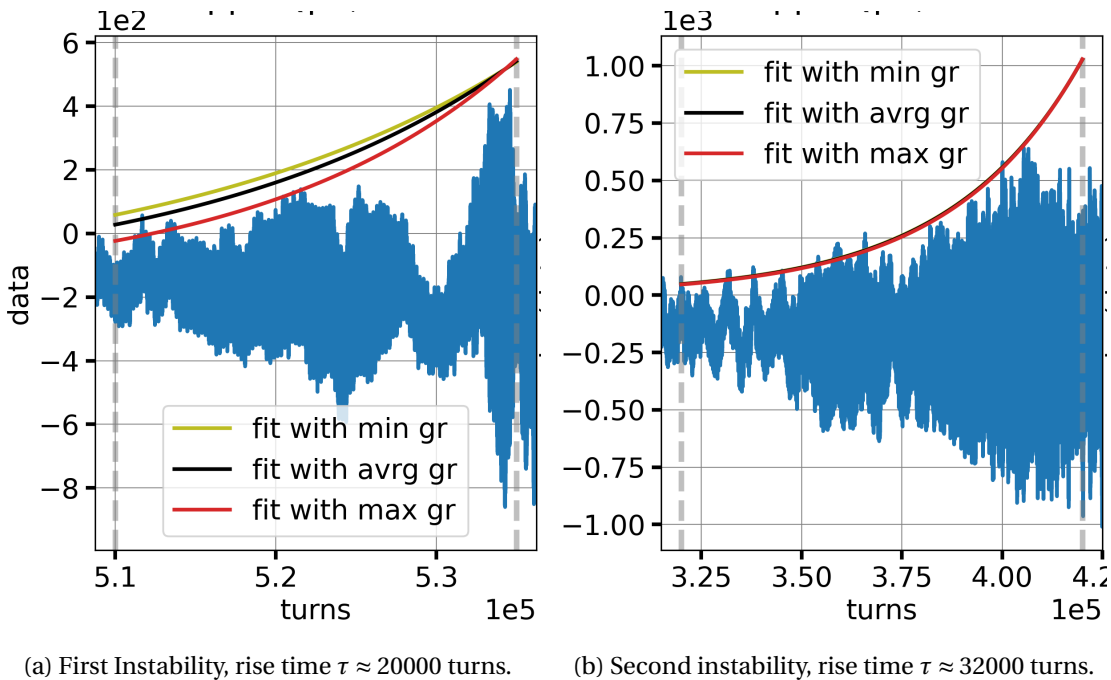


Figure 3.35: The vertical position of bunch 64 in bunch train 1 in beam 1 during a fill with bunch intensity 1.1×10^{11} protons/bunch and chromaticity 5 is plotted in blue. The green, black, and red curves correspond to the low, average, and high estimates of the growth rate using the rolling window FFT fitting method described in Sec. 3.1.3

3.2 Measurements of octupole thresholds after conditioning

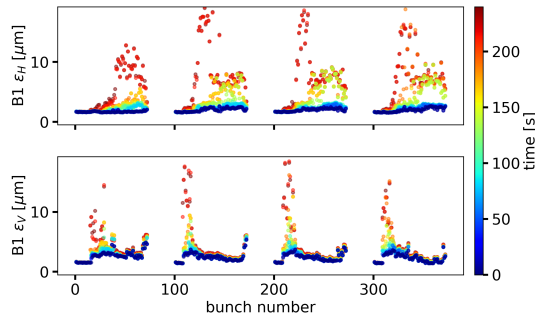


Figure 3.36: The emittances during 250 s at the onset of instabilities during a fill of beam 1 with bunch intensity 1.1×10^{11} protons/bunch and chromaticity 25.

The bunch-by-bunch emittances in both planes obtained during a fill of beam 1 with bunch intensity 1.1×10^{11} protons/bunch and chromaticity 25 can be seen in Fig. 3.36. The color of each dot indicates the time. In the horizontal plane, the later bunches in each train experience emittance growth, with the emittance growth seemingly proportional to the bunch position for the first 150 s plotted. After 150 s, a fast blowup occurs for bunches in the middle of trains two, three, and four. In the vertical plane, bunches early in the train experience the most emittance growth.

To get an overview of the transverse motion during this instability, the amplitude of the horizontal motion of train 2 is plotted in Fig. 3.37a and the amplitude of the vertical motion of the same train at the same time in Fig. 3.37b. Turn-by-turn data of 10^5 turns are plotted for the 72 bunches in the train. The x-axis corresponds to the turn number and the y-axis to the bunch number. The scale of the amplitude is given by the colorbar on the right side of each plot. In the horizontal plane, several of the bunches in the range 20-50 are unstable whereas bunches in the range 7-20 are unstable in the vertical plane. The instabilities in the horizontal plane start around turn 50 000 whereas the instabilities in the vertical plane start at turn 30 000, meaning the instabilities start in the vertical plane.

The rise times of the single bunch instabilities observed in the vertical plane during this fill was about 8000 turns.

3.2.4 High bunch intensity

The transverse emittances recorded during 250 s at the onset of instability for the fills with bunch intensity 1.8×10^{11} protons/bunch can be seen in Fig. 3.38. The left plot, Fig. 3.38a, contains results for chromaticity 5 and the later two-thirds of the trains show emittance growth in both planes during the full 250 s. The horizontal plane is slightly worse than the vertical plane. In the right plot, Fig. 3.38b, the chromaticity is instead 25. Here, the latter two-thirds of the train also shows emittance growth in both planes with the horizontal plane being slightly worse. However, the emittance grows only during the first 100 s. This is because the octupole current was increased when the first instability was seen, see the grey line in Fig. 3.25f. The rise

Chapter 3. Experimental characterization of e-cloud driven instabilities in the LHC

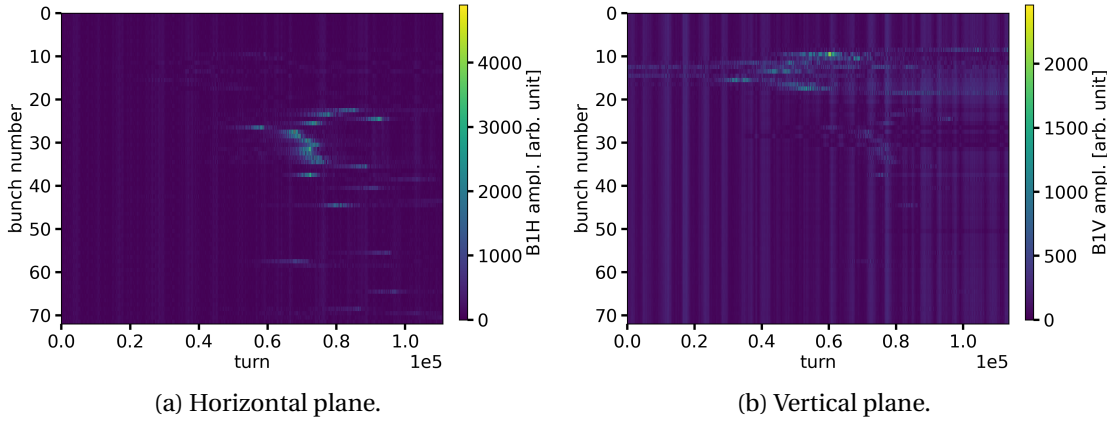


Figure 3.37: The amplitude of the transverse motion of the 72 bunches in train 2 in beam 1 plotted turn-by-turn for 50 000 turns. The bunch intensity is 1.1×10^{11} protons/bunch and the chromaticity is 25.

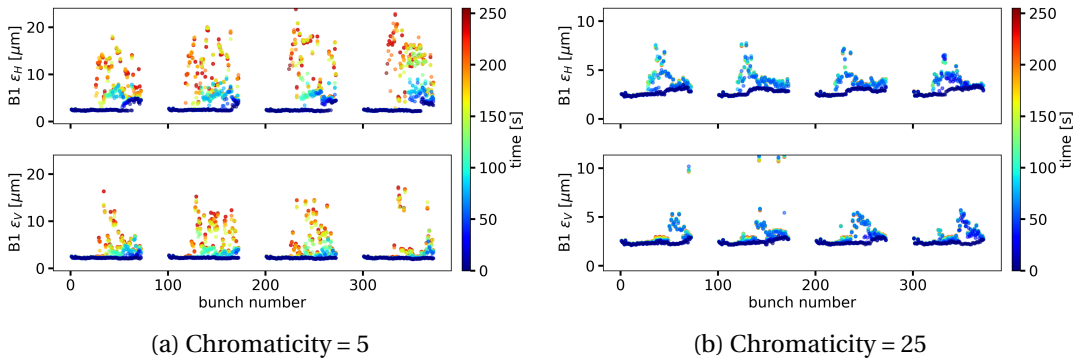


Figure 3.38: The emittances during 250 s at the onset of instabilities during a fill of beam 1 with bunch intensity 1.8×10^{11} protons/bunch.

times were estimated to $\tau \sim 14000$ turns at chromaticity 5 and $\tau \sim 5000$ turns at chromaticity 25.0.

The corresponding bunch-by-bunch transverse amplitudes for train 2 are plotted in Fig. 3.39 for the fills in beam 1 with bunch intensity 1.8×10^{11} protons/bunch. In all four plots, the y-axis represents the bunch position and the x-axis corresponds to time measured in turns. The horizontal amplitude of the fill with chromaticity 5 is plotted in Fig. 3.39a and the vertical amplitude of the same beam is plotted in Fig. 3.39c. Bunches 50-70 have a high amplitude in the horizontal plane, indicating instabilities. The same bunches have a slightly higher amplitude compared to the earlier bunches in the vertical plane, but the amplitude is not as high as in the horizontal plane.

When chromaticity is set to 25, the horizontal amplitude of bunch 20-40 is slightly larger compared to the rest of the bunches, see Fig. 3.39b. No visible bunch-by-bunch pattern is visible in the vertical plane.

3.2 Measurements of octupole thresholds after conditioning

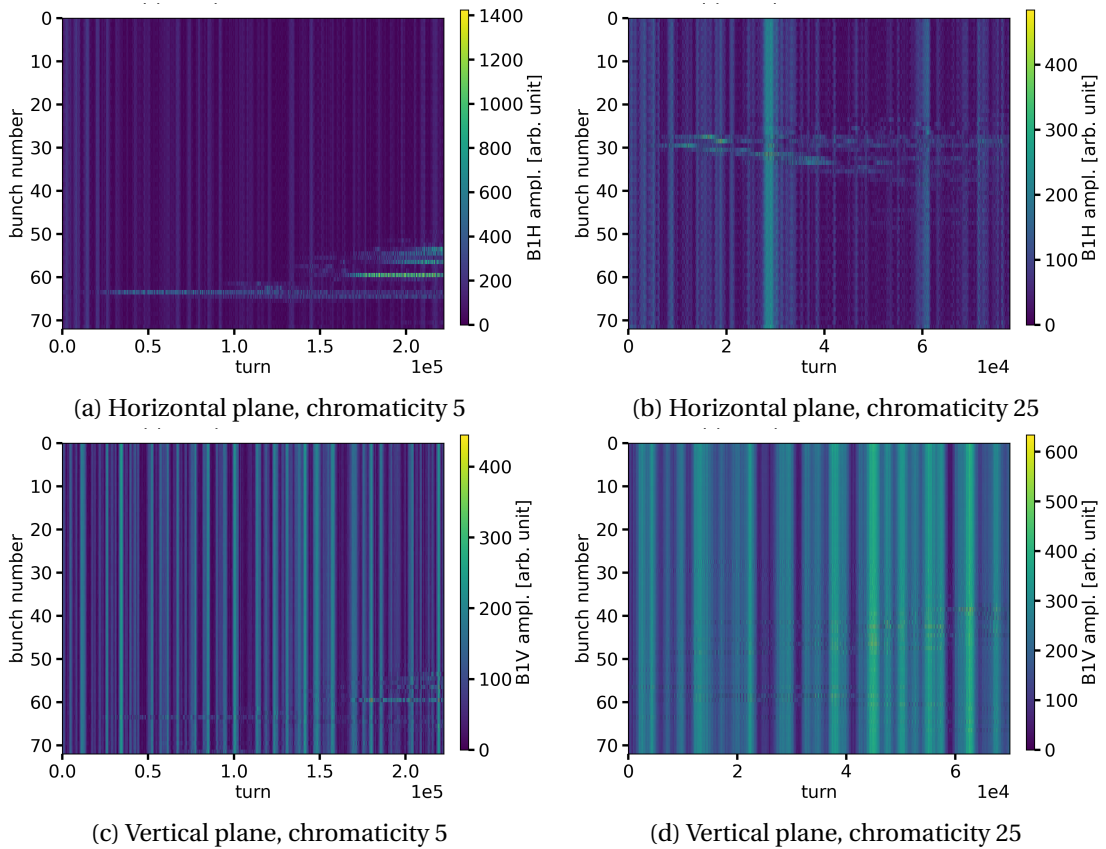


Figure 3.39: The amplitude of the transverse motion of the 72 bunches in train 2 in beam 1 plotted turn-by-turn. The bunch intensity is 1.8×10^{11} protons/bunch.

These plotted fills with bunch intensity 1.8×10^{11} protons/bunch shows that the horizontal plane becomes unstable before the vertical plane for both high and low chromaticity.

In summary, the observations were dominated by vertical instabilities for low intensity and low chromaticity, however, both planes become unstable at the same time for high intensity and or high chromaticity.

Chapter 3. Experimental characterization of e-cloud driven instabilities in the LHC

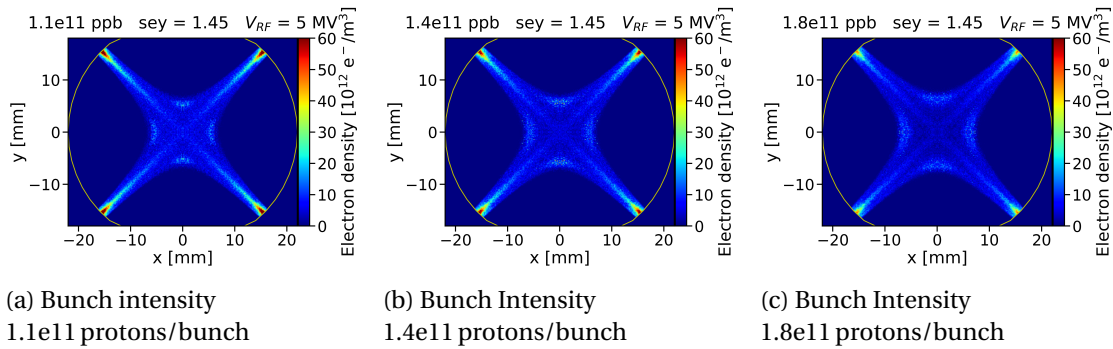


Figure 3.40: The three figures show the transverse cross-section of the electron distribution in the beam chamber of a LHC quadrupole after build-up saturation for three difference bunch intensities. The distribution shown is right before a bunch passage.

3.2.5 Simulations

Build-up simulations were performed using parameters consistent with the conditions in the LHC at injection for the three bunch intensities used during the measurements. The SEY varies along the LHC but all sectors are estimated to have an SEY between 1.35 and 1.45 [79]. In these simulations, the accelerator is approximated to have an even SEY along the whole machine of 1.45, which is a high estimate. The electrons arrange themselves differently in the beam chamber depending on the magnetic fields present as well as the bunch intensity. The resulting cross sections of electrons in LHC quadrupoles after the electron density has saturated can be seen in Fig. 3.40. The electrons are arranged as a cross following the field lines of the quadrupole magnet for all three bunch intensities. The electron density is higher the lower the bunch intensity, but the difference is subtle.

Similarly, the cross section of the electron distribution in LHC dipoles for the same simulation parameters can be seen in Fig. 3.41 for the three bunch intensities 1.1e11, 1.4e11, and 1.8e11 protons/bunch. The majority of the electron arrange themselves in two vertical stripes and the distance between the stripes increases with increased bunch intensity. A result of this is that the central density of electrons decreases with increased bunch intensity. In Fig. 3.41a there are some electrons visible in the center of the beam pipe, something that is not visible for the two higher intensities, see Fig. 3.41b and Fig. 3.41c.

The central density of electrons building up in LHC dipoles and quadrupoles for the three bunch intensities 1.1e11 (purple), 1.4e11 (green), and 1.8e11 (red) protons per bunch as a function of bunch passages is plotted as dashed lines in Fig. 3.42. The central density in dipoles is very low for bunch intensity 1.4e11 and 1.8e11 protons/bunch. In the same graph, the central electron density as a result of bunch passages with a bunch intensity 1.1e11 protons/bunch grows to about $2e11 e^-/m^2$. This decrease in central density in dipoles with increased bunch intensity is consistent with expectation [84].

In quadrupoles, see whole lines in Fig. 3.42, the shape of the central density as a function of

3.2 Measurements of octupole thresholds after conditioning

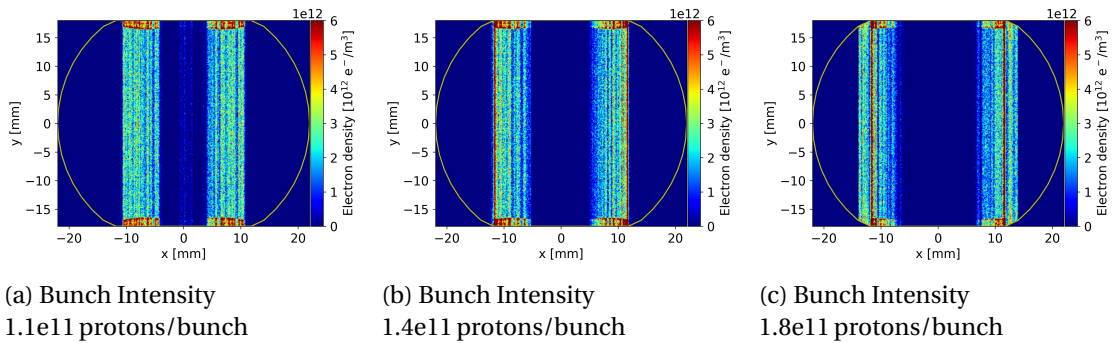


Figure 3.41: The three figures show the transverse cross section of the electron distribution in the beam chamber of a LHC dipole after build-up saturation for three different bunch intensities. The distribution shown is right before a bunch passage.

bunch passages is similar for all three intensities. What differs the three bunch intensities is the saturated value of electron density in the center of the beam pipe which decreases with increased bunch intensity.

The e-cloud formed in quadrupoles drive both horizontal and vertical instabilities whereas the e-cloud in dipoles drives vertical instabilities [69]. The observation of dominant vertical instabilities as bunch intensity 1.1e11 protons/bunch is therefore consistent with the predicted higher e-cloud in dipoles only at this intensity. For the other two intensities, the e-cloud in the quadrupole is the most dominant which could explain why similar instabilities can be observed in the two transverse planes.

The observation of instabilities becoming less pronounced for increased bunch intensity is consistent with the decreased electron density in dipoles and quadrupoles, which is observed in the simulations.

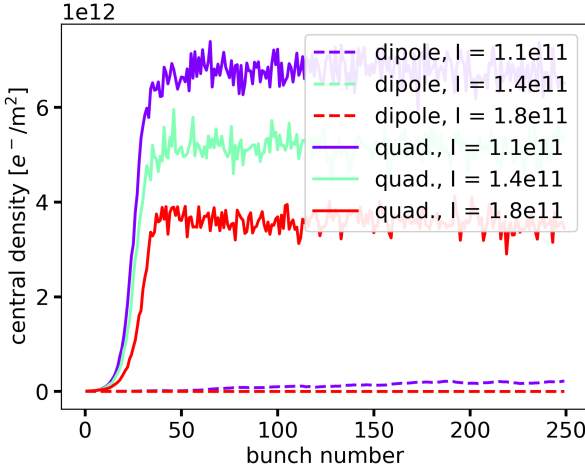


Figure 3.42: The electron density at the center of the beam pipe in LHC quadrupoles (whole lines) and LHC dipoles (dashed lines) as a result of e-cloud buildup in dipole and quadrupole magnets bunch intensity 1.1×10^{11} protons/bunch (purple), 1.4×10^{11} protons/bunch (green) and 1.8×10^{11} protons/bunch (red) as a function of time measured in bunch passages.

4 Conclusions

E-cloud resulting in both dipolar forces and a detuning along the bunch have been expressed in a dedicated Vlasov formalism for e-cloud forming in dipole as well as quadrupole magnets. This formalism also includes chromaticity. The adjustment of chromaticity to acceptable positive values is one of the mitigation strategies used against e-cloud driven instabilities in the LHC. As expected, the Vlasov formalism predicts a stabilizing effect with increasing chromaticity. Additionally, when chromaticity is included the growth rate of the strongest mode decreases whereas the growth rates of the weaker modes increase, which is consistent with theory.

The Vlasov simulations were benchmarked against macroparticle simulations using the Py-HEADTAIL as a particle tracker but using the same description for the e-cloud forces developed for the Vlasov approach. The tune shift of the Vlasov modes agrees well with the tune shift calculated from the spectral analysis of the macroparticle simulations. Also on the growth rate there is good agreement as long as there is only one dominant unstable mode. However, at high chromaticity, where multiple weakly unstable modes are expected by the Vlasov method, there is a stabilizing mechanism in the macroparticle simulations that is not captured in the linearized Vlasov approach.

This discrepancy is not observed when no detuning along the bunch from the e-cloud is included in either simulation, meaning the case when only the dipolar forces from the e-cloud were taken into account. For this case, the Vlasov modes accurately predict the behavior of the macroparticle tracking simulations for all ranges of chromaticity. To understand the stabilizing mechanism, the quadrupolar force from the e-cloud was further investigated. It was found that Vlasov modes agree with the macro-particle simulations also when no detuning with longitudinal amplitude, ΔQ_R , was included in either simulation and only the head-tail phase shift from e-cloud is included.

To further test the Vlasov model, impedance forces were implemented in the same force formalism as e-cloud with the forces being divided into dipolar forces and a detuning along the bunch. The macroparticle simulations using this force formalism agree with conventional

Chapter 4. Conclusions

PyHEADTAIL impedance simulations for the full range of chromaticity. This suggests that the force formalism used in the e-cloud Vlasov approach is not the source of the discrepancy. Consistently with the observations made with the e-cloud, Vlasov calculations agree with the macroparticle simulations for all cases except for the case with both positive chromaticity and a detuning with longitudinal amplitude from the impedance present. This means the same stabilizing mechanism not captured by the Vlasov simulations is present in the impedance simulations as well. Further work could study this phenomenon with the stability diagram method to investigate how Landau damping comes into play in the macroparticle simulations. This exploration aims to enhance our understanding of how modes with different frequencies are stabilized differently. Additionally, it may offer insights into the observation that, when many weak Vlasov modes are present, they are not always visible in the macroparticle simulations.

This theoretical and simulation work was complemented by experimental studies at the LHC. Transverse instabilities driven by e-cloud with high e-cloud densities present. Trains of 24 bunches were injected at several values of positive chromaticities. All injections showed signs of instabilities which was consistent with the expectation of high e-cloud present in the machine. The later bunches in the trains were more unstable compared to the earlier bunches in the train and the observed instabilities were in the vertical plane. The instability growth rates, calculated with an averaged rolling window FFT algorithm, showed a clear decrease with increasing chromaticity in both beam 1 and beam 2. E-cloud in quadrupoles drive instabilities in both vertical and horizontal planes whereas e-cloud formed in dipoles drive instabilities mainly in the vertical plane. This suggests that e-cloud in dipoles significantly contributes to the measured instabilities in these conditions. The measured stabilizing effect from chromaticity could be replicated by macroparticle simulations.

Apart from using a positive chromaticity, octupoles are used to mitigate e-cloud driven instabilities. Understanding stability at 450 GeV is critical for the HL-LHC, as stronger chromaticity and octupole settings can lead to a degraded beam lifetime. The octupole current thresholds, i.e. the lowest current at which the beam is stable, were measured after scrubbing, for bunch intensity $1.1e11$, $1.4e11$, and $1.8e11$ protons/bunch. The resulting thresholds depended as expected on the bunch intensity, showing a lower threshold for higher bunch intensity. The instabilities developed at low bunch intensity were in the vertical plane whereas transverse instabilities developed simultaneously in both the horizontal and vertical planes at high bunch intensity.

Build-up simulations in conditions with a SEY of 1.4, which is the estimated SEY at the nominal operation of the LHC, predict that the central density of the e-cloud formed in dipoles is significant only for lower bunch intensity. This is consistent with the vertical transverse instabilities being observed only at the lowest bunch intensity for which measurements were conducted. The central electron density in LHC quadrupoles also depends on intensity. In particular, the density at the beam location decreases with increasing bunch intensity, which is consistent with the observed behavior of the instability threshold.

A Numerical Checks

A.1 Number of longitudinal slices

The number of points used within a bunch to model the responses was varied to check convergence and other resulting responses are plotted in Fig. A.1.

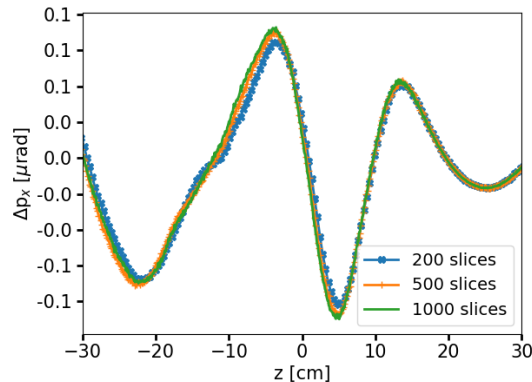


Figure A.1: The response to a sinusoid bunch distortion using 200, 500, and 1000 slices along the bunch.

The same check was done in the detuning along the bunch and the result can be seen in Fig. A.2. The three curves are again on top of each other, and 200 slices are considered to be enough.

The instability growth rates from Vlasov simulations, Fig. A.3a, and macroparticle simulations, Fig. A.3b, for simulations using 200, 500, and 1000 slices along the bunch are plotted in blue for simulations with chromaticity 0 and orange for simulations using chromaticity 15. The growth rates vary little with the number of slices.

Appendix A. Numerical Checks

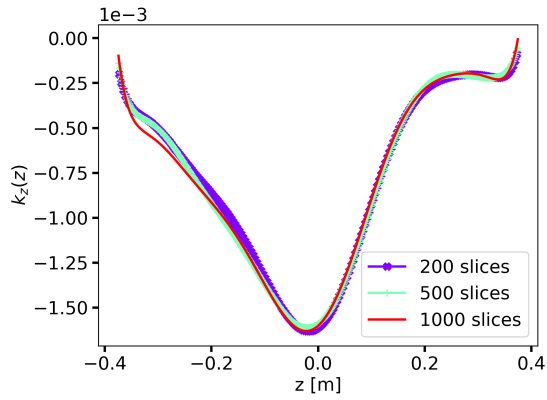
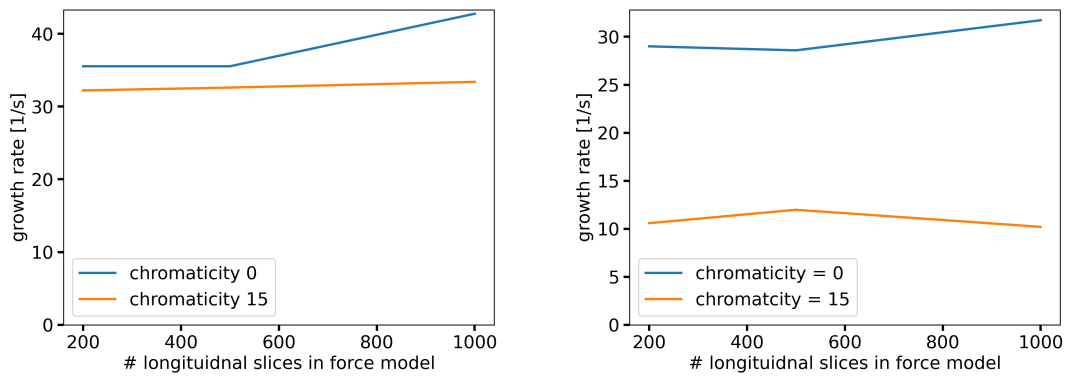


Figure A.2: The detuning along the bunch from the e-cloud in an LHC quadrupole using 200, 500, and 1000 slices along the bunch.



(a) Growth rate from Vlasov simulations.

(b) Growth rate from macroparticle simulations.

Figure A.3: The growth rates from simulations as a function of the number of longitudinal slices used. Results from simulations using chromaticity 0 are plotted in blue and from simulations with chromaticity 15 are plotted in orange.

A.2 Detuning from e-cloud in dipoles

The calculating detuning from the e-cloud in an LHC dipole is sensitive to the number of macroparticles used to simulate the interaction of the beam and e-cloud using the PIC algorithm. Either simulations with 100 times as many macroparticles are to be used, plotted as dashed red lines in Fig. A.4. The same result can be achieved by averaging 50 detuning calculated with simulation using the nominal simulations setting, see Tab. 3.3.

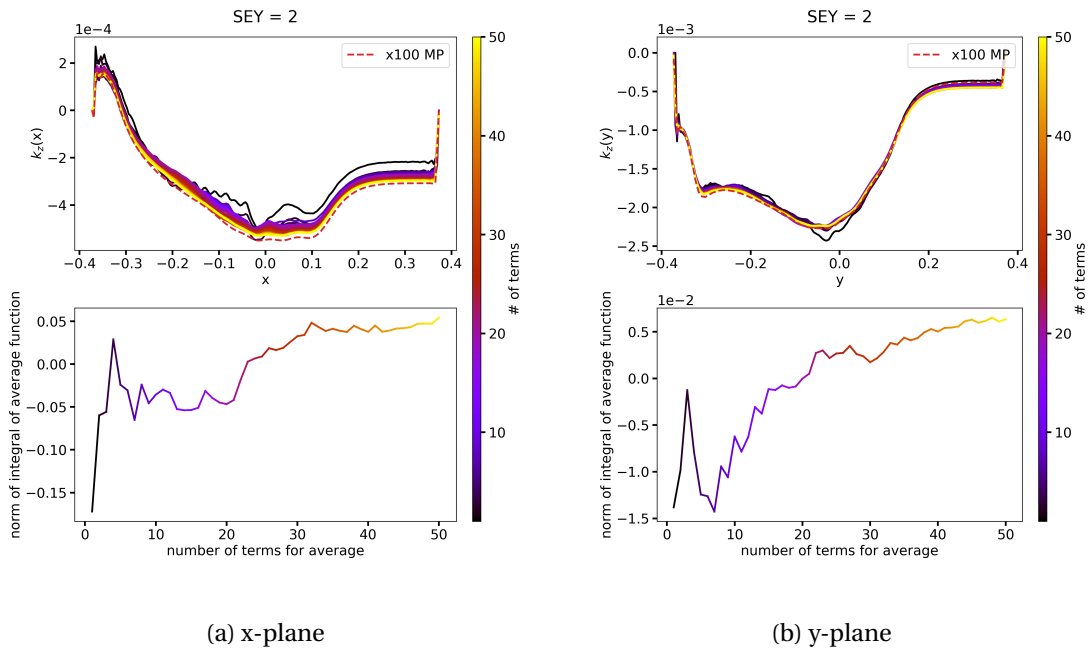


Figure A.4: The detuning along the bunch from averaging several simulations, the color of the plot corresponds to the number of simulations used in the average. The integral of the detuning as a function of the number of terms used for the average is plotted in the bottom plots. The simulations were done with thee-cloud in LHC dipoles at injection.

A similar study was conducted for the detuning from the e-cloud in quadrupole, however, the detuning was not as sensitive, as less variation with the number of terms used in the average can be seen in Fig. A.4

Appendix A. Numerical Checks

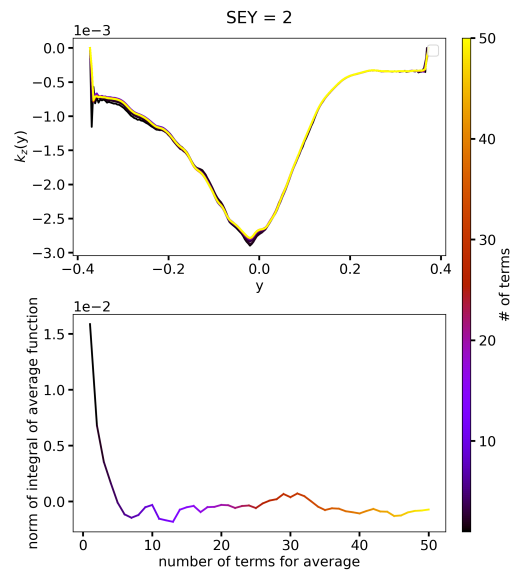


Figure A.5: The detuning along the bunch from averaging several simulations, the color of the plot corresponds to the number of simulations used in the average. The integral of the detuning as a function of the number of terms used for the average is plotted in the bottom plots. The simulations were done with thee-cloud in LHC quadrupoles at injection.

A.3 Number of macroparticles in instability simulations

The number of macroparticles was varied in the impedance simulations defined in section 2.4.1, and the resulting growth rates can be seen in Fig. A.6 for simulations with chromaticity 0, 3, and 5. The instability growth rates of the corresponding Vlasov modes are plotted in the same plotted in grey. The growth rates from simulations using 10^5 , 10^6 , and 10^7 macroparticles all give the same instability growth rates.

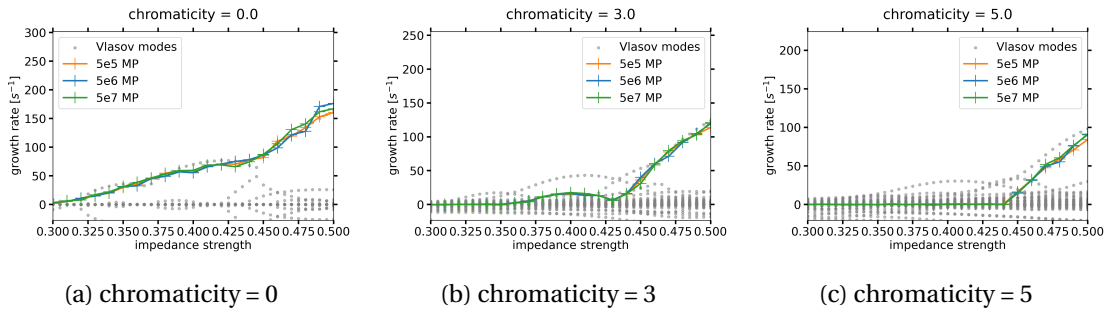


Figure A.6: The instability growth rate of macroparticle simulations using 10^5 , 10^6 and 10^7 macroparticles are plotted in orange, blue, and green respectively. The corresponding growth rates from Vlasov simulations are plotted in grey.

A.4 Number of terms Vlasov sum

There are three sums in the Vlasov equation, the m , l and p sum in:

$$\begin{aligned}
 b_{lm}(\Omega - Q_{u0}\omega_0 - l\omega_s) - \frac{\omega_0}{F_{lm}} \sum_{m'=0}^{+\infty} b_{lm'} \int dr w_l(r) \Delta Q_R(r) f_{lm}(r) f_{lm'}(r) = \\
 - \frac{N_b \beta c}{8\pi^2 Q_{u0} F_{lm}} \sum_{l'm'} b_{l'm'} \sum_{n=0}^N \iint dr d\phi e^{jl\phi} e^{j\Delta\Phi(r,\phi)} w_l(r) f_{lm}(r) \frac{g_0(r)}{W_l(r)} k_n(r \cos\phi) \\
 \times \iint \tilde{r} d\tilde{r} d\tilde{\phi} e^{-jl'\tilde{\phi}} e^{-j\Delta\Phi(\tilde{r},\tilde{\phi})} f_{l'm'}(\tilde{r}) \frac{W_{l'}(\tilde{r}) h_n(\tilde{r} \cos\tilde{\phi})}{\lambda_0(\tilde{r} \cos\tilde{\phi}) H_n^2}. \quad (A.1)
 \end{aligned}$$

The p sum is the sum over all dipolar responses. The numbers l and m correspond to the radial and azimuthal mode numbers. The number of terms used in these calculations can be varied and the resulting growth rates for the worst Vlasov mode of simulations using chromaticity 15 and the parameters defined in Tab. 2.1, can be seen for three different numbers of azimuthal modes, N_m as a function of the maximum radial mode l_{max} used.

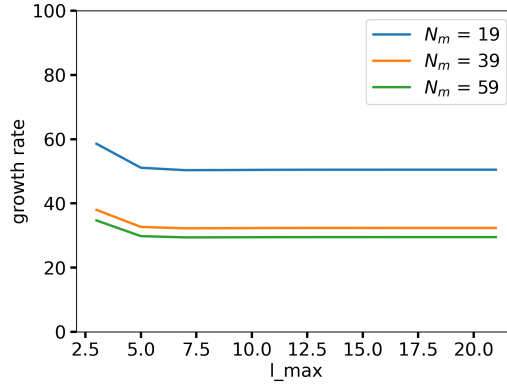


Figure A.7: The instability growth rate of Vlasov simulations using a different number of azimuthal modes, N_m and radial modes l_{max}

Bibliography

- [1] M. Streit-Bian. *CERN Science Bridging cultures*. Open Access, CC BY licens, 2018.
- [2] CERN. CERN Annual report 2022. Technical report, CERN, Geneva, 2023.
- [3] H. Schopper and L. De Lella. *60 Years of CERN Experiments and Discoveries*. World Scientific, Singapore, 2015.
- [4] E. Lopienska. The CERN accelerator complex, layout in 2022. Complexe des accélérateurs du CERN en janvier 2022, 2022. General Photo.
- [5] O. Brüning, P. Collier, P Lebrun, S. Myers, R. Ostojic, J. Poole, and P. Proudlock. *LHC Design Report*. CERN Yellow Reports: Monographs. CERN, Geneva, 2004.
- [6] Cern accelerating science. <https://home.cern/science/accelerators/accelerator-complex>. retrieved 01-11-2023.
- [7] M. Krause. *CERN - How We Found the Higgs Boson*. WORLD SCIENTIFIC, 2014.
- [8] M. Poehler. *CERN Masterplan 2040: General strategy*. CERN, Geneva, 2021. Taken from the French edition: Maître d’ouvrage: CERN - mandataires: Urbaplan.
- [9] M Lamont. Wrap-up and prospects for post LS1 operations. In *4th Evian Workshop on LHC beam operation*, 2012.
- [10] G. Iadarola, G. Rumolo, P. Dijkstal, and L. Mether. Analysis of the beam induced heat loads on the LHC arc beam screens during Run 2. Technical Report CERN-ACC-NOTE-2017-0066, Dec. Dec. 2017.
- [11] V. Kain, S. Albright, R. Alemany-Fernández, M. Angoletta, F. Antoniou, T. Argyropoulos, and F. et. al. Asvesta. Achievements and Performance Prospects of the Upgraded LHC Injectors. *JACoW IPAC*, 2022:1610–1615, 2022.
- [12] M. Lamont. Welcome and introduction. In *Chamonix '22*, 2022.
- [13] O. Aberle, I Béjar Alonso, O Brüning, P Fessia, L Rossi, L Tavian, M Zerlauth, C. Adorisio, A. Adraktas, and M. et. al. Ady. *High-Luminosity Large Hadron Collider (HL-LHC): Technical design report*. CERN Yellow Reports: Monographs. CERN, Geneva, 2020.

Bibliography

- [14] E. Metral, G. Rumolo, and W. Herr. *Impedance and Collective Effects*, pages 105–181. Springer International Publishing, Cham, 2020.
- [15] F Zimmermann. Electron cloud effects in accelerators. In *E-CLOUD'18: Proceedings of the Joint INFN-CERN-ARIES Workshop on Electron-Cloud Effects*, 2020.
- [16] G Rumolo, H Bartosik, E Belli, G Iadarola, K Li, L Mether, A Romano, F Zimmermann, P Dijkstal, and M Schenk. Electron cloud effects at the CERN accelerators. In *E-CLOUD'18: Proceedings of the Joint INFN-CERN-ARIES Workshop on Electron-Cloud Effects*, 2020.
- [17] G. Iadarola and G. Rumolo. Electron Cloud Effects. *ICFA Beam Dyn. Newsl.*, 69:208–226, 2016.
- [18] E. Prat. Synchrotron light sources and x-ray free-electron-lasers, 2021.
- [19] G. Arduini. Electron cloud and ion effects. In *8th European Particle Accelerator Conference*, 2002.
- [20] H Seiler. Secondary electron emission in the scanning electron microscope. *Journal of Applied Physics*, 54(11):R1–R18, 11 1983.
- [21] M.A. Furman. Electron Cloud Effects in Accelerators. In *Joint INFN-CERN-EuCARD-AccNet Workshop on Electron-Cloud Effects: E-CLOUD'12*, 2013.
- [22] G. Skripka, G. Iadarola, L. Mether, and G. Rumolo. Non-monotonic dependence of heat loads induced by electron cloud on bunch population at the LHC. *Eur. Phys. J. Plus*, 137(7):849, 2022.
- [23] V Petit, H Neupert, E Garcia-Tabares, M Taborelli, and M Belhaj. Surface characterization of vacuum components extracted from LHC dipole magnet. In *E-CLOUD'18: Proceedings of the Joint INFN-CERN-ARIES Workshop on Electron-Cloud Effects*, 2020.
- [24] C. Yin Vallgren, G. Arduini, J. Bauche, S. Calatroni, P. Chiggiato, K. Cornelis, P. Costa Pinto, B. Henrist, E. Métral, H. Neupert, G. Rumolo, E. Shaposhnikova, and M. Taborelli. Amorphous carbon coatings for the mitigation of electron cloud in the cern super proton synchrotron. *Phys. Rev. ST Accel. Beams*, 14:071001, Jul 2011.
- [25] A Novelli, M Angelucci, A Liedl, L Spallino, R Cimino, and R Larciprete. Surface effects for electron cloud. In *ICFA mini-Workshop on Mitigation of Coherent Beam Instabilities in Particle Accelerators (MCBI 2019)*, 2020.
- [26] G Iadarola and G Rumolo. Electron Cloud Effects. *CERN Yellow Rep. Conf. Proc.*, 1:49–56, 2018.
- [27] R. Cimino, M. Commisso, D. R. Grosso, T. Demma, V. Baglin, R. Flammini, and R. Larciprete. Nature of the decrease of the secondary-electron yield by electron bombardment and its energy dependence. *Phys. Rev. Lett.*, 109:064801, 2012.

-
- [28] F Ruggiero, G. Rumolo, and F. Zimmermann. Simulation of the electron-cloud build up and its consequences on heat load, beam stability and diagnostics. *Phys. Rev. Spec. Top. Accel. Beams*, 4:012801, 2001.
- [29] J M Jimenez, Gianluigi Arduini, Paul Collier, G Ferioli, Bernard Henrist, Noël Hilleret, L Jensen, Jean Michel Laurent, K Weiss, and F Zimmermann. Electron Cloud Studies and Beam Scrubbing Effect in the SPS. Technical report, CERN, Geneva, 2003.
- [30] G. Iadarola, B. Bradu, P. Dijkstal, L. Mether, and G. Rumolo. Impact and Mitigation of Electron Cloud Effects in the Operation of the Large Hadron Collider. In *8th International Particle Accelerator Conference*, 2017. TUPVA019.
- [31] F Zimmermann. Electron cloud effects in the LHC. In *Proceedings E-CLOUD'02 : Mini Workshop on Electron Cloud Simulations for Proton and Positron Beams*, 2002.
- [32] N Karastathis, M Barnes, H Bartosik, K Brodzinski, X Buffat, F Cerutti, S Fartoukh, B Goddard, G Iadarola, S Le Naour, A Lechner, J Maestre Heredia, A Mereghetti, E Métral, D Missiaen, N Mounet, F X Nuiry, S Papadopoulou, Y Papaphilippou, B Petersen, G Rumolo, B Salvant, C Schwick, M Solfaroli Camillocci, G Sterbini, H Timko, R Tomas Garcia, J Uythoven, and J Wenninger. LHC Run 3 Configuration Working Group Report. In *9th LHC Operations Evian Workshop*, 2019.
- [33] K. Ohmi. Electron cloud effects in positron storage rings. In *ICFA mini-Workshop on Mitigation of Coherent Beam Instabilities in Particle Accelerators*, 2020.
- [34] F Zimmermann. Review of single bunch instabilities driven by an electron cloud. *Phys. Rev. Spec. Top. Accel. Beams*, 7:124801, 2005.
- [35] W. Hölfe. Status and prospects in fast beam-based feedbacks. In *JACoW IPAC*, volume 2022, pages 3112–3317, 2022.
- [36] A. Romano, G. Iadarola, K. Li, and G. Rumolo. Macroparticle Simulation Studies of the LHC Beam Dynamics in the Presence of Electron Cloud. In *8th International Particle Accelerator Conference*, 2017. TUPVA018.
- [37] E. Métral. Effect of bunch length, chromaticity, and linear coupling on the transverse mode-coupling instability due to the electron cloud. In *Proceedings E-CLOUD'02 : Mini Workshop on Electron Cloud Simulations for Proton and Positron Beams*, 2002.
- [38] H. Wiedemann. *Particle Accelerator Physics I*. Springer, New York, 1999.
- [39] K. Wille. *The Physics of Particle Accelerators*. Oxford University Press, 2000.
- [40] F Tecker. Longitudinal beam dynamics, 2014. 21 pages, contribution to the CAS - CERN Accelerator School: Advanced Accelerator Physics Course, Trondheim, Norway, 18-29 Aug 2013.

Bibliography

- [41] A. Wolski. *Beam Dynamics in high energy particle accelerators*. Imperial College Press, 2014.
- [42] S. Johannesson. Fast retuning of superconducting radiofrequency accelerating cavities in the european spallation source linear accelerator., June 2020. Master thesis, Lund University, Available at <https://www.eit.lth.se/index.php?gpuid=288&L=1&eauid=1288>.
- [43] G. Vilasi. *Hamiltonian Dynamics*. World Scientific Publishing Co. Pte. Ltd., Singapore, 2001.
- [44] H. Wiedemann. *Particle Accelerator Physics II*. Springer, Berlin, 1999.
- [45] J. V. José and E. J. Saletan. *Classical Dynamics, A contemporary approach*. Cambridge University Press, United States of America, 1998.
- [46] C. Holmes. Canonical transformations. <https://courses.smp.uq.edu.au/MATH4104/m4104sec3.pdf>, 2009. Lecture notes for course MATH4104 from University of Queensland Australia, Accessed: 2023-10-13.
- [47] K. Habermann and L. Habermann. *Introduction to Symplectic Dirac operators*. Springer, Netherlands, 2006.
- [48] A. J. Dragt. *Lie Methods for Nonlinear Dynamics with Applications to Accelerator Physics*. Dynamical Systems and Accelerator Theory Group, Department of Physics, University of Maryland, College Park, Maryland 20742, 2020.
- [49] A. W. Chao. *Physics of Collective Beam Instabilities in High Energy Accelerators*. John Wiley and sons, Inc, 1993.
- [50] K. Li. Perturbation formalism. https://kli.web.cern.ch/USPAS_Lectures_Collective_Effects/Lectures/USPAS_05a_Vlasov_equation.pdf, 2015. Lecture at the US Particle Accelerator School, Hampton, Virginia, USA, 19-23 January.
- [51] N. Mounet. Direct Vlasov solvers, 2020. Proceedings of the 2018 CERN–Accelerator–School course on Numerical Methods for Analysis, Design and Modelling of Particle Accelerators, Thessaloniki, (Greece).
- [52] V. Kain. Emittance Preservation. *CERN Yellow Rep. School Proc.*, 5:345, 2018.
- [53] S. Fartoukh, S. Kostoglou, M. Solfaroli Camillocci, G. Arduini, H. Bartosik, C. Bracco, K. Brodzinski, R. Bruce, X. Buffat, M. Calviani, F. Cerutti, I. Efthymiopoulos, B. Goddard, G. Iadarola, N. Karastathis, A. Lechner, E. Metral, N. Mounet, F. Nuiry, P. Papadopoulou, Y. Papaphilippou, B. Petersen, T. Persson, S. Redaelli, G. Rumolo, B. Salvant, G. Sterbini, H. Timko, R. Tomas Garcia, and J. Wenninger. LHC Configuration and Operational Scenario for Run 3. Technical report, CERN, Geneva, 2021.
- [54] J. Wenninger. Operation and Configuration of the LHC in Run 2. 2019. CERN-ACC-NOTE-2019-0007.

- [55] N. Mounet. Vlasov Solvers and Macroparticle Simulations. In V. Brancolini, G. Rumolo, M.R. Masullo, and S. Petracca, editors, *ICFA Mini-Workshop on Impedances and Beam Instabilities in Particle Accelerators, 18 - 22 Sep 2017, Benevento, Italy: Proceedings*, pages 77–85, 2018. CERN-2018-003-CP.
- [56] K Ohmi, E A Perevedentsev, and F Zimmermann. Wake-field and fast head-tail instability caused by an electron cloud. *Phys. Rev. E*, 65:016502, 2002.
- [57] E. Perevedentsev. Head-tail instability caused by electron cloud. In *E-CLOUD'02: Mini-workshop on electron-cloud simulations for proton and positron beams, CERN, Geneva, Switzerland, 15-18 Apr 2002: Proceedings*, pages 171–194, 4 2002. CERN-2002-001.
- [58] G. Iadarola, L. Mether, N. Mounet, and L. Sabato. Linearized method for the study of transverse instabilities driven by electron clouds. *Phys. Rev. Accel. Beams*, 23(8):081002, 2020.
- [59] G. Iadarola, L. Mether, N. Mounet, and L. Sabato. A Vlasov approach to study transverse instabilities driven by electron clouds . 2020. CERN-ACC-NOTE-2020-0054.
- [60] W. Hillert. Transverse linear beam dynamics, 2021.
- [61] M. Abramowitz, I. A. Stegun, and R. H. Romer. Handbook of Mathematical Functions with Formulas, Graphs, and Mathematical Tables. *American Journal of Physics*, 56(10):958–958, 10 1988.
- [62] C. R. Harris, K. Jarrod Millman, S. J. van der Walt, R. Gommers, P. Virtanen, D. Cournapeau, E. Wieser, J. Taylor, S. Berg, N. J. Smith, R. Kern, M. Picus, S. Hoyer, M. H. van Kerkwijk, M. Brett, A. Haldane, J. F. del Río, M. Wiebe, P. Peterson, P. Gérard-Marchant, K. Sheppard, T. Reddy, W. Weckesser, H. Abbasi, C. Gohlke, and T. E. Oliphant. Array programming with NumPy. *Nature*, 585(7825):357–362, September 2020.
- [63] G. Iadarola and G. Rumolo. PyE-CLOUD and build-up simulations at CERN. *Conf. Proc. C*, 1206051:189–194, 2013. Comments: 6 pages, contribution to the Joint INFN-CERN-EuCARD-AccNet Workshop on Electron-Cloud Effects: E-CLOUD'12; 5-9 Jun 2012, La Biodola, Isola d'Elba, Italy.
- [64] G. Iadarola. Electron cloud studies for CERN particle accelerators and simulation code development, 2014. PhD Thesis, U. Naples (main), Presented 23 05 2014.
- [65] G. Iadarola, E. Belli, K. Li, L. Mether, A. Romano, and G. Rumolo. Evolution of Python Tools for the Simulation of Electron Cloud Effects. In *8th International Particle Accelerator Conference*, 2017. THPAB043.
- [66] F. Zimmermann. Electron cloud simulations for SPS and LHC. In *10th Workshop on LEP-SPS Performance*, 2000.
- [67] G. Iadarola and G. Rumolo. Electron cloud effects. *CERN Yellow Rep. Conf. Proc.*, 1:49–56, 2018.

Bibliography

- [68] R J Macek, A A Browman, J E Ledford, M J Borden, J F O'Hara, R C McCrady, L J Rybarcyk, T Spickermann, T J Zaugg, and M T F Pivi. Electron cloud generation and trapping in a quadrupole magnet at the Los Alamos PSR. Technical report, SLAC, Stanford, CA, 2007.
- [69] A. Romano. Electron cloud formation in CERN particle accelerators and its impact on the beam dynamics, 2018. PhD Thesis, TU Darmstadt, Presented 2018.
- [70] A. Oeftiger. An Overview of PyHEADTAIL. 2019. CERN-ACC-NOTE-2019-0013.
- [71] K. Li, H. Bartosik, S. Hegglin, G. Iadarola, A. Oeftiger, A. Passarelli, A. Romano, G. Rumolo, and M. Schenk. Code development for collective effects. In *57th ICFA Advanced Beam Dynamics Workshop on High-Intensity and High-Brightness Hadron Beams*, 2016. WEAM3X01.
- [72] R Bartolini and F Schmidt. A Computer Code for Frequency Analysis of Non-Linear Betatron Motion. Technical report, CERN, Geneva, 1998.
- [73] K. Li. Collective effects – an introduction. Proceedings of the CERN–Accelerator–School course: Introduction to Particle Accelerators pp. 437–489, 2021.
- [74] N. Mounet and E. Métral. Electromagnetic fields and beam coupling impedances in a multilayer flat chamber. 2010. CERN-ATS-Note-2010-056 TECH.
- [75] L. Mether, B. Bradu, G. Iadarola, S. Johannesson, K. Paraschou, G. Rumolo, and L. Sabato. Electron cloud observations and mitigation for the lhc run 3. In *14th Int. Particle Accelerator Conf. (IPAC'23)*, volume 2023, page WEPA091, 2023. Conference paper.
- [76] L. Carver, X. Buffat, A. Butterworth, W. Höfle, G. Iadarola, G. Kotzian, K. Li, E. Métral, M. Ojeda Sardonís, M. Söderén, and D. Valuch. Usage of the Transverse Damper Observation Box for High Sampling Rate Transverse Position Data in the LHC. In *8th International Particle Accelerator Conference*, 2017. MOPAB113.
- [77] M. Söderén and D. Valuch. Low Latency, Online Processing of the High-Bandwidth Bunch-By-Bunch Observation Data From the Transverse Feedback System in the LHC. *EPJ Web Conf.*, 245:01036, 2020.
- [78] S. Kostoglou, N. Karastathis, Y. Papaphilippou, D. Pellegrini, and P. Zisopoulos. Development of Computational Tools for Noise Studies in the LHC. In *8th International Particle Accelerator Conference*, 2017. THPAB044.
- [79] V. Sedlakova, L. Mether, and Konstantinos P. Reconstruction of the SEY evolution during the 2022 LHC scrubbing run. SEY - Secondary Emission Yield. 2022. CERN-STUDENTS-Note-2022-112.
- [80] K Li and G Rumolo. Mitigation of Electron Cloud Instabilities in the LHC using Sextupoles and Octupoles. *Conf. Proc.*, C1205201:WEPPR068, 2012.

- [81] H. Bartosik, Y. Papaphilippou, and A. Wolski. A first taste of nonlinear beam dynamics, 2022.
- [82] N. Mounet. The LHC Transverse Coupled-Bunch Instability, 2012. PhD Thesis, Ecole Polytechnique, Lausanne, Presented 2012.
- [83] L. Sabato, G. Iadarola, and L. Mether. Numerical simulations studies on single-bunch instabilities driven by electron clouds at the LHC . 2020. CERN-ACC-NOTE-2020-0050.
- [84] A. Romano, O. Boine-Frankenheim, X. Buffat, G. Iadarola, and G. Rumolo. Electron cloud buildup driving spontaneous vertical instabilities of stored beams in the Large Hadron Collider. *Phys. Rev. Accel. Beams*, 21(6):061002, 2018.

Abbreviations

FFT = Fast Fourier Transform

LHC = Large Hadron Collider

MP = Macroparticle Tracking Simulations

RF = Radio Frequency

rev = Revolution in the Machine

SEY = Secondary Electron Yield

SPS = Super Proton Synchrotron

s = Seconds

PIC = Particle-In-Cell

SOFIA JOHANNESSON

PhD Student in Accelerator Physics

@ sofia.carolina.johannesson@cern.ch 📍 Geneva, Switzerland
in <https://www.linkedin.com/in/sofia-johannesson-516219116>



WORK EXPERIENCE

PhD Student

I am enrolled at EPFL and my PhD work is done at CERN in the beams department. I am part of the electron cloud team and study instabilities driven by electron cloud in the Large Hadron Collider and the Super Proton Synchrotron through simulations and beam-based measurements. I am developing a new simulation tool based on the linearized Vlasov equation to reach time scales not accessible by conventional simulation methods. I have also been involved in the commissioning of Large Hadron Collider and the Super Proton Synchrotron to mitigate electron cloud effects.

CERN

📅 2020 - Present 📍 Meyrin, Switzerland

Master thesis worker

I was working with the beam physics group at ESS. ESS has high beam availability requirements which means that small errors should be able to occur without the entire machine needing to shut down. To deal with one or multiple of the accelerating cavities being offline, I wrote a program that fast-tunes the other cavities to compensate so that the beam stability is preserved. The best cavities settings could be obtained by simulating the whole accelerator.

European Spallation Source (ESS)

📅 Nov 2019-May 2020 📍 Lund, Sweden

Summer worker

I worked, for the summer, in the technology department of Axis. For the first summer, my mission was to investigate and explain a phenomenon which is in the borderline of optics and sensor technology. The second summer I investigated how multi-spectral images can be created and used in sensor simulations.

Axis Communications

📅 2018 & 2019 📍 Lund, Sweden

RESEARCH INTERESTS

- Particle accelerator physics (beam-based measurements and collective effects)
- The Muon Collider Collaboration
- Plasma Acceleration
- Medical applications of accelerator technology
- Accelerator Driven Systems

EDUCATION

PhD in Accelerator Physics

EPFL, Laboratory of Particle Accelerator Physics

📅 2020-Present 📍 Lausanne, Switzerland

Degree of Master of Science in Engineering, Engineering Physics

Lund University

📅 2015 - 2020 📍 Lund, Sweden

Exchange year (1st year of master)

UC Santa Cruz

📅 2018-2019 📍 Santa Cruz, USA

High School, Special program: physics peak

Polhemskolan

📅 2012-2015 📍 Lund, Sweden

TEACHING/OUTREACH

Teaching Assistant, EPFL, 2021

I was a teaching assistant for the EPFL master course "Introduction to particle accelerators" taught by Prof. Mike Seidel. The work consisted of hosting 2h tutorial session each week and correct weekly assignments. It was truly rewarding to see the students become interested in accelerators and expanding their knowledge by answering their questions. My own knowledge of accelerator physics was advanced thanks to the student many inquiries.

SKILLS

PYTHON, PyHEADTAIL, PyECLOUD, Vlasov Solvers

UNIX, CLUSTER COMPUTING, MATLAB
SWEDISH (NATIVE), ENGLISH (C2), BASIC FRENCH

EXTRACURRICULAR

Aerial dance, hiking, Via Ferrata, Adv. Scuba diving certificate, former swimming instructor.

PROCEEDINGS AND TALKS

- S. Johannesson, et. al. "A linearized Vlasov method for the study of transverse e-cloud instabilities" (Poster and Proceedings), in Proc. HB2023, Geneva, Switzerland, Oct. 2023
- S. Johannesson, et. al. "Investigating LHC Electron Cloud Instabilities through Linearized Vlasov Method", in the Joint Annual Meeting of the Swiss and Austrian Physical Society, Basel, Switzerland, Sept. 2023, oral contribution
- S. Johannesson, et. al. "Study of LHC e-cloud instabilities using the linearised Vlasov method" (Poster and Proceedings), in Proc. IPAC'23, Venice, Italy, May. 2023, paper WEPA090, this conference.
- S. Johannesson, "A novel Vlasov approach for modelling electron cloud instabilities", in the 8th e-cloud workshop, La biodola, Isola d'Elba Italy, Sept. 2022. oral contribution
- S. Johannesson, "Vlasov solver for e-cloud and combined effects", in FCC Innovation Study Workshop, Meyrin Switzerland, Dec. 2022. oral contribution
- S. Johannesson, "Fast retuning of superconducting radiofrequency accelerating cavities in the European Spallation Source linear accelerator", Master Thesis, Lund, Sweden, Jun 2020

Planned

- S. Johannesson, et. al. "A Novel Vlasov Approach for Modeling Electron Cloud Instabilities" (invited talk), IPAC'24, Nashville, USA, May 2024.

SCHOOLS

CERN Accelerator School (CAS) – Advanced Accelerator physics

CERN

 2022

 Sévrier, France

CERN Accelerator School (CAS) - Introduction to Accelerator physics

CERN

 2021

 Chavannes de Bogis , Switzerland

Joint Universities Accelerator School (JUAS) – Accelerator physics and technology.

European Scientific Institute

 2020

 Archamps, France
